UNIVERSITÀ DEGLI STUDI DI UDINE
hic sunt futura

www.uniud.it

Corso di dottorato di ricerca in:

SCIENZE DELL'INGEGNERIA ENERGETICA E AMBIENTALE

Ciclo XXXI

DIPARTIMENTO POLITECNICO DI INGEGNERIA E ARCHITETTURA

Titolo della tesi

A RANS-informed model for the fast prediction of noise from Contra-Rotating Open Rotors including the effect of the blade tip vortex

Dottorando

Damiano Tormen

Supervisore

Prof. Pietro Giannattasio

Anno 2019

To my parents

ABSTRACT

The continuous increase in air traffic is leading to a growing interest in the development of new engine concepts for fuel saving and noise reduction. The Contra-Rotating Open Rotor (CROR) engine architecture has shown the potential for a significant fuel burn reduction. Unfortunately, CRORs exhibit very high noise emissions that have a significant environmental impact, especially during aircraft take-off and landing. Therefore, the noise reduction must be considered in the earliest stages of a multidisciplinary design strategy.

The interaction noise (IN) emitted by CRORs, which is generated by the aerodynamic interaction between the counter-rotating blade rows, is particularly intense at take-off. To compute accurately this interaction noise, Unsteady Reynolds Averaged Navier-Stokes (URANS) simulations coupled with the Ffowcs Williams-Hawkings (FWH) acoustic analogy would be necessary. However, the very large computational burden of such a numerical approach is not compatible with a multidisciplinary design procedure.

Jaron et al. (2014) proposed a model for the fast prediction of the noise emitted by CRORs, based on data extracted from steady-RANS simulations coupled with the mixing plane concept. However, this RANS-informed model is based on the 2D flow assumption, and hence it is not able to consider properly the impact of three-dimensional flow structures on the interaction noise. Among the different sources of aerodynamic interaction, the strongly 3D tip vortices released by the front blades and impacting the rear blades are major drivers of IN. Therefore, their influence must be properly taken into account for an accurate noise prediction.

The present thesis focuses on the development of an improved RANS-informed model for the fast prediction of the IN emitted by CRORs including the effect of the tip vortices. A genuinely 3D semi-analytical model of the tip vortex (TV) has been developed. The model is calibrated using data extracted from steady-RANS solutions and is employed to reconstruct the velocity perturbations due to the front rotor tip vortices at the inlet of the rear rotor. A specially developed procedure, based on the RANS vorticity fitting, is adopted for the calibration of the TV model.

The TV model has been coupled with the model of Jaron et al., which accounts for the 2D flow perturbations due to the viscous wake and potential field generated by the front rotor, in order to provide a more general and accurate RANS-informed procedure for the reconstruction of the flow unsteadiness at the CROR rear rotor.

The reconstructed velocity perturbations are used to compute the unsteady aerodynamic loads on the rear blades by means of an analytical blade response model (Goldstein, 1976). Then, the

IN is computed through an analytical noise propagation model in the frequency domain (Hanson, 1985).

The flow simulations and the IN computations performed in the present thesis refer to CROR UDF F7/A7, a 8 x 8 blade count configuration for which sufficient geometrical and experimental data are available in the literature.

Comparisons with data extracted from a URANS simulation show that the TV model improves significantly the reconstruction of the velocity perturbations at the rear rotor leading edge.

The noise emissions computed from the flow perturbations reconstructed by the RANS-informed model are compared with those resulting from the URANS perturbations, using the analytical acoustic model in both cases. It is found that these results agree much better when the contribution of the tip vortices is taken into account.

A comparison with the results of the FWH acoustic analogy shows some inaccuracies of the proposed approach. These are mainly ascribed to inherent limitations of the blade response model adopted in the present work. However, the general trend of the noise levels along a sideline parallel to the CROR axis is predicted reasonably well.

The proposed RANS-informed model shows the potential to be successfully embedded in a multidisciplinary optimization strategy of CROR engines.

ACKNOWLEDGEMENTS

First and foremost, I would like to express my gratitude to my supervisor Prof. Pietro Giannattasio. His precious and constant support was fundamental for the completion of this Ph.D. thesis. He taught me to be humble and that the learning never stops. I like to consider him as a friend rather than a supervisor.

A special acknowledgement goes to the Austrian Institute of Technology, which largely supported my research. In particular, I am very grateful to Alessandro Zanon for his invaluable technical support and his encouragements. I also thank Helmut Kühnelt and Michele De Gennaro for their interest in my work and their precious suggestions.

I warmly thank my Ph.D. colleagues at the University of Udine, Marco, Maurizio, Diego, and all the others, who shared with me the joys and the difficulties of the Ph.D. course.

I cannot forget my dear friends, Alessio, Alberto, Lorenzo, Davide, and many others, who have always been on my side and made me feel happy.

A great thank you goes to Lisa, whose presence and love gave me the serenity and the strength to carry out this work.

Finally, I wish to thank my parents and my sister. Their constant support and advice have been indispensable for my studies and my life. I'm very grateful to my mother, whose strength and energy inspired me. I will always be in debt with my father, who pushed me to go further and further. He passed away one year ago, but I feel as if he is always on my side. I like to believe that he would be proud of me.

TABLE OF CONTENTS

NOMENCLATURE

B	Blade number
BPF	Blade passing frequency
C_D	Drag coefficient
C_L	Lift coefficient
c	Chord length
$(\boldsymbol{e}_x, \boldsymbol{e}_r, \boldsymbol{e}_\vartheta)$	Local cylindrical reference frame of the vortex
$(\boldsymbol{e}_X, \boldsymbol{e}_R, \boldsymbol{e}_\Psi)$	Cylindrical reference frame of the front rotor
$(\boldsymbol{e}_x, \boldsymbol{e}_y, \boldsymbol{e}_z)$	Local cartesian reference frame of the vortex
$(\boldsymbol{e}_X, \boldsymbol{e}_Y, \boldsymbol{e}_Z)$	Cartesian reference frame of the front rotor
FR	Front rotor
f	Frequency
h	Harmonic order
IN	Interaction noise
k	Wavenumber
LE	Leading edge
MP	Mixing plane
r_c	Viscous core radius
RR	Rear rotor
SPL	Sound pressure level
TE	Trailing edge
TV	Tip vortex
$\boldsymbol{u}$	Model absolute velocity
$\boldsymbol{v}$	Absolute velocity
$\boldsymbol{V}$	Uniform absolute velocity
$V_{x,def}$	Peak of the vortex axial velocity deficit
$\boldsymbol{w}$	Relative velocity
$\boldsymbol{W}$	Uniform relative velocity
(x, r, ϑ)	Local cylindrical coordinate system of the vortex
(X, R, Ψ)	Cylindrical coordinate system of the front rotor
(X_a, R_a, Ψ_a)	Absolute cylindrical coordinate system
(X, Y, Z)	Coordinate system of the front rotor

(X_a, Y_a, Z_a)	Absolute cartesian coordinate system

Γ	Circulation
ρ	Density
σ	Reduced frequency
Ω	Rotational speed
$\boldsymbol{\omega}$	Absolute vorticity

SUBSCRIPTS

0	Freestream
1	Front rotor
2	Rear rotor
c	Tip vortex centre
def	Tip vortex velocity deficit
ind	Induced velocity
T	Rotor tip
uw	Ultimate wake

1 INTRODUCTION

1.1 Architecture of CROR engines

In the context of civil aviation, the concerns about fuel prices and environmental impact are pushing the development of new engine concepts for fuel saving and noise reduction. As a fuel saving solution, the Contra-Rotating Open Rotor (CROR) engine architecture, which was initially developed during 80's and early 90's [1,2], has received renewed interest for the propulsion of short-medium range aircraft [1,3,4]. CRORs consist of two rows of unshrouded blades rotating in opposite directions, powered by a core turbine. As an example, Figure 1.1 illustrates the UDF (acronym of UnDucted Fan) open rotor engine, developed by General Electric during 80's, installed on a McDonnel-Douglas MD-80 to perform flight tests [5]. The contra-rotating rear blades recover the swirl kinetic energy produced by the front blades, which would be wasted in a single blade row configuration, providing an increase in the propulsive efficiency of about 8% [6,7]. The absence of an external nacelle allows obtaining very high bypass ratios and reducing aircraft drag and weight [8]. In light of these features, CRORs exhibit a very high propulsive efficiency and they have the potential for a fuel burn reduction up to 30% compared to high bypass turbofans. Unfortunately, the absence of a shroud limits the possibility of dampening the noise emitted by the engine. This causes open rotors to exhibit a very high noise emission that has a significant environmental impact, especially at take-off and approach.

Figure 1.1 – Contra-rotating Open Rotor in pusher configuration.
General Electric UDF® (UnDucted Fan) mounted on a McDonnel-Douglas MD-80.

In recent years, many experimental campaigns have been undertaken in the USA [1,9–12] and in Europe [4,13,14] to assess the aerodynamic and acoustic features of CRORs, along with several numerical studies aimed at developing appropriate computational strategies and gaining a better understanding of the noise generation mechanisms [12,15–20]. Although the modern computational capabilities have enabled progress in CROR aeroacoustic design, further developments are needed to achieve the stringent noise targets imposed by the International Civil Aviation Organization (ICAO) [21,22].

1.2 Noise generation mechanisms in CRORs

In order to identify effective strategies for noise reduction, it is necessary to understand the mechanisms involved in the noise generation. The noise emitted by the blades is recognized as the main contribution to the overall acoustic signature of a CROR engine, and it can be classified into tonal noise and broadband noise. The former is due to periodic phenomena and emerges at discrete frequencies, while the latter is random in nature and contains components at all frequencies. A comprehensive description of the noise generation mechanisms in single-rotating and contra-rotating blades is given by Magliozzi et al. [23]. In general, the noise sources can be divided into two categories:

- Steady sources: they appear constant in time for an observer in the reference frame rotating with the blade.
- Unsteady sources: they are time dependent in the reference frame rotating with the blade.

The steady sources and the unsteady sources that are periodic in time are responsible for the emission of the tonal noise components, while the unsteady sources that exhibit a random behaviour give rise to the broadband noise.

1.2.1 Tonal noise generated by steady sources

Although the steady sources are constant in time in the reference frame relative to the blades, they produce tonal noise due to the periodical perturbation of the medium during the blade rotation. They can be divided into thickness, loading and volume (nonlinear) sources [24–26], and the related noise generation mechanisms are as follows:

- Thickness sources: generated by the periodic displacement of the air by the volume of a rotating blade. They can be represented by a distribution of acoustic monopole sources.

- Loading sources: correspond to the forces acting on the fluid due to the viscous stress and pressure distributions on the blade surface. Since the blade rotates, these forces cause periodical flow perturbations and hence tonal noise generation. Loading sources can be represented by a distribution of acoustic dipoles.
- Volume (nonlinear) sources: are due to nonlinear effects occurring in the flow field around the blades. They represent the shear stress in the fluid [26]. Since the volume sources can be described by acoustic quadrupoles distributed in the volume surrounding the blade, their contribution is usually called quadrupole noise.

In a CROR engine, the tonal noise due to the steady sources is emitted by each blade row at frequencies that are multiples of the Blade Passing Frequency ($BPF =$ No. blades $\times (rpm/60)$ [Hz]), i.e., $f_1 = h_1 \times BPF_1$ and $f_2 = h_2 \times BPF_2$, with h_1,$h_2 \in \mathbb{N}$. This kind of tonal noise is usually called rotor self-noise.

1.2.2 Tonal noise generated by unsteady sources

The loading sources that are periodic in the reference frame rotating with the blade generate tonal noise components. For example, periodic blade loads occur when the rotor axis is tilted relative to the inflow direction. In this operating condition, the blades experience a cyclic variation of flow incidence and, consequently, the loading undergoes periodic variation [17].

In a CROR, the aerodynamic interactions between front rotor (FR) and rear rotor (RR) cause significant fluctuations of the blade loading. These interactions are due to the following phenomena:

- Impingement of the front rotor wakes on the rear rotor blades.
- Mutual effects of the potential flow fields generated by the two rotors.

Each blade of the front rotor sheds a wake that is convected into the rear rotor. These wakes include velocity deficits ascribed to the viscous wakes, secondary vortices developing in the hub region, and tip vortices (TVs). Since these flow structures are periodic in the circumferential direction of the front rotor, they generate periodic load fluctuations on the rear blades.

Also the bound potential fields of the two rotors contribute to their aerodynamic interaction. The potential field of each rotor induces velocity disturbances at the position of the other rotor, which are periodic in the circumferential direction. Due to the relative rotation, these disturbances generate a periodic fluctuation of the blade loading of both rotors.

The tonal noise arising from the aerodynamic interaction between the rotors is called interaction noise (IN). It is emitted at frequencies that are linear combinations of the blade passing frequencies of the two rotors, that is, $f = h_1 \times BPF_1 + h_2 \times BPF_2$, with h_1,$h_2 \in \mathbb{N}$.

1.2.3 Broadband noise

The broadband noise is generated by unsteady sources characterized by a random behaviour. In open rotors, there are two mechanisms that produce significant levels of broadband noise [23,27,28]. The first one is the interaction of the flow turbulence with the leading edge (LE) of the blades. This interaction is due to the impingement of the inflow turbulence on both rotors and to the impact of the turbulent wakes shed by the front blades on the LE of the rear blades. In the second mechanism, the broadband noise is scattered by the trailing edge (TE) of the blades. In fact, CRORs typically develop a turbulent boundary layer over the blade surfaces, resulting in fluctuating blade loading at the trailing edge.

1.2.4 Contribution of the different noise sources to the total noise emission

Experimental and numerical studies have shown that different noise sources prevail over the others depending on the CROR operating conditions (see, e.g. [9,23,26,29]).

At cruise, the self-noise tones dominate the noise spectrum. In fact, although the radial sections of CROR blades are thin, the thickness noise is very intense due to the high relative speed. Moreover, Hanson and Fink [26] showed that the quadrupole sources have a significant impact when the blades operate in transonic regime, which is the case of CROR blades at cruise condition. On the other hand, the contribution of the loading sources to the rotor self-noise is comparatively weak since the blades are lightly loaded.

In general, the environmental impact of the acoustic emission is not a major issue during cruise flight. However, the engine noise causes annoyance to passengers and has to be duly considered in the design stage to limit the in-cabin noise.

At take-off and approach, the noise emitted by the CROR blades represents a critical issue for the communities living close to airports. Due to the high thrust required, the blades are heavily loaded during take-off. Consequently, the wakes of the front blades and the bound potential fields of the two rotors are very intense and generate high levels of periodic unsteady loading. Therefore, in this operating condition, the interaction noise tones due to the aeroacoustic interference of the two rotors are very strong if not dominant over the self-noise tones [9,23,29]. The mitigation of the IN at take-off is of primary importance in reducing the environmental impact of contra-rotating open rotors.

The broadband noise exhibits appreciable levels in all operating conditions. However, it has been demonstrated that the tonal noise components are significantly more intense than the broadband noise, especially at the lower frequencies [9,23]. Therefore, the contribution of the broadband noise is not considered in the present work.

1.3 Contribution of the front rotor tip vortices to the interaction noise

Among the flow structures responsible for the aerodynamic interaction of the two rotors, the tip vortices released by the front blades and impinging the rear blades are recognized as major drivers of IN at take-off condition [4,29,30]. They generate intense velocity disturbances in the circumferential direction that periodically impact the rear blades in the tip region, inducing high amplitude loading fluctuations. Moreover, the rotor tip is a very efficient noise radiator due to its high speed.

Peters and Spakovszky [29] showed numerically that the contribution of the rear blade tip to the interaction noise emission, due to the impingement of the tip vortices, can be as large as the contribution of the viscous wakes. Therefore, in a design strategy aimed at reducing the acoustic impact of CRORs, it is essential to account for the influence of the TVs.

1.4 Technologies for noise reduction

Effective technical solutions for noise reduction have already been identified during the development of the first generation of open rotors in the 80's and early 90's (see, e.g. [23,30]). Nevertheless, the progress in computational fluid dynamics (CFD) and computational aeroacoustics (CAA) methods, together with recent experimental efforts, has allowed assessing the effect of modern technologies for the reduction of the noise emitted by CRORs. A comprehensive overview of possible solutions for noise mitigation and their impact on rotor aerodynamics and structural issues is given by Negulescu [4] and Van Zante et al. [12].

1.4.1 Rotor self-noise reduction

The technical solutions for the abatement of the rotor self-noise emitted by each blade row can be summarized as follows:

- Swept blades: a spanwise shift between acoustic sources located at different blade stations is introduced by adopting blades with swept planforms. Thus, the acoustic signals emitted by different blade strips arrive out of phase at the observer position, resulting in partial self-interference and reduction in net noise. Moreover, the sweep

reduces the effective Mach number at which the airfoils operate, thus reducing the quadrupole noise [31]. However, the maximum sweep angle is limited by structural constraints.

- High blade count: it is desirable to maximize the blade counts in order to reduce the loading per blade, thus reducing the contribution of the loading noise. Also the induced losses diminish, resulting in a higher propulsive efficiency. Nevertheless, the maximum blade number is limited by constraints regarding the pitch change mechanism, blade solidity for reverse thrust, and engine weight. Future CRORs may have up to 12 blades per row.
- Large rotor diameter: the higher is the rotor diameter the lower is the disk loading (power per unit propeller annulus area) necessary to provide the required thrust. The local blade load is reduced, thus reducing the tonal loading noise. Also the efficiency benefits from a low disk loading since the losses are reduced. However, a large rotor diameter has a negative impact on the engine weight and requires a reinforced and heavier engine mount.
- Rotational speed: when increasing the blade rotational speed at constant propeller thrust, the projection of the blade lift force on the propeller axis increases, while its projection in the propeller plane decreases, thus enhancing the propeller efficiency. Nevertheless, when the blade tip approaches the transonic regime, thickness and quadrupole noise increase rapidly. Therefore, the propeller rotational speed must be chosen as a compromise between noise and efficiency requirements.
- Rear mounted pusher configuration: CROR engines can be installed on the wing or on the rear part of the fuselage in pusher configuration (see Figure 1.1). The latter is preferable to reduce the in-cabin noise perceived by the passengers at cruise. Indeed, thickness and quadrupole noise, which are dominant at cruise, exhibit the maximum amplitude close to the propeller rotation plane. Therefore, by mounting the engine in the aft part of the fuselage avoids exposing the cabin to the maximum intensity of the acoustic emission.

1.4.2 Interaction noise reduction

Technologies for the mitigation of the IN tones, which are particularly intense at take-off, have been explored and they are as follows:

- Rear rotor cropping: an effective mean to reduce the IN consists in avoiding the impingement of the FR tip vortices on the rear blades [30]. This can be achieved, at

least partially, by reducing the diameter of the RR (rotor cropping), so that the trajectory of the tip vortices lies outward the tip of the rear blades. At take-off, the stream-tube contraction is considerable due to the high thrust required. Therefore, limiting the impingement of the TVs on the rear blades requires a significant reduction in the rear rotor diameter. However, the vena contracta effect is slight at cruise. Therefore, the smaller is the RR diameter the larger is the amount of swirl kinetic energy not recovered by the rear rotor. Consequently, the radial extension of the rear blades must be tailored to achieve a compromise between cruise efficiency and noise mitigation.

- Increased axial spacing: the IN is sensitive to the axial distance between the two rotors. In fact, the intensity of the perturbations due to the FR wakes and the potential field of the two rotors decay moving away from the blades. Therefore, the unsteady loads decrease by increasing the spacing between the rotors. Even though the axial spacing has a minor influence on the propulsive efficiency, it has a large impact on the weight of the CROR.
- Unequal blade number: the front/rear self-rotor tones are emitted at integer multiples of the two separate $BPFs$, while interaction noise occurs at their linear combinations. For equal blade numbers and rotational speeds of the front and rear rotors, the self-noise tones of the RR, as well as the IN tones, are emitted at the same frequencies as those of the FR. For equal rotor speeds, unequal blade numbers with no common multiple factors should be adopted to spread the noise over different frequencies, thus reducing the overall acoustic emission. A difference of 2-3 blades for a total of 14-20 blades is suggested [4]. A difference of more than 3 blades would have a negative impact on the CROR efficiency.

1.4.3 The need for a multidisciplinary design approach

Research and development activities on CRORs have shown that adopting the best solutions for noise reduction leads to deterioration of CROR efficiency and also to structural issues. Thus, the geometrical features of the rotors, as well as their operating parameters, must be chosen properly to obtain the best compromise among acoustic, aerodynamic and structural requirements. Therefore, it is essential to consider the noise reduction in the earliest stages of a multidisciplinary design approach [29,32].

In a multidisciplinary design optimization, many CROR geometries and operating conditions have to be assessed, and hence a fast method to predict the noise emission is required.

1.5 Numerical methods for accurate noise predictions

To predict accurately the noise emitted by open rotors it is necessary to rely on CFD simulations for the computation of the unsteady flow field around the rotors and thus the acoustic sources. Then, accurate CAA methods have to be used to compute the acoustic pressure at any observer position.

The unsteady flow field around the CROR blades can be computed accurately by means of 3D Unsteady Reynolds Averaged Navier-Stokes (URANS) simulations. This numerical technique is based on the Reynolds averaging of the Navier-Stokes equations, which eliminates the turbulent fluctuations in the linear terms, while maintaining the time dependence of the averaged quantities. However, the turbulent fluctuations remain in the non-linear terms of the URANS equations, that is the Reynolds stresses, and a turbulence model needs to be introduced for the problem closure.

By means of URANS simulations, the steady (in the relative reference frame) and unsteady noise sources can be computed. These sources are used as an input to CAA models based on the acoustic analogy of Ffowcs Williams and Hawkings (FWH) [24], which is a generalization of the Lighthill equation accounting for the noise radiated by moving bodies [33,34]. Thus, the CAA models allow computing the time history of the acoustic pressure at the desired receiver positions.

The approach based on URANS simulations coupled with the FWH acoustic analogy provides accurate estimations of the noise emission. However, it requires very large computational times (some months on modern multi-processor computers). In fact, the URANS simulation must be advanced over a very large number of time steps, corresponding to several revolutions of the rotors, in order to obtain sufficient data for a spectral analysis of the computed signal, i.e., information on the noise tones. Therefore, due to its large computational burden, this approach is not compatible with a multidisciplinary optimization strategy.

1.6 Steady RANS simulations and mixing plane approach

3D steady Reynolds Averaged Navier-Stokes (RANS) simulations require considerably less computing time compared to URANS. To compute the approximate steady flow field past the CROR, the front and rear rotors are coupled using the mixing plane (MP) approach.

1.6.1 Mixing plane approach

Because of the aerodynamic interaction of the two blade rows in relative rotation, the flow field is inherently unsteady. Therefore, a mixing plane is introduced between FR and RR to

compute the approximate steady flow field in the rotating reference frame of each blade row (see Denton [35]). The flow quantities are azimuthally averaged at both sides of the MP interface, thus providing a uniform boundary condition in the circumferential direction for both rotors, which allows performing a steady state simulation.

RANS simulations conducted introducing the mixing plane concept give a very good estimate of the CROR aerodynamic performance (thrust, torque, efficiency, etc.) [4,15]. Moreover, they are rather fast, taking only few hours per simulation on a multi-processor computer. Therefore, the RANS mixing plane approach is suited to computations for the optimized design of open rotors.

1.6.2 Limitations regarding the noise computation

Steady RANS simulations are very attractive for the purpose of a multidisciplinary design strategy. However, only a partial assessment of the noise emission can be obtained. Indeed, the unsteadiness is completely suppressed at the MP and only the steady acoustic sources can be computed. This enables a fast estimation of the rotor self-noise tones only, whereas the IN cannot be evaluated. Therefore, in the context of a multidisciplinary optimization involving the acoustics of CRORs, the main issue to be addressed concerns the fast estimation of the unsteady loadings and the interaction noise tones.

1.7 Hybrid CFD/analytical methods for the fast prediction of the interaction noise tones

A relatively fast prediction of the IN tones can be obtained by means of hybrid CFD/analytical methods [36]. The basic concept behind hybrid methods is to exploit data extracted from a CFD simulation to calibrate analytical models of the velocity perturbations in space, i.e. the azimuthal perturbations, responsible for the unsteady aerodynamic interaction of the rotors (front blade wakes and rotor bound potential fields). The models assume that the azimuthal perturbations generated by each rotor are steady relative to it. However, due to the rotation, they are perceived by the other rotor as periodic velocity gusts that induce fluctuating aerodynamic loads.

The harmonics of the velocity gusts computed at the leading edge of the rotors are used as input to an analytical blade response model which gives the discrete spectrum of the unsteady blade loads (see Goldstein [37]).

After computing the harmonics of the unsteady loading, the acoustic emission is evaluated by means of an analytical noise propagation model in the frequency domain. A widely used model was proposed by Hanson, who initially developed a theory for the noise radiated by single-

rotating propellers [38], and then extended it to the contra-rotating configuration by including the contribution of the unsteady sources [39]. Hanson's model is a simplification of the FWH acoustic analogy, expressed in the frequency domain via Fourier transform, and it allows obtaining a very fast estimation of the tonal noise emitted by CRORs.

To summarize, the key steps of a hybrid CFD/analytical method for the prediction of the interaction noise are as follows:

1) conducting a CFD simulation;
2) using CFD data to calibrate analytical models of the azimuthal perturbations of velocity generated by the rotors;
3) computing the harmonics of the velocity perturbations at the leading edge of the rotors;
4) evaluating the harmonics of the unsteady loading by means of analytical blade response models;
5) calculating the radiated noise tones by means of an analytical noise propagation model in the frequency domain.

1.7.1 Literature review on hybrid methods

Hybrid CFD/analytical methods for the prediction of the IN from CRORs have been recently proposed by Ekoule et al. [40] and Carazo et al. [41]. Ekoule et al. developed analytical models of the azimuthal velocity perturbations generated by each rotor. The parameters of the models are calibrated exploiting flow velocity data extracted from URANS simulations and the harmonics of the velocity gusts are computed at the inlet of the two rotors. Carazo et al. single out the gusts due to the FR directly from the URANS solution and calculate their harmonics at the leading edge of the RR using the Fourier transform. Then, a blade response model and a modified version of Hanson's propagation model are used to compute the unsteady blade loads and the interaction noise, respectively.

Since the methods by Ekoule et al. and Carazo et al. are based on analytical models for the calculation of the unsteady loading and the noise radiation, they are considerably less time demanding compared to CAA models based on the FWH analogy. However, these methods circumvent only partially the issues related to the computational burden, since they rely on URANS simulations to obtain the necessary aerodynamic input.

Jaron et al. [42,43] proposed a method based on the RANS mixing plane approach for the fast computation of the IN. The velocity perturbations in space generated by each rotor are suppressed at the mixing plane. The concept behind the RANS-informed method of Jaron et al. is to extrapolate the perturbations through the MP to compute an approximate unsteady flow field

around the CROR. They developed analytical models describing the velocity perturbations generated by the front rotor viscous wakes and rotor bound potential fields. The parameters of the models are calibrated by fitting the azimuthal perturbations extracted from the RANS solution. Then, the perturbations are extrapolated through the MP, up to the LE of the two rotors. Finally, the harmonics of the extrapolated perturbations are used to compute the unsteady loading.

Grasso et al. [44] have recently presented the multidisciplinary optimization of the blade shape of a contra-rotating ducted fan, conducted using the extrapolation models of Jaron et al. to compute the IN tones. The RANS-informed method of Jaron et al. shows the potential to be successfully used for the fast prediction of noise in the context of a multidisciplinary optimization of CROR engines. However, this model relies on a 2D flow assumption, and a poor extrapolation is achieved in the region of the rear blade tip, thus affecting the prediction of the interaction noise tones. In fact, this region is influenced by the front rotor tip vortices, which are strongly three-dimensional flow structures. As already discussed, the TVs are major drivers of interaction noise at take-off and their influence must be assessed properly to obtain an effective noise mitigation.

Analytical models of the velocity perturbations ascribed to the FR tip vortices have already been developed by Kingan and Self [45] and Quaglia et al. [46]. These models can be calibrated using the solution of RANS simulations. Kingan and Self assume that the tip vortices follow a path of constant radius, thus neglecting the strong stream-tube contraction typical of take-off. This 3D effect is taken into account by Quaglia et al., who introduced a radially contracting helical path for the vortex centre. However, their TV model is defined in a coordinate system unwrapped on the radius of the blade-vortex impingement locus, leading to a distortion of the actual three-dimensional velocity field.

In view of the limitations of the models from literature, the need arises to develop a RANS-informed model capable of considering properly the contribution of the FR tip vortices to the aerodynamic interaction of the two rotors, as well as the contribution of the other flow structures (viscous wake and potential field).

1.8 Original contributions of this thesis

The objective of the present work is the development of an improved RANS-informed model for the fast prediction of CROR noise which properly accounts for the contribution of the FR tip vortices to the IN tones.

The background models considered for further improvements are the following ones:

1) RANS-informed model of Jaron et al. [42] for the extrapolation of the velocity perturbations generated by the FR beyond the mixing plane and the reconstruction of the unsteadiness at the inlet of the RR;
2) analytical blade response model proposed by Goldstein [37] for the calculation of the unsteady loading;
3) analytical noise propagation model by Hanson [39] for the computation of the acoustic emission.

The original contribution of the present thesis is supplementing the above models with a genuinely 3D semi-analytical model of the tip vortex (TV) flow field, with the aim of accounting for its contribution to the rotor interaction noise. The model, calibrated using data from steady RANS solutions, allows extrapolating the velocity perturbations due to the FR tip vortices beyond the mixing plane.

The trajectory of the TV centre is modelled by a helix that extends from the FR trailing edge (TE) to infinity downstream. Within an initial axial distance, the helix is allowed to radially contract and to have a variable pitch to account for stream-tube contraction and flow acceleration.

After defining the TV trajectory, the velocity induced by the vortex is computed numerically by means of the Biot-Savart law, modified to take into account the presence of a viscous core of finite radial extent [47]. Also, a velocity deficit locally tangent to the vortex trajectory is considered, being a typical occurrence in CROR blade tip vortices [18,46].

The TV model is calibrated using data from a steady RANS solution extracted from the FR trailing edge to the MP. The calibration procedure is divided into two steps. First, the unknown parameters of the analytical trajectory are balanced by fitting the TV centre path extracted from RANS. In the second step, the velocity parameters (vortex circulation, viscous core radius, and peak of velocity deficit) are identified. To make the identification of these parameters affordable in terms of computational burden, a specially developed calibration procedure based on the RANS vorticity fitting is proposed.

After calibrating the model parameters, the velocity ascribed to a single TV is evaluated at any point of the space. Thus, the velocity field due to the vortices released by all the FR blades is computed as the superposition of the contributions of the single blades. Therefore, the velocity perturbations in space due to the tip vortices, which are steady in the reference frame of the FR, are used for a dual purpose:

1) The TV perturbations are subtracted from the RANS velocity field between the FR trailing edge and the MP, thus removing the contribution of the tip vortices. Then, the 2D model of Jaron et al. is calibrated by fitting the resulting perturbations. This allows

improving the extrapolation of the flow structures described according to a 2D model (FR viscous wakes and potential field).

2) The TV perturbations are computed at the LE of the rear rotor, where they are added to the perturbations extrapolated by means of the 2D model.

Adopting this procedure, the contribution of both tip vortices and 2D flow structures to the unsteady loading on the rear blades is properly accounted for.

After reconstructing the perturbations beyond the mixing plane, the unsteady loading and the interaction noise emitted by the RR are evaluated using the aforementioned blade response and noise propagation models.

The CROR geometry considered in this work is the UDF F7/A7 with 8 x 8 blade count configuration (the numbering refers to the number of blades of the FR and the RR). Data found in literature [48,49] allowed reproducing the blade shape and the geometry of the nacelle.

The simulated operating condition is representative of take-off. The numerical simulations were conducted by means of the commercial software ANSYS Fluent. A RANS and a URANS simulation were performed. The former is employed to calibrate the analytical models, while the latter is used to validate the results of the proposed RANS-informed approach.

1.9 Structure of the thesis

This thesis is focused on the development of a RANS-informed model for the computation of the IN of CRORs that includes the effects of the FR tip vortices. The role of the data extracted from the RANS simulations is essential for the description of such a hybrid model. Therefore, the adopted CROR geometry and the setup of the numerical simulations are introduced first. Then, the background analytical models and the proposed tip vortex model are described.

Chapter 2 reports the procedure adopted to define the geometry of UDF F7/A7, based on data from literature, while Chapter 3 describes the setup of the RANS and URANS simulations.

The background models that represent the basis of the present work are illustrated in Chapter 4. First, the 2D extrapolation model of Jaron et al. is described. Then, the adopted blade response and noise propagation models are outlined.

The original contributions of the present thesis are presented in Chapter 5, which describes the tip vortex model and its interaction with the 2D extrapolation model from literature. After a general introduction, the modelling of the vortex trajectory and vortex velocity field is described. Then, the calibration procedure based on data extracted from RANS solutions is illustrated, together with preliminary results showing the velocity field ascribed to the tip vortices. Finally,

the procedure used to couple the tip vortex model with the 2D extrapolation model, based on the removal of the TV velocity perturbations from the RANS flow field, is illustrated.

The results of the present work are given in Chapter 6. First, the results of the numerical simulations are reported. Then, the results of the analytical models are illustrated, showing the outcomes of both improved model and purely 2D model, in order to assess the benefits achieved by considering the effect of the tip vortices. These results are organized as follows:

1) The extrapolated velocity perturbations, computed at the leading edge of the RR, are compared with URANS results to assess the reconstruction of the flow unsteadiness.
2) A comparison between the unsteady loading given by the blade response model and computed from the URANS blade pressure is presented.
3) The interaction noise tones emitted by the RR is evaluated and compared with high fidelity results obtained from the URANS simulation coupled with FWH. A comparison between the predicted noise emission and wind tunnel noise measurements found in the literature is also presented.

Finally, the conclusions of the present work are drawn in Chapter 7.

2 CROR GEOMETRY

The CROR geometry considered in this work is the historical UDF F7/A7, developed by General Electric (GE) during late 80's [48]. Acronym UDF denotes "UnDucted Fan", while F7 and A7 refer to the blades of the front rotor and rear (aft) rotor, respectively. The 8 x 8 blade count configuration was considered. A realistic shape of the nacelle and of the F7 and A7 blades has been reproduced, based on data found in literature [48,49].

2.1 Reproduction of the blade shape

The full scale UDF engine has rotor blade tip radii of $R_{T,1} = 1.778\ m$ and $R_{T,2} = 1.730\ m$ for the front rotor and rear rotor, respectively. The hub to tip ratio of the two rotors is $R_H/R_T = 0.425$. The engine was designed to operate at a cruise flight speed of Mach 0.72 and $35000\ ft$ altitude [48]. Data found in literature, and reported in Figures 2.1-2.3, allowed reproducing the main geometrical features of the front and rear blades [48,49].

Figure 2.1 refers to the F7 blade and shows the spanwise distributions of the normalized airfoil chord, $c_1/R_{T,1}$, and maximum airfoil thickness $t_{m,1}/c_1$. The distributions of the lift coefficient, $C_{L,1}$, and stagger angle, γ_1, at design cruise condition are also depicted. The stagger angle is measured from the axial direction and allows the blade twist to be defined. Analogous distributions for the A7 blade are given in Figure 2.2.

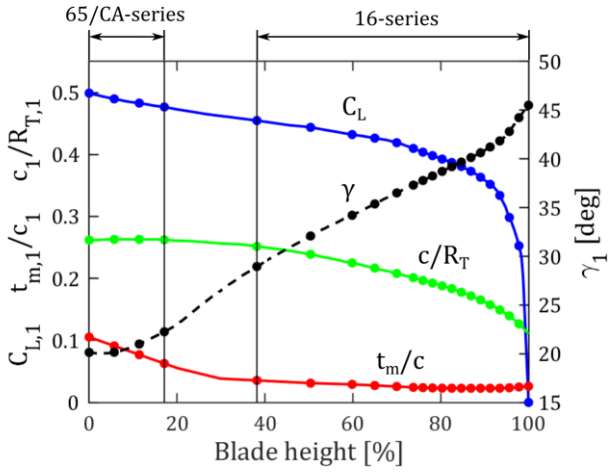

Figure 2.1 – Spanwise distributions of lift coefficient (C_L), chord-to-R_T ratio (c/R_T), thickness-to-chord ratio (t_m/c) and stagger angle (γ) for the F7 blade (from [48,49]).

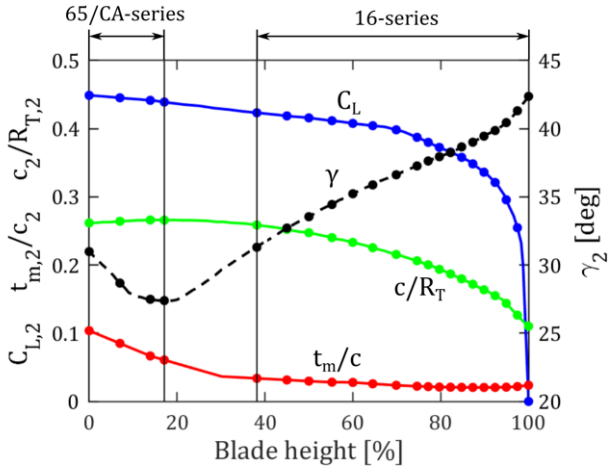

Figure 2.2 – Spanwise distributions of lift coefficient (C_L), chord-to- ratio (c/R_T), thickness-to-chord ratio (t_m/c) and stagger angle (γ) for the A7 blade (from [48,49]).

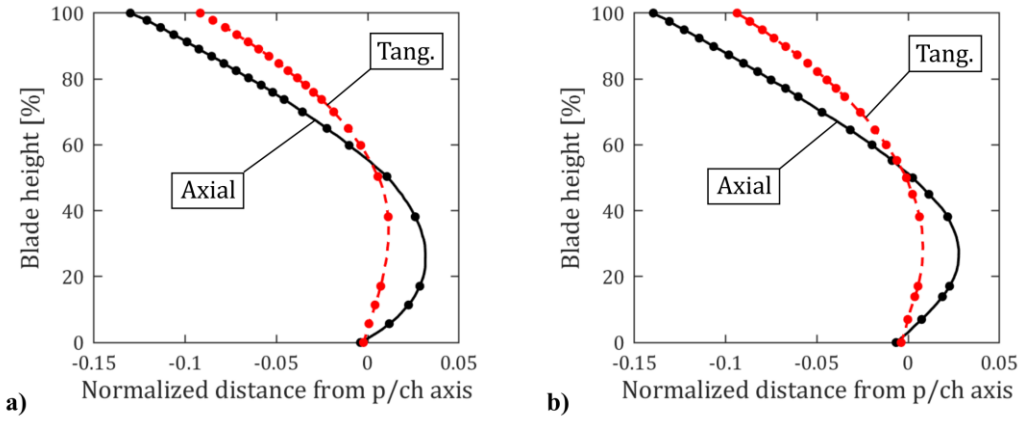

Figure 2.3 – Axial and tangential displacements defining the blade profile stacking line (from [48]). **a)** F7 blade, **b)** A7 blade.

In Ref. [48] the profile stacking line is provided in terms of axial and tangential displacements of the airfoil centroid with respect to the pitch change axis (PCA). The spanwise distributions of the airfoil displacements, normalized with respect to the rotor tip radius, are shown in Figure 2.3 for both front and rear blades. Note that these displacements refer to the cruise setting. In fact, at a different operating condition (e.g. take-off) the pitch angle of the blades is changed by the pitch change mechanism, thus varying the axial and tangential displacements of the airfoil centroid.

Since the actual airfoil geometry is not provided in the literature, the assumption has been made of using NACA 65-series profiles from the hub to 17.11 % of the blade height and NACA 16-series from 38.16 % to the blade tip (see Figure 2.1 and Figure 2.2). The intermediate blade region is filled with profiles obtained by a CAD interpolation procedure. This distribution of airfoil families is the same as that of the advanced propeller NASA SR-3 (see Rohrbach et al.

[31]). In fact, NASA SR-3 and UDF F7/A7 have been designed in the same period, and it is assumed they have similar geometric characteristics.

The aforementioned information allowed reproducing a realistic shape of the F7 and A7 blades. First, the spanwise distributions of lift coefficient, chord length and maximum thickness are used to define the airfoil shape at different radii along the blade span. Then, the airfoils are twisted according to the distribution of the stagger angle. Finally, they are stacked following the spanwise distributions of axial and tangential displacements of the centroids. The blade shape is then obtained by means of a CAD interpolation of the airfoils.

Both front and rear blades were obtained by stacking 22 airfoils along the blade height. The spanwise coordinates and the properties of these airfoils are identified by solid circles in Figures 2.1-2.3.

2.2 Reproduction of the nacelle shape

The geometry of the nacelle was reproduced using data found in Refs. [48] and [49]. The nacelle profile was extracted from Figure 2.4 [48] and is indicated by the solid line in Figure 2.6, where X_a and R_a are the axial and radial coordinates, respectively (axis X_a coincides with the CROR rotation axis and points in the downstream direction).

The axial coordinates of the pitch change axes of the two rotors, which define the location of the blades with respect to the nacelle, were extracted from Figure 2.5 ([49]). In this figure, the axial spacing between FR and RR (that is, the axial distance between the pitch change axes) refers to the baseline configuration of the UDF F7/A7 and corresponds to $\Delta X_a/R_{T,1} = 0.359$. The dash-dotted lines in Figure 2.6 show the axial positions of the pitch change axes for the baseline geometry. Axial coordinate $X_a = 0$ has been assigned to the position of the front rotor PCA.

2.3 Geometrical configuration considered

The CROR operating conditions considered in this work are representative of take-off. The benchmark for the simulated test case is an experiment conducted in the 9- by 15- Anechoic Wind Tunnel at NASA Lewis Research Center [50]. In that experiment, the pitch angle of the blades, i.e. the angle between the chord and the tangential direction at $R/R_T = 0.75$, was set to $\beta_1 = 36.2°$ and $\beta_2 = 38.4°$ for FR and RR, respectively. Moreover, an increased axial spacing of $\Delta X_a/R_{T,1} = 0.482$ was considered (the RR was shifted downstream). Therefore, the blade configuration considered in the present work has been modified with respect to the baseline one to match the NASA geometrical setting.

Figure 2.7 shows an overview of the reproduced CROR geometry, while views of the FR and RR in the rotation plane are depicted in Figure 2.8 a) and Figure 2.8 b), respectively. The absolute reference frame in cartesian coordinates, (X_a, Y_a, Z_a), and cylindrical coordinates, (X_a, R_a, Ψ_a), is also shown, together with the directions of the angular velocities of front rotor, Ω_1, and rear rotor, Ω_2.

Figure 2.9 and Figure 2.10 provide detailed pictures of the front and rear blades, respectively. In these figures, the PCA (indicated by a dash-dotted line) is aligned with the axis Z_a.

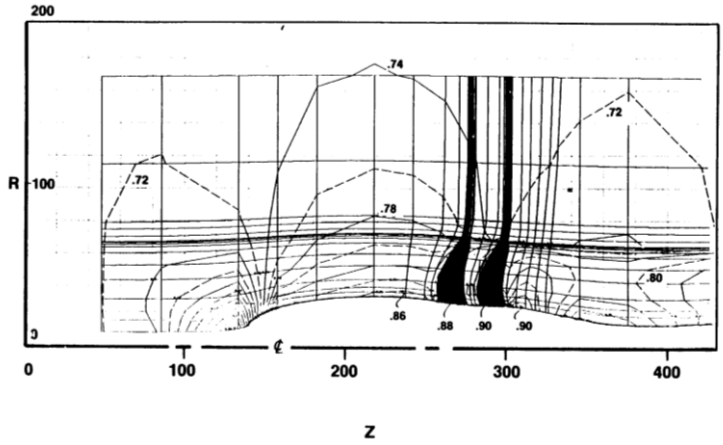

Figure 2.4 – Picture taken from Ref. [48], which includes the nacelle profile.

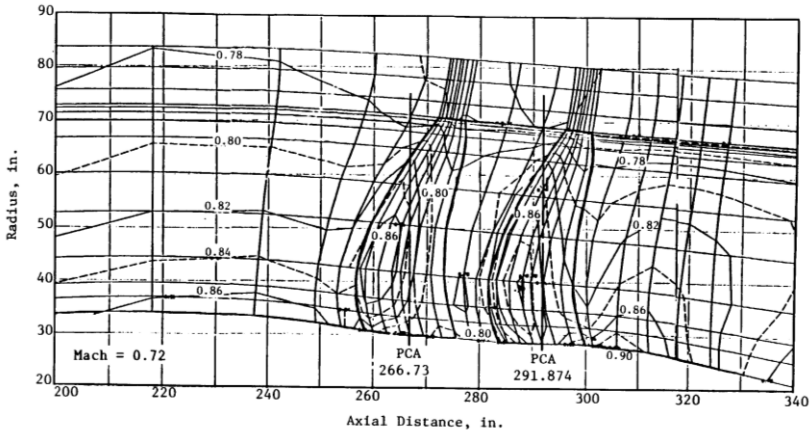

Figure 2.5 – Picture taken from Ref. [49], which includes a detail of the nacelle profile and the axial locations of the pitch change axes of FR and RR.

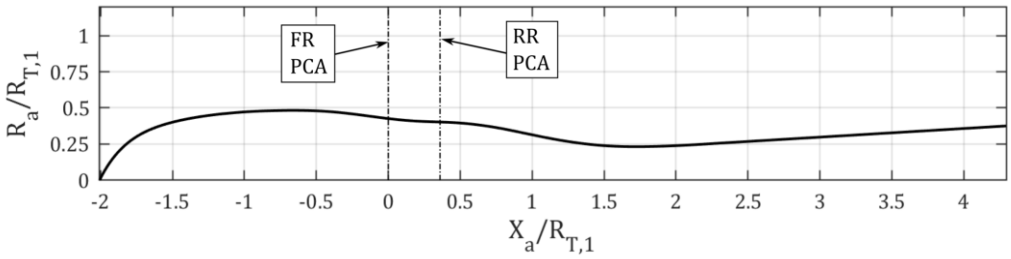

Figure 2.6 – Curve defining the nacelle profile (solid line) and axial positions of the pitch change axes of FR and RR (dash-dotted lines) for the UDF F7/A7 baseline configuration.

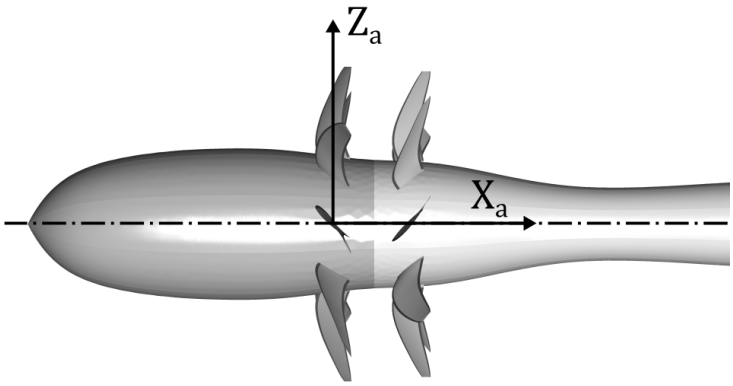

Figure 2.7 – Overview of the reproduced CROR geometry.

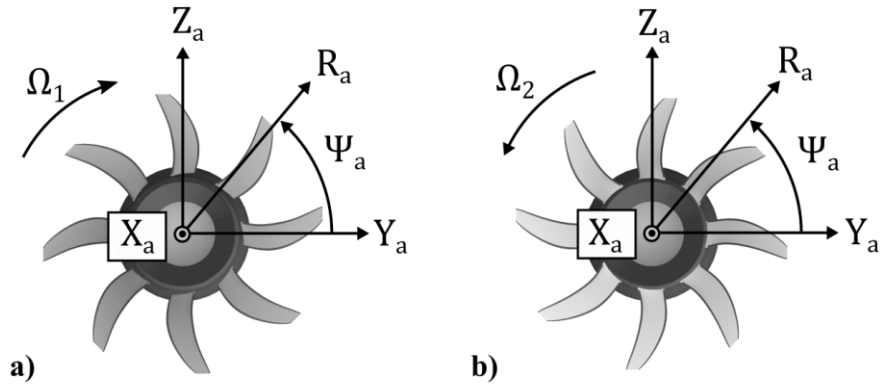

Figure 2.8 – View of the rotors in the rotation plane. **a)** front rotor, **b)** rear rotor.

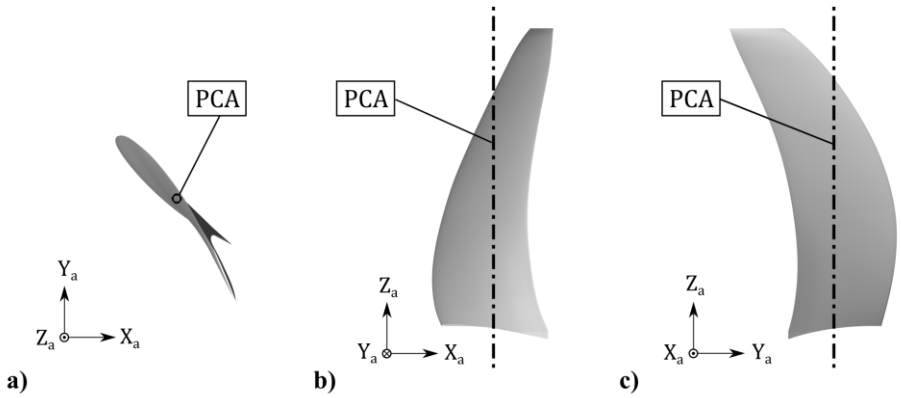

Figure 2.9 – Shape of the F7 blade. **a)** projection on (X_a, Y_a) plane, **b)** projection on (X_a, Z_a) plane, **c)** projection on (Y_a, Z_a) plane.

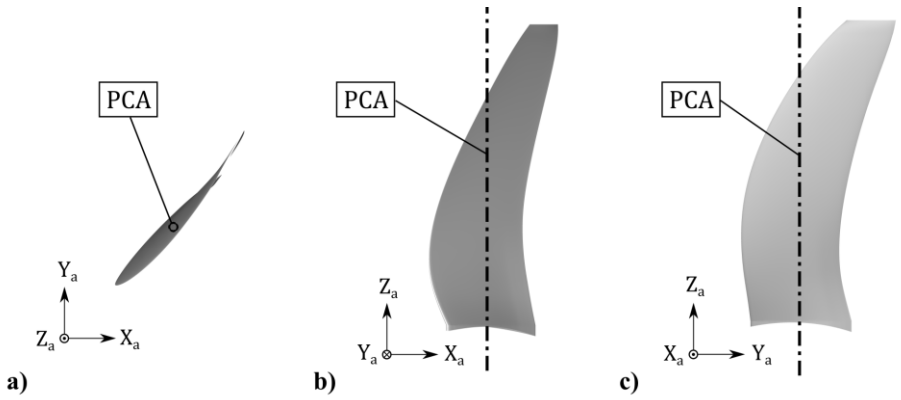

Figure 2.10 – Shape of the A7 blade. **a)** projection on (X_a, Y_a) plane, **b)** projection on (X_a, Z_a) plane, **c)** projection on (Y_a, Z_a) plane.

3 NUMERICAL MODELS

The RANS and URANS numerical simulations have been performed using commercial software ANSYS Fluent [51]. A second-order accurate pressure-based coupled solver and the $\kappa - \omega$ SST turbulence model were used. In the URANS simulation, the time integration relied on a full implicit, second-order accurate, numerical scheme with constant time-step size.

The computational domain includes a single blade passage for each rotor and periodic boundary conditions are applied at the lateral faces of the domain. The sketch in Figure 3.1 shows the axial and radial extension of the domain. The inlet and outlet boundaries are located at axial distances of 12 and 24 FR tip radii from the FR pitch change axis, respectively, while the far field boundary is located at 13 FR tip radii from the rotation axis. The boundary conditions applied to the inlet, outlet and far field surfaces are of "pressure-far-field" type, where the freestream Mach number and static conditions are specified, and the Riemann invariants are used to determine the flow variables at the boundary. The no-slip condition is enforced on the blade surfaces, while the nacelle surface is modelled as a zero-shear wall. It was decided to neglect the boundary layer of the nacelle to avoid a grid refinement at its surface, thus significantly reducing the computational burden of the simulations. Considering that the noise emission depends on the square of the Mach number of the sources relative to the observer [39], and since the nacelle boundary layer and the secondary flows would impinge the blades at the hub region, where the rotational speed is low, it is believed that treating the nacelle as a zero-shear wall has negligible effects on the noise prediction.

The computational grid was built so as to be used to perform both the RANS and URANS simulations. The URANS simulation is conducted by means of the sliding mesh approach, in which the two portions of the computational grid enclosing the front and rear blades are allowed to rotate relative to each other. To prevent numerical instability, the rotating grids are not extended radially up to the far field boundary, but they are divided into two regions of limited radial extent, surrounded by a non-rotating region that extends up to the domain external boundaries. However, when the computational domain includes a single blade passage, ANSYS Fluent is not capable of performing a sliding mesh simulation involving three adjacent computational grids with different rotational speeds (two contra-rotating grids and a fixed grid). Therefore, the two rotating grids cannot be adjacent, but they must be separated by a portion of the fixed grid. The RANS

simulation requires that the computational grid is divided into two portions, one for each rotor, separated by a mixing plane.

To satisfy all the aforementioned requirements, thus allowing the use of the same computational grid for both RANS and URANS simulations, the computational domain is divided into four cell volumes, as shown in Figure 3.1. The volumes identified by A and B (short-dashed lines in Figure 3.1) enclose the FR blade and the RR blade, respectively, and their radial and axial lengths are 1,5 and 0,73 FR tip radii. The surrounding volumes C and D extend up to the domain boundaries and their interface (long-dashed line) is placed at the mixing plane (MP) location. Figure 3.2 shows a three-dimensional view of the domain, and the blue surfaces in the detailed view represent the interfaces between internal and external cell volumes. All the pairs of adjacent surfaces at the interfaces are conformal, that is, the coordinates of the nodes on the two sides are coincident when the lateral faces of the cell volumes are aligned (as shown in Figure 3.2).

In the RANS simulation, the node pairs at the interfaces between internal (A,B) and external (C,D) volumes are merged into single nodes. Therefore, no interpolation is necessary, and each of couples A-C and B-D is treated as a single computational volume. The surfaces at the interface between C and D, named FR outlet and RR inlet, are kept separated and they are coupled via the mixing plane technique. The azimuthal averaging of the flow quantities is performed along 2200 circumferences on both sides of the MP interface. The averaged profiles at the FR outlet are used as boundary conditions for the RR inlet and vice-versa. In this way, the fluxes of the azimuthally averaged flow variables are conserved through the MP, while any flow unsteadiness due to circumferential variations is removed, allowing a steady flow computation. The computational

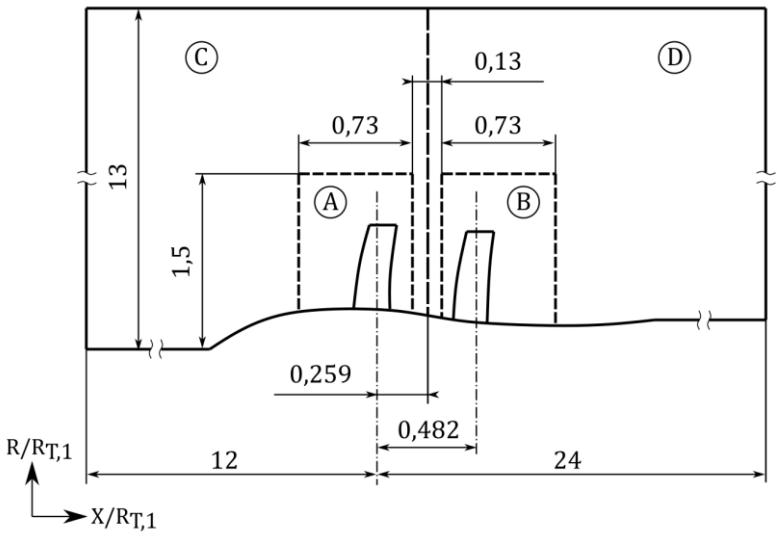

Figure 3.1 – Extent of the computational domain and cell volumes.

meshes are fixed to the blades and their rotational speeds are specified assigning a rotating frame to each rotor.

To perform the URANS simulation, external volumes C and D are treated as a single computational grid by merging the nodes at their interface. The sliding mesh approach is used and the computational grids of the volumes enclosing the two rotors (A and B) are put into rotation, while the external volume C+D is kept fixed in the absolute reference frame. Since during the rotation the coordinates of the nodes at the sliding surfaces do not match, the flow variables are interpolated at the interfaces between fixed (C+D) and rotating (A,B) volumes.

The volumetric mesh is unstructured and consists of polyhedral cells, with the blade surfaces surrounded by 20 polyhedral prism layers. The first layer has a constant height, while the offset of the last layer is set to 12% of the base mesh size. The offset of the intermediate layers is defined by a geometric progression. By means of the prism layers, a better refinement of the grid can be obtained at the blade surfaces. Moreover, depending on the computed local value of y^+, the numerical solver switches automatically from a low-Reynolds ($y^+ < 1$) to a wall function treatment of the near-wall regions. In Figure 3.3, a portion of the prism layers on the FR blade has been removed to visualize the height of the layers and the shape of the prism cells, indicated by red lines. The values of y^+ on the blade surface resulting from the simulations vary from a minimum of 0.1 to a maximum of 8.

A preliminary mesh-dependence analysis of the numerical solution allowed an appropriate grid refinement to be selected, resulting in an overall cell count of approximately 11 million. As shown in Figure 3.4, the computational grids are properly refined in the region between the two

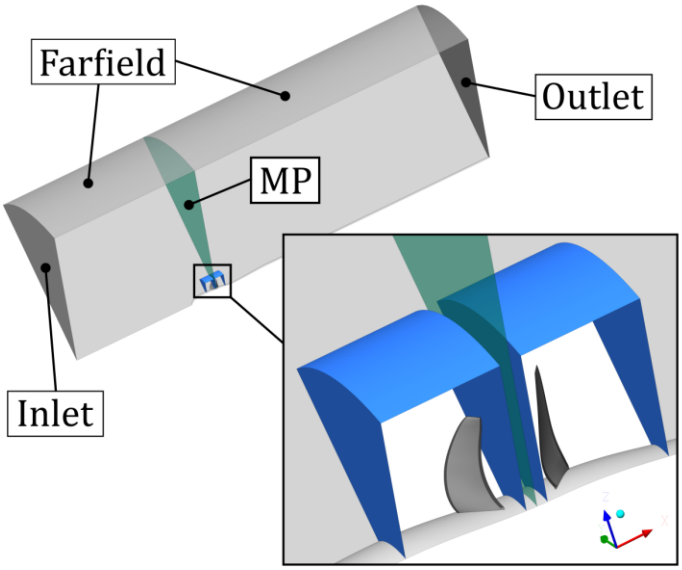

Figure 3.2 – Overview of the computational domain and detail of the internal cell volumes.

rotors in order to minimize the numerical diffusion and to obtain a good resolution of the wake flow from the front rotor.

In the URANS simulation, the time step size was set so that the mutual blade passage takes place within 60 time steps. It is short enough to minimize the numerical diffusion, so ensuring an accurate wake convection through the domain interfaces.

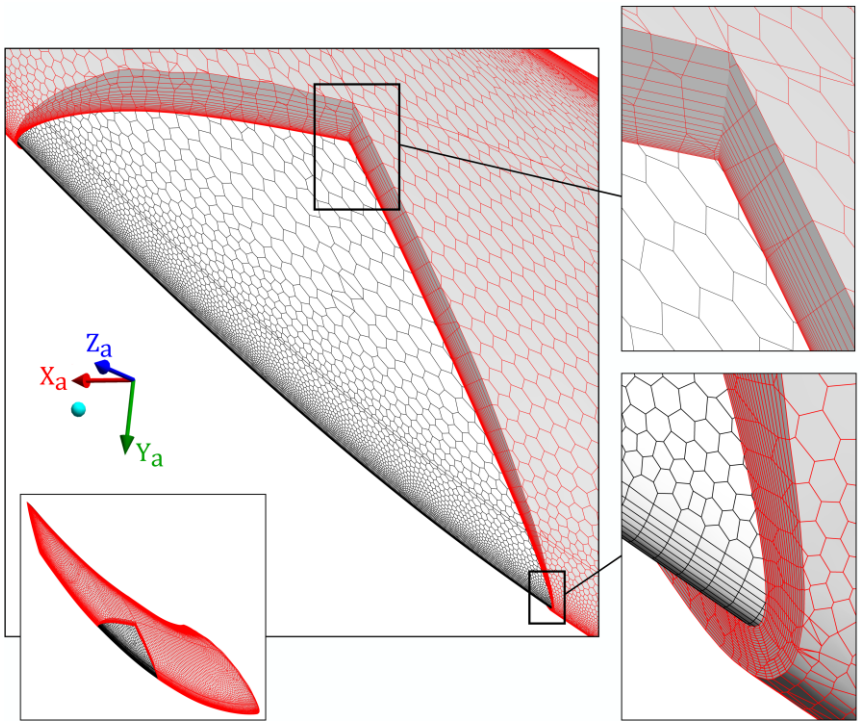

Figure 3.3 – Section of the prism layers surrounding the FR blade. The cutting surfaces are $X_a = 0$ and $R_a = 0.75R_{T,1}$.

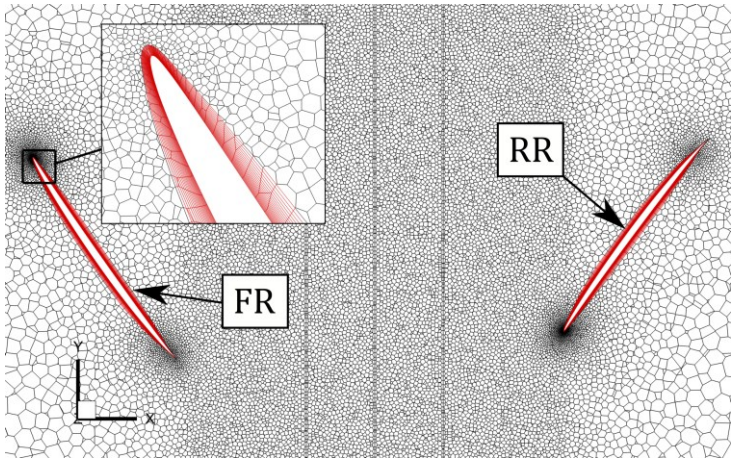

Figure 3.4 – Mesh between the rotors on cylindrical surface $R_a = 0.75R_{T,1}$.

4 BACKGROUND ANALYTICAL MODELS

The background analytical models considered for the development of the present RANS-informed model are outlined in this chapter. The detailed derivations of these models are reported in Appendices A, B and C.

4.1 2D extrapolation model

The RANS-informed 2D model of Jaron et al. [42], balanced on data extracted from RANS solutions, allows extrapolating the azimuthal perturbations of flow velocity generated by the FR through the mixing plane. Then, the harmonics of the perturbations computed at the leading edge of the RR can be used as an input to blade response models, and a fast prediction of the IN tones emitted by the rear rotor can be obtained.

At any given radius, the velocity field around the CROR blades can be decomposed into its azimuthal average, $\overline{\boldsymbol{v}}$, and circumferential perturbations $\boldsymbol{v}'$. The assumption of Jaron et al. [42] is that $\boldsymbol{v}'$ in the region between the FR trailing edge and the MP can be described as a superposition of the viscous wake and potential flow perturbations generated by the front rotor. The model represents the azimuthal perturbations in a reference frame rotating with the FR (see Figure 4.1), where they are steady. The origins of the relative reference frame (X, Y, Z) and absolute reference frame (X_a, Y_a, Z_a) are coincident and the Z axis is aligned with the PCA of one of the front blades.

The circumferential profile of the velocity perturbations is decomposed into harmonics using different velocity distributions for the wake and potential flow contributions. The viscous wake is represented by a Gaussian distribution and the related harmonic superposition is given by

$$u'_w(X,\Psi) = 2 \cdot \sum_{h=1}^{N} -u_{w0} e^{-\pi h^2 [W_0^2 + K(X - X_{TE,1})]} \cdot \cos\left[hB_1 \left(\Psi - \frac{\tan \beta_{rel}}{R} \left(X - X_{TE,1} \right) \right) + \varphi_w(h) \right], \tag{4.1}$$

where X and Ψ are the axial and azimuthal coordinates, respectively, of the reference frame attached to the FR (see Figure 4.1). X is measured in the downstream direction, and $X_{TE,1}$ is the axial coordinate of the FR trailing edge. Term u_{w0} determines the amplitude of the velocity

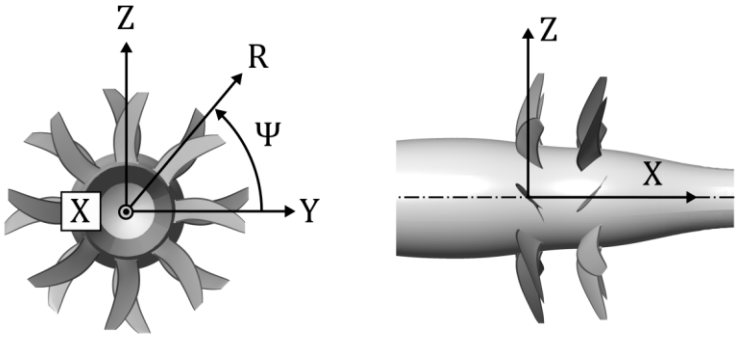

Figure 4.1 – Cartesian coordinates (X, Y, Z) and cylindrical coordinates (X, R, Ψ) in the relative reference frame of the front rotor.

deficit at the TE, W_0 is the non-dimensional wake width at TE, and K is a coefficient that accounts for the wake expansion in the downstream direction. Since the viscous wake generated by a lifting airfoil exhibits an asymmetric distribution of the velocity deficit between the pressure and suction side [52], the zero-phase property of the harmonics of a classic Gaussian distribution is relaxed and a different phase, $\varphi_w(h)$, is introduced for each harmonic. The exponential term in Eq. (4.1) provides the decay of the wake amplitude moving away from the rotor. β_{rel} is the outflow angle in the reference frame of the front rotor and term $\tan\beta_{rel}\,(X - X_{TE,1})/R$ accounts for the convection of the wake due to the swirl of the flow.

The contribution of the potential flow perturbations is derived from the theory of waves in ducted swirling flows [53] and is given by

$$u'_p(X,\Psi) = 2 \cdot \sum_{h=1}^{N} u_{p0}(h) e^{-hB_1 \frac{\sqrt{1-M_{rel}^2}}{1-M_X^2} \frac{|X-X_{TE,1}|}{R}} \cdot \cos\left[hB_1 \left(\Psi - \frac{M_X^2}{1-M_X^2} \frac{\tan\beta_{rel}}{R} \left(X - X_{TE,1}\right) \right) + \varphi_p(h) \right]. \tag{4.2}$$

Terms $u_{p0}(h)$ and $\varphi_p(h)$ are the amplitude at the TE and the phase of the harmonic of order h, respectively. The presence of term $M_X^2/(1-M_X^2)$ shows that the potential field rotates with a different swirl compared to the viscous wake. Furthermore, the exponential term shows that the amplitude decay depends also on the number of blades, B_1. The application of this model to an unducted fan is an acceptable approximation as long as the radial velocity components are small compared to the other ones, which is not the case in the tip vortex region. The detailed derivation of Eqs. (4.1) and (4.2) is reported in Appendix A.

The total velocity perturbation is the superposition of the two contributions in Eqs. (4.1) and (4.2), i.e., $u'(X,\Psi) = u'_w(X,\Psi) + u'_p(X,\Psi)$, and the parameters that have to be balanced using the RANS solution are u_{w0}, W_0, K, $\varphi_w(h)$, $u_{p0}(h)$ and $\varphi_p(h)$. The sum of $N = 40$ harmonics was considered. Therefore, the numbers of parameters to be calibrated for the viscous wake and potential field models are $N_{par,w} = 3 + N = 43$ and $N_{par,p} = 2N = 80$, respectively.

To account for the effect of the stream-tube contraction, the extrapolation paths are defined by streamlines computed from the azimuthally averaged flow field [42]. 55 streamlines were considered (see Figure 4.2) and a set of unknown coefficients had to be determined for each of them. To do so, velocity profiles $v(X_i,\Psi)$ were extracted along the streamlines at 8 axial locations, X_i, from the TE of the front rotor to the MP, and the perturbations $v'(X_i,\Psi) = v(X_i,\Psi) - \bar{v}(X_i)$ were calculated. The black circles in Figure 4.2 give an example of extraction locations along one of the streamlines. Then, the unknown coefficients for each streamline were computed by fitting the model velocity u' with v', that is by solving the following non-linear least squares problem:

$$\sum_{i=1}^{8} [u'(X_i,\Psi) - v'(X_i,\Psi)]^2 = \min . \tag{4.3}$$

The solution of the minimization problem (4.3) was performed using the Trust-Region-Reflective (TRR) algorithm available in MATLAB, due to its efficiency and robustness in solving large-scale minimization problems. For each streamline, the TRR algorithm was initialized with 120 different values of each variable to increase the chances of finding the global minimum.

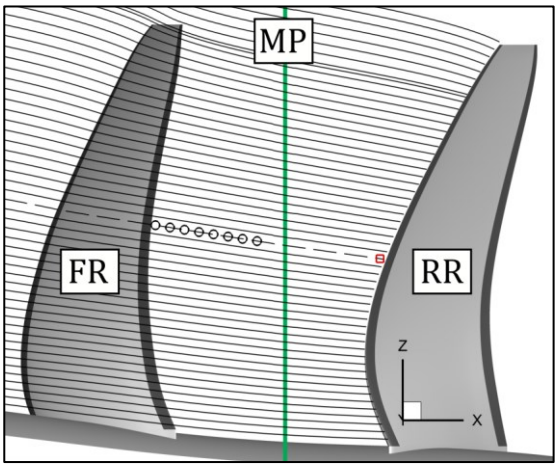

Figure 4.2 – Streamlines defining the extrapolation paths. The black circles represent the (X,R) locations of the velocity extraction points along one of the streamlines. The red square indicates the point where the velocity perturbations are extrapolated.

Once the unknown parameters have been balanced, it is possible to compute $u'(X_{LE,2}, \Psi)$, at the LE of the rear rotor. The red square in Figure 4.2 represents an example of extrapolation location along one of the streamlines.

Since Eqs. (4.1) and (4.2) are valid for any velocity component, the identification of the parameters and the extrapolation of the perturbations were performed separately for the axial, tangential and radial velocity components.

Due to the stream-tube contraction, the streamlines that reach the LE of the rear rotor in the tip region, i.e., streamlines 51 to 55, do not cross the TE of the front rotor and, consequently, the influence of the viscous wake should not be considered. Therefore, in the present implementation only the potential field contribution, u'_p, is fitted along these streamlines. Thus, the total number of model parameters to be balanced for each velocity component is $N_{par,tot} = 50(N_{par,w} + N_{par,p}) + 5N_{par,p} = 6550$.

In order to add the contribution of the front rotor to the IN, Jaron et al. [43] developed their model further to extrapolate also the perturbations generated by the rear rotor in the upstream direction. In this case, only the potential field contribution is considered. However, the potential field has a limited effect on the IN. This is especially true for modern CRORs, characterised by large axial spacings. In fact, the amplitude of the velocity perturbations ascribed to the bound potential field decay rapidly moving away from the rotor. Therefore, the upstream extrapolation is not considered in this work and the focus is on the modelling of the perturbations generated by the FR.

Due to the essentially 2D nature of the models described by Eqs. (4.1) and (4.2), the quality of the fitting, and consequently of the extrapolation, is poor at the outer portion of the blade. In fact, in this region the influence of the tip vortex, which is a strongly three-dimensional flow structure, becomes important. Moreover, a correct modelling of the harmonics of the velocity at the outer radii, where the peripherical rotor speeds are high, is particularly important to obtain a correct noise prediction. Therefore, a tip vortex model has been developed to integrate the extrapolation model of Jaron et al.. The objective is to single out the flow field generated by the TV, so that the related velocity perturbations can be directly computed. Furthermore, the TV velocity can be subtracted from the RANS solution, thus removing the three-dimensional effects and improving the extrapolation of the 2D model.

4.2 Blade response model

The azimuthal perturbations of flow velocity generated by the front rotor, $\boldsymbol{v}'_{FR}(X, R, \Psi)$, are detected as time perturbations in the reference frame of the rear rotor. They affect the rear blades

causing the fluctuating blade loads responsible for the emission of the IN tones from the RR. The extrapolation model allow computing $\boldsymbol{v'}_{FR}$ beyond the mixing plane, thus reconstructing the unsteadiness at the leading edge of the rear blades. Then, the fluctuating loads on the RR blades can be computed by means of two-dimensional unsteady airfoil theories [36,37,40].

In this work, a blade response model proposed by Goldstein [37] is adopted to compute the unsteady lift due to the impingement of the velocity perturbations on the RR blades. The model allows computing the unsteady lift acting on an isolated airfoil due to the impingement of a velocity perturbation. It is assumed that the perturbation, usually called a gust, is convected by a uniform 2D flow relative to the airfoil. The amplitude of the gust is considered small with respect to the uniform mean flow velocity. Moreover, the gust is frozen, i.e., it is spatially non-uniform but steady in a reference frame moving with the mean flow. The blade response model relies on the assumption of thin airfoil, having a small camber and a small angle of attack with respect to the mean flow. This implies that the gust is not modified by the presence of the airfoil and the flow field can be considered linear. It is further assumed that the upwash component of the velocity gust, that is, the component perpendicular to the mean flow direction, is responsible for the loading fluctuation on the airfoil. The model considers the effects of compressibility, that become significant for high frequency gusts, which is usually the case of the perturbations impinging the CROR blades.

In view of the 2D assumptions of the blade response model, the rear blade is divided into radial sections, which are treated as isolated thin airfoils. 55 blade sections are considered along the blade span at the radial positions where the averaged streamlines, used to extrapolate the front rotor perturbations, approach the RR leading edge. The model is applied separately to each blade section, starting from the evaluation of the uniform mean flow and the frozen gust of upwash velocity at the leading edge of the RR. The mean flow is computed from the RANS solution, while the extrapolated velocity perturbations are considered as the frozen gust convected by the mean flow.

Consider a blade section at radius R in the unwrapped cylindrical section of the RR shown in Figure 4.3. It is assumed that a uniform flow $\boldsymbol{W}_1$ relative to the FR, computed as:

$$\boldsymbol{W}_1 = \bar{v}_{RANS,X}\left(X_{LE,2}, R\right)\boldsymbol{e}_X + \left[\bar{v}_{RANS,\Psi}\left(X_{LE,2}, R\right) - \Omega_1 R\right]\boldsymbol{e}_\Psi \,, \tag{4.4}$$

is convecting the frozen perturbations $\boldsymbol{v'}_{FR}\left(X_{LE,2}, \Psi\right)$ computed at the LE of the airfoil (see the contours in Figure 4.3). Due to the relative rotation of the two rotors, the perturbations impact the RR airfoil with relative velocity

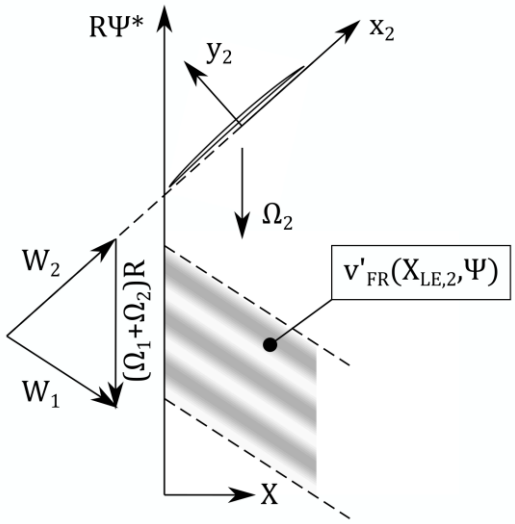

Figure 4.3 – Blade section of the rear rotor in the unwrapped reference frame.

$$\boldsymbol{W}_2 = \boldsymbol{W}_1 - \boldsymbol{\Omega}_{rel} \times \boldsymbol{R} = \boldsymbol{W}_1 - (-\boldsymbol{\Omega}_1 + \boldsymbol{\Omega}_2) \times \boldsymbol{R}\,. \tag{4.5}$$

The reference frame (x_2, y_2), attached to the RR airfoil, is aligned with the direction of $\boldsymbol{W}_2$ and centred at the midchord. The upwash component $v'_{y_2}(X_{LE,2}, \Psi)$ of the velocity perturbations is simply obtained by projecting $\boldsymbol{v}'_{FR}$ along direction y_2.

The blade response model is linear and gives the harmonic components of the lift induced by sinusoidal gusts of the upwash velocity. Therefore, the circumferential profile of v'_{y_2} is processed by DFT (Discrete Fourier Transform) to obtain its harmonic content:

$$v'_{y_2}(X_{LE,2}, \Psi^*) = \sum_{h=-H}^{H} |v_{y_2}(h)| e^{i[hB_1\Psi^* + \Psi^*(h)]}\,, \tag{4.6}$$

where $|v_{y_2}(h)|$ and $\Psi^*(h)$ are the amplitude and phase of the harmonic of order h, respectively. Note that the harmonics must be defined in the azimuthal coordinate Ψ^*, which is measured in the direction of rotation of the FR (see Figure 4.3). The Fourier coefficients of the lift force per unit span are then computed according to the formula [37]:

$$L_2(h) = \pi\rho_0 c_2 |v_{y_2}(h)| |\boldsymbol{W}_2| S_c(\sigma_{x_2}, M_{rel,2}) e^{i\left(k_{x_2}\frac{c_2}{2} + \phi\right)}\,, \tag{4.7}$$

the complete derivation of which is reported in Appendix B. In Eq. (4.7), $S_c(\sigma_{x_2}, M_{rel,2})$ is the high-frequency approximation of the compressible Sears function [37],

$$S_c\left(\sigma_{x_2}, M_{rel,2}\right) = \frac{e^{-i\sigma_{x_2}}}{\sigma_{x_2}\pi}\sqrt{\frac{2i}{M_{rel,2}}}F\left(\sqrt{\frac{4\sigma_{x_2}M_{rel,2}}{\pi\left(1+M_{rel,2}\right)}}\right), \tag{4.8}$$

which depends on the relative Mach number, $M_{rel,2} = |\boldsymbol{W}_2|/a_0$, and the reduced frequency, $\sigma_{x_2} = hB_1(|\Omega_1| + |\Omega_2|)c_2/2\,|\boldsymbol{W}_2|$. Function F is the complex Fresnel integral. The validity condition of this approximation, $M_{rel,2}\left|\sigma_{x_2}\right|/\left(1 - M_{rel,2}^2\right) > 1$, is satisfied at all the blade sections considered.

In the blade response model, the phases of the upwash gusts are relative to the midchord point. In view of this, the exponential term in Eq. (4.7) is introduced to account for the actual phase of each harmonic of the lift (see Appendix B). This term includes two shifts, ϕ and $k_{x_2}c_2/2$. The former represents the phase of the upwash harmonic at the leading edge of the airfoil:

$$\phi(h) = hB_1\Psi^*_{LE,2} + \Psi^*(h)\,, \tag{4.9}$$

while the latter accounts for the phase shift between the leading edge and the midchord through the chordwise wavenumber, $k_{x_2}(h) = 2\sigma_{x_2}(h)/c_2$.

Finally, the total unsteady lift per unit area is computed by means of the following inverse DFT:

$$L'_2(t) = \sum_{h=-H}^{H} L_2(h)e^{-ik_{x_2}|\boldsymbol{W}_2|t} = \sum_{h=-H}^{H} L_2(h)e^{-ihB_1(|\Omega_1|+|\Omega_2|)t}\,. \tag{4.10}$$

Equation (4.10) shows that the frequencies of the unsteady lift depend on the number of blades of the FR, which generates the velocity perturbations, and on the relative angular velocity of the two rotors, as expected. It should be noted that reconstruction $L'_2(t)$ in the time domain is not a necessary information for the fast noise computation. In fact, the noise propagation model is formulated in the frequency domain, and it requires the knowledge of only the Fourier coefficients, $L_2(h)$, of the blade loading [39].

Although Eq. (4.7) was derived under the assumptions of 2D flow, slightly cambered thin airfoil and small angle of attack, it was considered acceptable for the present application, where the blade profiles have small thickness and camber, and the angles of attack are moderate. Concerning the 2D approximation, Adamczyk [54] shows that the lift response is a weak function of the encounter angle in the case of an oblique gust impacting an infinite swept wing.

4.3 Noise propagation model

In the present work, the analytical model in the frequency domain proposed by Hanson [39] is used for the estimation of the far field noise emitted by the rear rotor. The unsteady loading given by the blade response are used as an input to the noise propagation model, which allows computing the IN tones at frequencies that are linear combinations of the $BPFs$ of the two rotors.

The Hanson's model is a simplification of the Ffowcs Williams-Hawkings equation [24,38], which gives the pressure disturbances generated by acoustic sources distributed on rigid surfaces in arbitrary motion. Hanson assumes that the rotor blades are thin and thus considers the acoustic sources as distributed on the helicoidal surface swept by the blade PCA in forward motion with speed v_0 and rotating with angular speed Ω_2 [38] (see Figure 4.4). Then, the blade of the RR is divided into radial sections and the useful geometrical quantities and acoustic sources are defined in a helicoidal coordinate system (γ, ξ), having the origin along the PCA and locally aligned with the advancing speed of the blade section, $\boldsymbol{V}_{adv,2}(R)$, as depicted in Figure 4.5 b). γ and ξ are arc lengths measured on a cylindrical surface of radius R. Notice that $\xi = 0$ corresponds to the helicoidal surface. The noise sources are represented in the frequency domain via Fourier transform in space, along direction γ, and time. The computation of the noise emission relies on the spanwise integration of the geometrical quantities and the acoustic sources represented in the frequency domain.

The acoustic pressure is computed at points with polar coordinates (ϱ, φ), where angle φ is equal to 90° in the plane of rotation of the RR (see Figure 4.5 a)). The coordinate system (ϱ, φ) is in forward motion with the rotor with speed v_0. In the original formulation of the model, which is derived in Appendix C, the time signal of the acoustic pressure is given by the superposition of the harmonics at frequencies $f = h_1 BPF_1 + h_2 BPF_2$, for $h_1, h_2 \in \mathbb{Z}$ (see equation (C.16) in Appendix C) [39]. The Fourier coefficient, $P_{h_1,h_2}(\varrho, \varphi)$, of the harmonic of orders h_1, h_2 is given by the following equation:

$$P_{h_1,h_2}(\varrho, \varphi) = \frac{-i\rho_0 a_0^2 B_2 D_2}{8\pi\varrho(1 - M_0 \cos\varphi)} \times \int_{hub}^{tip} M_{adv,2}^2 e^{i(\phi_l + \phi_s)} \mathcal{J}_{h_2 B_2 - h_1 B_1}(q) \left[k_\gamma \frac{C_{Dh_1}}{2} \Psi_{Dh_1} + k_\xi \frac{C_{Lh_1}}{2} \Psi_{Lh_1} \right] d\left(\frac{R}{R_{T,2}}\right), \quad (4.11)$$

and the pressure amplitude of the IN tone at frequency $f = |h_1 BPF_1 + h_2 BPF_2|$, for $h_1, h_2 \in \{\dots, -2, -1, 1, 2, \dots\}$, is computed as:

$$A_p(\varrho, \varphi, f) = 2\left|P_{h_1,h_2}(\varrho, \varphi)\right|. \tag{4.12}$$

In Eq. (4.11), $M_0 = v_0/a_0$ is the Mach number of the freestream axial flow relative to the rotor in forward flight, while $M_{adv,2} = V_{adv,2}/a_0$ is the blade section Mach number. The argument of the Bessel function $\mathcal{J}_{h_2B_2-h_1B_1}$ is:

$$q = \frac{\left(h_2B_2 - h_1B_1\frac{|\Omega_1|}{|\Omega_2|}\right)\frac{R}{R_{T,2}}M_{T,2}\sin\varphi}{1 - M_0\cos\varphi}. \tag{4.13}$$

Terms ϕ_s and ϕ_l are introduced in Eq. (4.11) to take into account the phase shift due to the blade sweep and lean. They depend on the midchord alignment (MCA), i.e., the local sweep, and the face alignment (FA), i.e., the local lean, respectively (see Figure 4.5 b)). Terms k_γ and k_ξ are wavenumbers (for more details see Appendix C).

The IN component provided by Eq. (4.11) arises from the unsteady loading induced on the rear rotor by the harmonic of order h_1 of the velocity perturbation generated by the front rotor

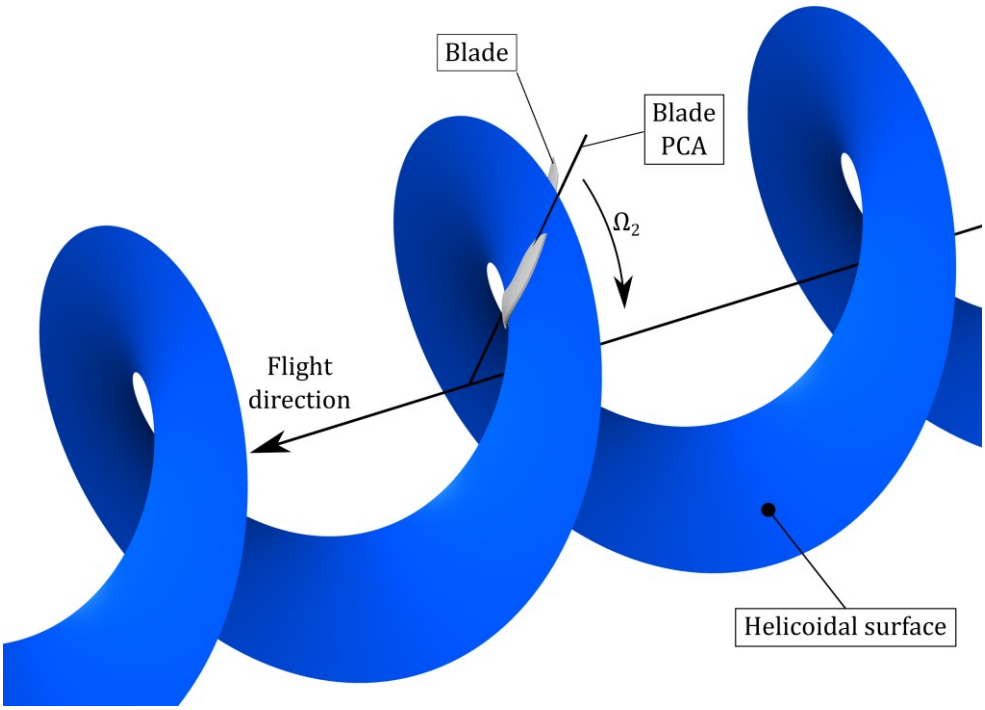

Figure 4.4 – Helicoidal surface swept out by the PCA of the blade in forward motion and rotating with angular speed Ω_2

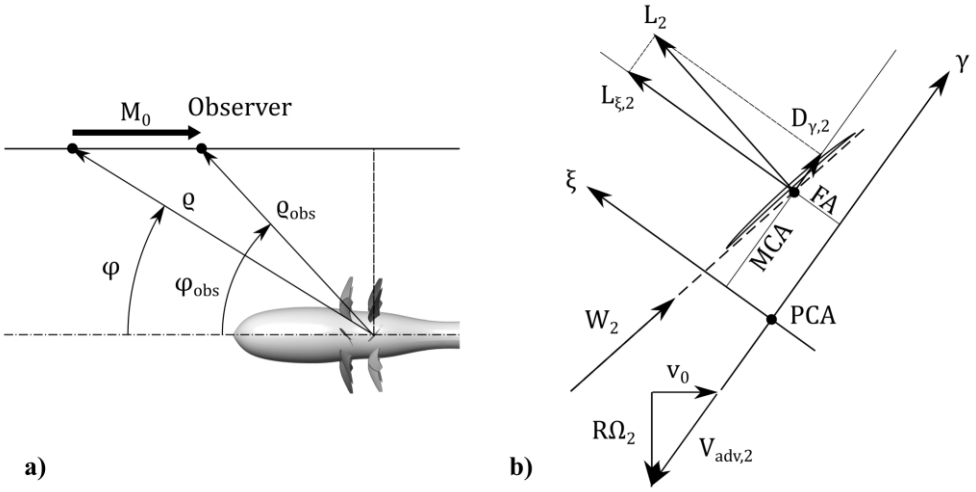

Figure 4.5 – Reference frames for the noise propagation model.
a) emission coordinates (ρ, φ) and observer coordinates $(\rho_{obs}, \varphi_{obs})$,
b) blade section helicoidal coordinates (γ, ξ) and blade load.

(see Eq. (4.6)). Complex parameters C_{Dh_1} and C_{Lh_1} represent amplitude and phase of the unsteady drag and lift coefficients, respectively, due to this flow perturbation. In the present noise propagation model, drag and lift are intended as the forces in the directions γ and ξ, respectively [38,39]. Therefore, the Fourier coefficients of the lift force per unit span, $L_2(h_1)$, given by the blade response model are projected onto axes ξ and γ of the helicoidal coordinate system, obtaining the $L_{\xi,2}(h_1)$ and $D_{\gamma,2}(h_1)$ components of the unsteady loads, as shown in Figure 4.5 b). Note that $L_{\xi,2}$ and $D_{\gamma,2}$ are not the lift and drag in a strict sense (they are not normal and parallel to $\boldsymbol{W}_2$, respectively), but they actually represent the components of L_2, which is the lift force given by the blade response model. The lift and drag coefficients are calculated by means of the following equations:

$$C_{Lh_1} = \frac{L_{\xi,2}(h_1)}{\frac{1}{2}\rho_0 V_{adv,2}^2} \tag{4.14}$$

and

$$C_{Dh_1} = \frac{D_{\gamma,2}(h_1)}{\frac{1}{2}\rho_0 V_{adv,2}^2}. \tag{4.15}$$

Note that this approach yields the same phase for C_{Lh_1} and C_{Dh_1}, that is, $\angle\{C_{Lh_1}\} = \angle\{C_{Dh_1}\} = \angle\{L_2(h_1)\}$. Indeed, coefficients C_{Lh_1} and C_{Dh_1} computed from the pressure distribution extracted from URANS show that the lift and drag harmonics have almost the same phase. Moreover, the mean angle between $\boldsymbol{W}_2$ and $\boldsymbol{V}_{adv,2}$ along the blade span is about 7.9°, resulting in a preferential projection of $L_2(h_1)$ along ξ, and indicating that C_{Lh_1} contributes mostly to the computed noise emission. Consequently, the fact that C_{Lh_1} and C_{Dh_1} have the same phase should not affect significantly the noise estimation.

Complex coefficients $\Psi_{Dh_1}(k_\gamma)$ and $\Psi_{Lh_1}(k_\gamma)$ in Eq. (4.11) are dimensionless non-compactness factors that are used to take into account the actual distribution of the loading sources along the chord of the blade sections [39]. These coefficients are computed under the assumption that the source distributions are real functions of the chordwise coordinate γ (see Appendix C). Therefore, in the present implementation, the distributions of the steady lift and drag sources, extracted from the RANS blade pressure, were used for all harmonic orders h_1.

Due to the convective effects perceived in a reference frame attached to the aircraft, the signal calculated at (ϱ, φ) is detected by an observer located at the coordinates $(\varrho_{obs}, \varphi_{obs})$, as shown in Figure 4.5 a), Therefore, the convective effects (equivalent to the retarded aircraft position perceived by a fixed observer) are taken into account by assigning the acoustic pressure computed at point (ϱ, φ) to observer location $(\varrho_{obs}, \varphi_{obs})$, the relationship between these two points being

$$\begin{cases} \cos\varphi = M_0 \sin^2\varphi_{obs} + \cos\varphi_{obs}\sqrt{1 - M_0^2 \sin^2\varphi_{obs}} \\ \varrho = \varrho_{obs}\dfrac{\sin\varphi_{obs}}{\sin\varphi} \end{cases}. \tag{4.16}$$

5 TIP VORTEX MODEL

This chapter presents a novel model of the FR tip vortices developed to account for the contribution of these important three-dimensional flow structures to the CROR interaction noise. The introduction of an appropriate TV model leads to a more realistic description of the flow perturbations released by the front rotor and allows a more accurate extrapolation of these perturbations beyond the mixing plane. In fact, the velocity perturbations due to the FR tip vortices are misinterpreted by the 2D extrapolation model [42,55], leading to a poor extrapolation to the outward radii of the rear rotor, and hence to an inaccurate prediction of the interaction noise.

The present semi-analytical TV model is calibrated using data extracted from RANS solutions and allows accounting for the influence of the FR tip vortices on the velocity perturbations reconstructed along the entire span of the rear rotor blades. Therefore, an improved RANS-informed extrapolation model is obtained for the fast prediction of CROR noise.

5.1 General description of the tip vortex model

Accepting the assumption of linearity, the velocity field past a CROR can be thought as the superposition of the free stream velocity $\boldsymbol{v}_0$, velocity perturbations $\boldsymbol{v}_{TV}$ generated by the front rotor TVs, and perturbations $\boldsymbol{v}_e$ generated by sources other than front rotor TVs (viscous wakes, rotor bound potential field, rear rotor TVs, etc.). Considering also the splitting into azimuthal average $\overline{\boldsymbol{v}}$ and azimuthal perturbations $\boldsymbol{v}'$, the absolute velocity field can be expressed as:

$$\boldsymbol{v} = \boldsymbol{v}_0 + \boldsymbol{v}_{TV} + \boldsymbol{v}_e = \overline{\boldsymbol{v}} + \boldsymbol{v}' = \overline{\boldsymbol{v}}_0 + \overline{\boldsymbol{v}}_{TV} + \overline{\boldsymbol{v}}_e + \boldsymbol{v}'_{TV} + \boldsymbol{v}'_e. \tag{5.1}$$

Note that $\boldsymbol{v}'_0 = 0$ ($\boldsymbol{v}_0 = \overline{\boldsymbol{v}}_0$), since we consider a uniform freestream, aligned with the CROR rotation axis. It is further assumed that $\boldsymbol{v}'$ can be divided into the perturbations generated by the front rotor, $\boldsymbol{v}'_{FR}$, and the rear rotor, $\boldsymbol{v}'_{RR}$:

$$\boldsymbol{v} = \overline{\boldsymbol{v}} + \boldsymbol{v}'_{FR} + \boldsymbol{v}'_{RR}. \tag{5.2}$$

The azimuthal perturbations $\boldsymbol{v'}_{FR}$ and $\boldsymbol{v'}_{RR}$, which are velocity disturbances in space, are steady in the reference frames of the FR and RR, respectively. Due to the rotation, the perturbations generated by one rotor are perceived as velocity fluctuations in time by the other rotor.

The contribution to $\boldsymbol{v'}_{FR}$ of sources other than front rotor TVs is ascribed to the viscous wakes and rotor potential field, which behave as approximately 2D flow structures. $\boldsymbol{v'}_{FR}$ can thus be expressed as:

$$\boldsymbol{v'}_{FR} = \boldsymbol{v'}_{e,FR} + \boldsymbol{v'}_{TV} = \boldsymbol{v'}_{2D} + \boldsymbol{v'}_{TV}. \tag{5.3}$$

The azimuthal perturbations $\boldsymbol{v'}_{2D}$, due to viscous wake and potential field, can be reconstructed beyond the MP by means of the 2D extrapolation model. Therefore, the objective is to extrapolate $\boldsymbol{v'}_{TV}$.

The proposed TV model is genuinely 3D and allows computing the absolute velocity field $\boldsymbol{u}_{TV}$ due to the front rotor TVs in the coordinate system (X, Y, Z) (see Figure 4.1) of the FR. Then, the azimuthal perturbations due to the TVs can be computed in the cylindrical coordinate system as $\boldsymbol{u'}_{TV}(X, R, \Psi) = \boldsymbol{u}_{TV}(X, R, \Psi) - \overline{\boldsymbol{u}}_{TV}(X, R)$.

To compute the model velocity $\boldsymbol{u}_{TV}$ at any point (X, Y, Z) the trajectory of the tip vortices must be defined. The trajectory of the TV centre is modelled by a helix which extends from the FR trailing edge to infinity downstream. The helix has variable radius and pitch in order to account for the effect of stream-tube contraction and flow acceleration. The 3D curve representing the helix is defined in the relative reference frame (X, Y, Z) and its unknown parameters are calibrated by fitting the TV trajectory extracted from the RANS solution.

After defining the TV trajectory, the velocity induced by the vortices, $\boldsymbol{u}_{ind}$, is computed numerically by means of the Biot-Savart law, modified to take into account the effect of a viscous core with finite radial extent [47]. Moreover, the tip vortices emitted by CROR blades are characterized by a wake-like velocity deficit locally tangent to the TV trajectory [18,46]. The contribution of this deficit, $\boldsymbol{u}_{def}$, to the velocity field is also modelled and is added to the induced velocity:

$$\boldsymbol{u}_{TV} = \boldsymbol{u}_{ind} + \boldsymbol{u}_{def}. \tag{5.4}$$

The parameters of the TV model to be calibrated with data extracted from RANS are the vortex circulation, Γ, the viscous core radius, r_c, and the peak of the velocity deficit, $V_{x,def}$.

In principle, the parameters of the modelled 2D perturbations, $\boldsymbol{u'}$, and TV flow field, $\boldsymbol{u}_{TV}$, should be balanced by fitting the azimuthal perturbations $\boldsymbol{v'}_{FR} = \boldsymbol{v'}_{2D} + \boldsymbol{v'}_{TV}$ extracted from the

RANS solution with the superposition $\boldsymbol{u}' + \boldsymbol{u}'_{TV}$. However, this calibration procedure is prohibitive for two reasons:

- $\boldsymbol{u}_{TV}$ is evaluated numerically. Therefore, $\boldsymbol{u}'_{TV}$ does not have an analytical form.
- Due to the three-dimensionality of the TV model, a cumulative calibration of $\boldsymbol{u}'$ and $\boldsymbol{u}_{TV}$ would involve the simultaneous identification of the 2D model parameters for all the averaged streamlines. Consequently, the number of parameters to be balanced would be very large, leading to an unsustainable increase in the computational time required for the solution of the least squares problem.

This issue can be overcome by singling out the contribution of the tip vortex from the RANS flow field in order to calibrate the parameters of the TV model separately. After the calibration, the velocity field $\boldsymbol{u}_{TV}$, and hence the perturbations in space $\boldsymbol{u}'_{TV}$, can be computed at any point (X, Y, Z). Then, $\boldsymbol{u}'_{TV}$ can be used to perform the following steps:

1) $\boldsymbol{u}'_{TV}$ is subtracted from the RANS velocity perturbations in the region between the FR trailing edge and the MP. The influence of the TVs is thus removed in the calibration region of the 2D flow model, and the identification of the parameters of $\boldsymbol{u}'$ can be performed separately.
2) The azimuthal perturbations $\boldsymbol{u}'_{TV}$ are computed beyond the MP, at the LE of the rear rotor, where they are added to $\boldsymbol{u}'$, extrapolated by means of the 2D flow model. This allows reconstructing the flow unsteadiness at the rear blades accounting for the contributions of FR viscous wakes, potential field, and tip vortices.

However, identifying the contribution of a single TV to the RANS velocity field is a very difficult task, since the velocity is influenced by different flow structures (viscous wakes, potential field, tip vortices released by the other blades).

On the other hand, singling out the TV contribution to the overall flow field can be considerably simplified by exploiting the vorticity. Most vorticity is generated at the blade surface and is convected downstream, giving rise to the rotor wakes. Anyhow, it is possible to identify a limited region around the vortex trajectory where the vorticity can essentially be ascribed to the TV, thus excluding the contribution of the blade viscous wakes.

Consider the local reference frame (x, y, z) of the tip vortex and depicted in Figure 5.1. The x axis is locally tangent to the vortex trajectory and the y axis lies in the plane defined by the x axis and radial direction R. The corresponding cylindrical coordinate system (x, r, ϑ) is also shown in Figure 5.1. Figure 5.2 shows contours of the absolute vorticity components $(\omega_x, \omega_r, \omega_\vartheta)$

extracted from the RANS solution in a polar grid locally normal to the TV centre trajectory, i.e., to the local x direction. The grid is centred on the vortex trajectory and its location and orientation are indicated by the blue disc in Figure 5.3. After interpolating the vorticity on the local grid, the local components $(\omega_x, \omega_y, \omega_z)$ are computed and their counterparts in the cylindrical coordinate system $(\omega_x, \omega_r, \omega_\vartheta)$ are obtained. The vorticity contours in Figure 5.2 clearly show the trace of the viscous wake in the region $y < 0$ (radially inward with respect to the tip vortex centre). This trace extends up to the centre of the circular domain where a small circular region of high ω_x clearly identifies the viscous core of the tip vortex. Since its inception at the TE of the front blade, the tip vortex quickly rolls up [56,57] generating an almost axisymmetric distribution of ω_x and ω_ϑ around the vortex centre. Due to the rollup process, the centre of the TV moves away from the vorticity sheet ascribed to the viscous wake released by the FR blade. When the TV is completely developed, the vorticity sheet of the blade wake lies entirely in the half plane $z < 0$. In view of this, it is assumed that the vorticity contained in the region $z > 0$ (enclosed by a dashed line in Figures 5.2 a) and b)) can be ascribed solely to the tip vortex.

A novel procedure based on the fitting of the vorticity in the region $z > 0$ is proposed to single out the contribution of the TV. To do so, a model describing the axisymmetric vorticity

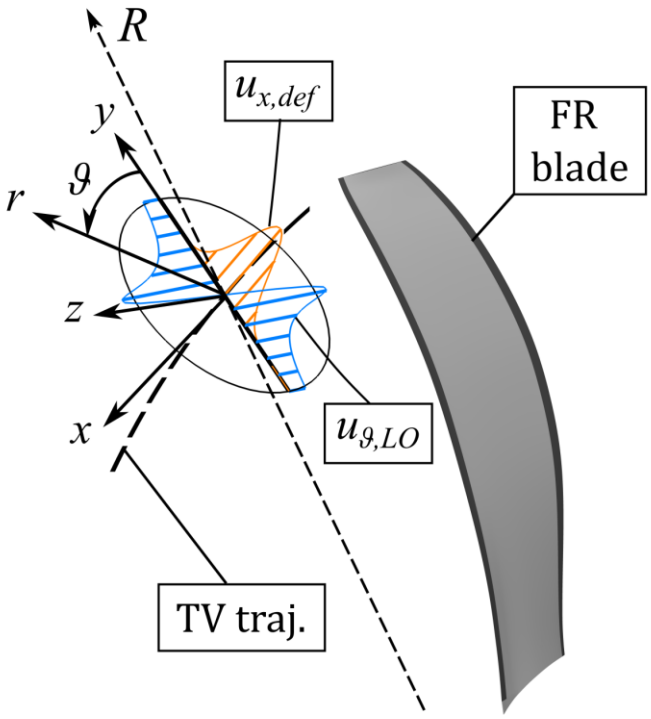

Figure 5.1 – Local reference frame of the tip vortex.

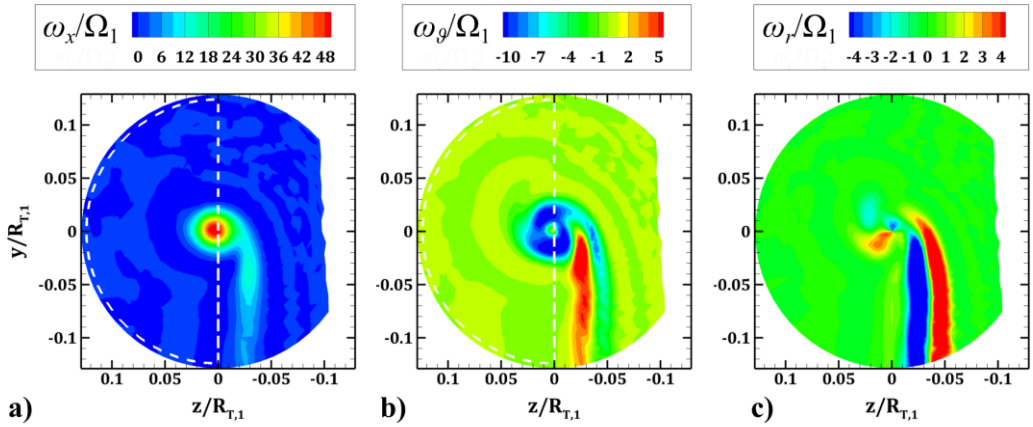

Figure 5.2 – Contours of absolute vorticity components in the local reference frame of the TV, extracted from the RANS solution in the region between the FR trailing edge and the MP.

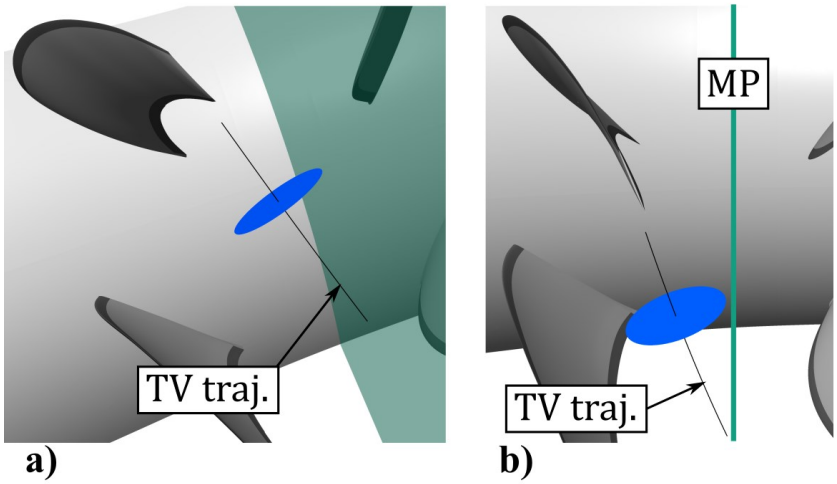

Figure 5.3 – Orientation of a grid for the vorticity extraction.
a) 3D view. **b)** projection onto (X, Y) plane.

distribution around the TV centre has been developed by enforcing local velocity distributions of the induced velocity, $\boldsymbol{u}_{ind}$, and velocity deficit, $\boldsymbol{u}_{def}$.

Quaglia et al. [46] showed that locally the TV tangential (swirl) velocity is well represented by the Lamb-Oseen vortex distribution:

$$u_{\vartheta,LO}(r) = \frac{\Gamma}{2\pi r}\left[1 - e^{-\alpha^2\left(\frac{r}{r_c}\right)^2}\right], \tag{5.5}$$

where r_c denotes the viscous core radius and $\alpha^2 = 1.25643$ ensures that the maximum swirl velocity is located at $r = r_c$. Therefore, it is assumed that $\boldsymbol{u}_{ind}$ can be approximated by Eq. (5.5)

in the region around the TV trajectory (see the blue velocity profile in Figure 5.1). Moreover, Delattre and Falissard [18] and Quaglia et al. [46] showed that the wake-like velocity deficit, $\boldsymbol{u}_{def}$, locally aligned with the x direction, is well approximated by an axisymmetric gaussian distribution (see the orange velocity profile in Figure 5.1):

$$u_{x,def}(r) = \left[-V_{x,def} e^{-\left(\frac{r}{r_c}\right)^2}\right], \tag{5.6}$$

where $V_{x,def} > 0$ identifies the velocity peak at the vortex centre.

Assuming that the local velocity components u_ϑ and u_x are given by Eqs. (5.5) and (5.6), respectively, while $u_r = 0$, and that the rate of change of the velocity along the vortex trajectory is small (i.e., $\partial/\partial x \ll \partial/\partial r$), the TV absolute vorticity in a cylindrical coordinate system locally aligned with the TV helix can be expressed as:

$$\begin{aligned}\boldsymbol{\omega} = \nabla \times \boldsymbol{u} = \frac{1}{r}\frac{\partial(r u_\vartheta)}{\partial r}\boldsymbol{e}_x - \frac{\partial u_\vartheta}{\partial x}\boldsymbol{e}_r - \frac{\partial u_x}{\partial r}\boldsymbol{e}_\vartheta \approx \\ \approx \left[\frac{\Gamma\alpha^2}{\pi {r_c}^2} e^{-\alpha^2\left(\frac{r}{r_c}\right)^2}\right]\boldsymbol{e}_x + \left[-\frac{2r}{{r_c}^2} V_{x,def} e^{-\left(\frac{r}{r_c}\right)^2}\right]\boldsymbol{e}_\vartheta ,\end{aligned} \tag{5.7}$$

where $(\boldsymbol{e}_x, \boldsymbol{e}_r, \boldsymbol{e}_\vartheta)$ are the unit vectors of the local coordinate system. The contribution of a single TV can be singled out by fitting Eq. (5.7) with the vorticity extracted from the RANS solution in the local region $z > 0$ in order to calibrate the unknown parameters of the TV model, that is Γ, r_c and $V_{x,def}$.

In what follows, a detailed description of the TV trajectory and velocity field models is given. Then, the calibration procedure is reported, and preliminary results are provided for the velocity field, $\boldsymbol{u}_{TV}$, ascribed to the tip vortices. Finally, the procedure for merging the TV and 2D flow perturbations is described.

5.2 Vortex path model

A TV released by the front rotor undergoes an increase in the axial transport velocity due to the acceleration produced by both rotors and to the influence of the adjacent TVs (see Landgrebe [58] for a comprehensive study on the latter effect for helicopter rotors in hover conditions). Therefore, a radial contraction and a variable pitch of the TV helix must be considered for an appropriate modelling of the TV path, and hence of the TV velocity field. The wake generated by

the FR is divided into a near wake region and an ultimate wake region (see Figure 5.4). The former lies between the FR trailing edge and axial coordinate X_{uw}, and is characterized by a radial contraction and a variable pitch of the TV helix. The ultimate wake extends from X_{uw} to infinity downstream and has constant radius and pitch.

To compute radius R_∞ and pitch angle β_∞ of the ultimate wake region, the stream-tube contraction and the flow acceleration must be determined. For this purpose, the front and rear rotors are reduced to a single actuator disc, as shown in Figure 5.5. By assuming that the flow is incompressible and no residual swirl is present in the wake, the following equation can be derived from the actuator disc theory:

$$T = \rho_0 A(v_0 + w)2w \Longrightarrow w = \frac{-v_0 + \sqrt{{v_0}^2 + 4\frac{T}{2\rho_0 A}}}{2}. \tag{5.8}$$

Knowing the freestream conditions, the total thrust $T = T_1 + T_2$, and the disc area $A = \pi {R_{T,1}}^2$, the velocity w induced at the disc can be calculated. Then, area A_∞ of the contracted stream-tube at infinity can be computed by applying the mass conservation

$$\dot{m} = \rho_0 A(v_0 + w) = \rho_0 A_\infty (v_0 + 2w) \Longrightarrow A_\infty = \frac{A(v_0 + w)}{(v_0 + 2w)}, \tag{5.9}$$

and the radius of the TV helix in the ultimate wake region is given by $R_\infty = \sqrt{A_\infty/\pi}$. Since no residual swirl is assumed in the wake, the pitch angle of the helix can be computed as

$$\beta_\infty = \tan^{-1}\frac{\Omega_1 R_\infty}{(v_0 + 2w)}, \tag{5.10}$$

where Ω_1 is the angular velocity of the front rotor. The analytical TV path in the ultimate wake is therefore described in cartesian coordinates by

$$\begin{cases} Y(X) = R_\infty \cos\left(b_\infty X + \Psi_{i,\infty}\right) \\ Z(X) = R_\infty \sin\left(b_\infty X + \Psi_{i,\infty}\right) \end{cases}, \tag{5.11}$$

with $b_\infty = \tan(\beta_\infty)/R_\infty = \Omega_1/(v_0 + 2w)$.

The general form of the TV helix in the near wake is given by

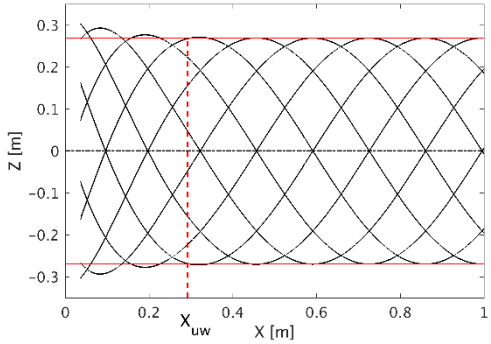

Figure 5.4 – Near wake and ultimate wake of the FR tip vortex.

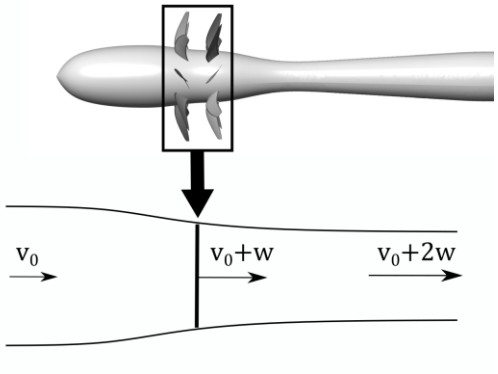

Figure 5.5 – Actuator disc model.

$$\begin{cases} Y(X) = R(X)\cos[\Psi(X)] \\ Z(X) = R(X)\sin[\Psi(X)] \end{cases}, \tag{5.12}$$

and the following exponential laws for the radial and azimuthal coordinates are assumed:

$$\begin{cases} R(X) = R_\infty + K_{r1}e^{-K_{r2}X} \\ \Psi(X) = \Psi_i + K_{\Psi 1}[1 - e^{-K_{\Psi 2}X}] \end{cases}, \tag{5.13}$$

with parameters K_{r1}, K_{r2}, $K_{\Psi 1}$, $K_{\Psi 2} > 0$. $R(X)$ represents the radial contraction of the TV, while $\Psi(X)$ accounts for the increasing rate of the axial displacement due to the flow acceleration. The exponential laws in Eq. (5.13) are proposed since they allow obtaining a smooth transition of the TV trajectory from near to ultimate wakes. Curve $R(X)$ approaches asymptotically R_∞, and, strictly speaking, the initial coordinate of the ultimate wake, X_{uw}, should be located at infinity. However, X_{uw} is assumed to be the axial coordinate where $R(X) = 1.01 \cdot R_\infty$, and it is computed according to the equation:

$$X_{uw} = -\frac{1}{K_{r2}} \ln\left(\frac{0.01 \cdot R_\infty}{K_{r1}}\right). \tag{5.14}$$

Thus, curve $R(X)$ is used for both near and ultimate wakes. Recent experimental investigations show that the TV radial contraction is almost linear in the region between the FR trailing edge and the RR leading edge [59]. Therefore, a piecewise function $R(X)$, consisting of two straight lines smoothly connected by a curve, could be suitable for a good representation of the TV path. However, the exponential laws in Eq. (5.13) makes the algorithm more robust, because it avoids the introduction of an arbitrary curve to connect the near and ultimate wakes.

A smooth helix at the interface $X = X_{uw}$ is obtained by imposing $d\Psi(X_{uw})/dX = b_\infty$, which leads to the equation $K_{\Psi 1} = b_\infty / K_{\Psi 2} e^{-K_{\Psi 2} X_{uw}}$. When using this relationship to eliminate $K_{\Psi 1}$ from Eq. (5.13), only $K_\Psi = K_{\Psi,2}$ remains as an unknown parameter. To summarize, the analytical TV path in polar coordinates is defined as follows:

- $R(X) = R_\infty + K_{r1} e^{-K_{r2} X}$ for both near and ultimate wake regions, (5.15)
- $\Psi(X) = \Psi_i + \frac{b_\infty}{K_\Psi e^{-K_\Psi X_{uw}}} [1 - e^{-K_\Psi X}]$ for $X \leq X_{uw}$ (near wake), (5.16)
- $\Psi(X) = \Psi_{i,\infty} + b_\infty X$ for $X > X_{uw}$ (ultimate wake). (5.17)

The parameters to be calibrated using the RANS solution are K_{r1}, K_{r2}, Ψ_i, and K_Ψ, while $\Psi_{i,\infty} = \Psi(X_{uw}) - b_\infty X_{uw}$ can be calculated directly.

5.3 Velocity field model

Consider the helix representing the TV released by the k-th blade of the FR, where k = 1 ... B_1. The helix is treated as a vortex filament that generates an induced velocity field, $\boldsymbol{u}_{ind,k}$. Then, the helix is discretized into small straight-line vortex segments and the induced velocity at a given point is evaluated numerically by means of the Biot-Savart law [47,60] applied to each segment. Referring to Figure 5.6, the contribution $\Delta \boldsymbol{u}_{ind}$ at point C due to the segment AB having constant circulation Γ is computed as [61]:

$$\Delta \boldsymbol{u}_{ind} = K_v \frac{\Gamma}{4\pi} \frac{(r_A + r_B)(\boldsymbol{r}_A \times \boldsymbol{r}_B)}{r_A r_B (r_A r_B + \boldsymbol{r}_A \cdot \boldsymbol{r}_B)}. \tag{5.18}$$

The correction factor K_v has been introduced to account for the viscous core of finite size typical of tip vortices [47], thus avoiding the singular behaviour of the Biot-Savart law as point C approaches the vortex filament. It is assumed that the local TV swirl velocity is well represented by the Lamb-Oseen vortex distribution, Eq. (5.5), which leads to the following form of the correction factor:

$$K_v = 1 - e^{-\alpha^2\left(\frac{h}{r_c}\right)^2}, \tag{5.19}$$

where h is the distance of point C from vortex segment AB (see Figure 5.6).

According to Eq. (5.6), the velocity deficit ascribed to the TV released by the k-th blade of the FR is modelled by the axisymmetric gaussian

$$\boldsymbol{u}_{def,k}(r) = \left[-V_{x,def}\, e^{-\left(\frac{r}{r_c}\right)^2}\right]\boldsymbol{e}_x, \tag{5.20}$$

where $\boldsymbol{e}_x$ is the unit vector tangent to the TV helix and pointing in the direction of the vortex convection. The magnitude of this velocity deficit can be considerable and its impact on the flow perturbations at the LE of the rear blades should be taken into account for a correct estimation of the interaction noise tones [18,46].

To compute $\boldsymbol{u}_{def,k}$ at a point (X, Y, Z), the corresponding coordinates (X_C, Y_C, Z_C) of the analytical TV helix are determined numerically so that the line connecting the two points is perpendicular to $\boldsymbol{e}_x(X_C, Y_C, Z_C)$. The local radius is $r = [(X - X_C)^2 + (Y - Y_C)^2 + (Z - Z_C)^2]^{1/2}$ and $\boldsymbol{e}_x(X_C, Y_C, Z_C)$ gives the opposite direction of $\boldsymbol{u}_{def,k}(X, Y, Z)$. The example in Figure 5.7 shows the direction of $\boldsymbol{u}_{def,k}$ (red arrows), associated with the TV emitted by one of the FR blades (black dashed line) and computed along a circular arc (black continuous line). It is observed that both the direction of $\boldsymbol{u}_{def,k}$ and the radius (blue lines) vary along the circular arc.

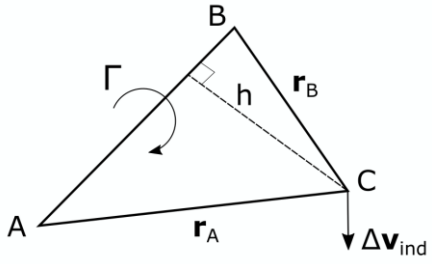

Figure 5.6 – Velocity induced at point C by a straight-line vortex segment AB.

Since its inception at the TE of the FR blade, the TV exhibits a viscous diffusion of the vorticity contained in the vortex core, which results in an increase in the core radius and a decrease in the maximum swirl velocity and velocity deficit. The Lamb-Oseen vortex model is capable of accounting for the effect of the vorticity diffusion by introducing an appropriate dependence of core radius r_c on time, that is, on the downstream position of the TV. Since r_c is directly related to the standard deviation of the gaussian function describing $\boldsymbol{u}_{def,k}$ (see Equation (5.20)), the spreading of the velocity deficit can also be considered. Therefore, the effect of the vorticity diffusion is included in the present TV model by introducing the equations suggested by Quaglia et al. [46] for the distributions of r_c and $V_{x,def}$ along the TV helix:

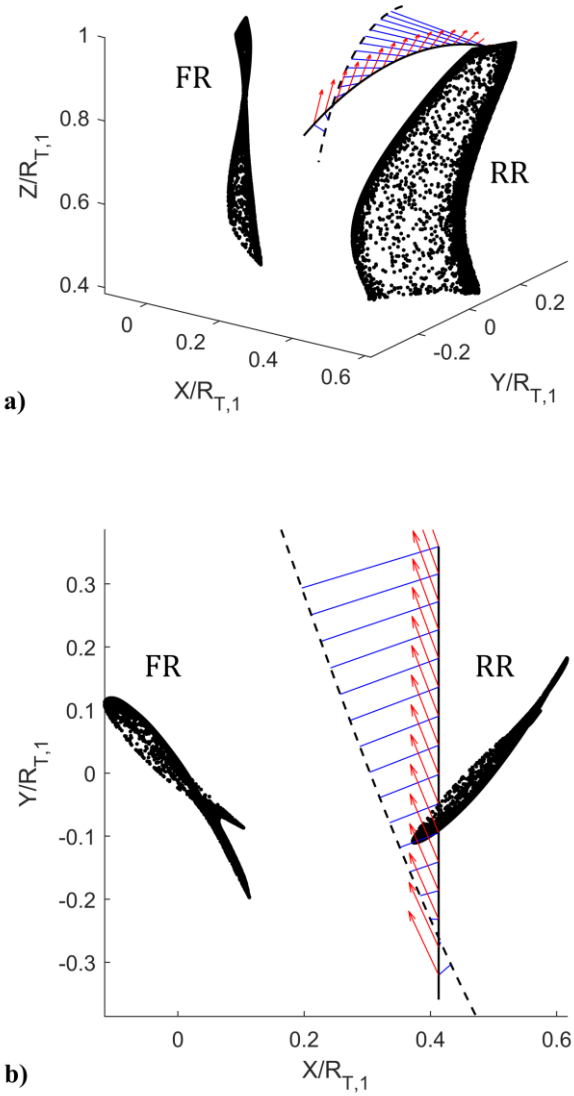

Figure 5.7 – Direction of the velocity deficit (red arrows) along a circular arc.
a) 3D view, **b)** projection onto (X, Y) plane.

$$r_c{}^2(X) = r_I{}^2 + r_X{}^2 X\,, \tag{5.21}$$

$$V_{x,def}(X) = V_I + \frac{V_X}{\sqrt{X}}. \tag{5.22}$$

Another effect considered in this study is the variation of the circulation Γ that may occur due to the quick rollup of the TV in its early development stage [47] and to the resulting ingestion of vorticity in the viscous core. An empirical law is proposed to model the circulation along the helix:

$$\Gamma(X) = \Gamma_I + K_{\Gamma 1}\left[1 - e^{-K_{\Gamma 2}(X - X_{TE})}\right], \tag{5.23}$$

where $\Gamma_I > 0$, $K_{\Gamma 1}$, $K_{\Gamma 2} \geq 0$ and X_{TE} is the axial coordinate of the helix at the blade TE. It should be noted that $\Gamma(X)$ increases monotonically and tends asymptotically to the maximum value $\Gamma_\infty = \Gamma_I + K_{\Gamma 1}$. Therefore, the dissipation due to viscosity, which would lead to a decrease in the circulation moving downstream along the helix, is neglected.

According to the proposed model, the velocity field generated by a single TV can be computed after calibrating the parameters r_I, r_X, V_I, V_X, Γ_I, $K_{\Gamma 1}$, and $K_{\Gamma 2}$.

Finally, the velocity field, $\boldsymbol{u}_{TV}$, due to the tip vortices released by all the blades of the front rotor is evaluated by superimposing the contributions of all vortices

$$\boldsymbol{u}_{TV} = \sum_{k=1}^{B_1} \left(\boldsymbol{u}_{ind,k} + \boldsymbol{u}_{def,k}\right) = \boldsymbol{u}_{ind} + \boldsymbol{u}_{def}\,, \tag{5.24}$$

where B_1 is the number of FR blades. The contribution of the tip vortex released by the k-th blade is calculated by positioning the associated vortex helix at the proper azimuthal coordinates.

5.4 Calibration of the tip vortex model

The first step to determine $\boldsymbol{u}_{TV}$ is the calibration of the analytical path of the TV centre. Subsequently, the parameters of the velocity model are balanced using the absolute vorticity extracted from the RANS solution and represented in the reference frame locally aligned with the TV path.

5.4.1 Vortex path parameters

In order to calibrate the unknown parameters of the TV helix (K_{r1}, K_{r2}, Ψ_i, and K_Ψ) the coordinates of the TV centre are extracted from the RANS solution by detecting the points of maximum helicity [62] at several axial locations between the front rotor TE and the MP. The green circles in Figure 5.8 indicate the extracted (X, R) and (X, Ψ) coordinates of such points. In the figure, the linear coordinates are normalized by the FR tip radius, while the azimuthal coordinate is normalized by the angular interval of one FR blade passage. First, the radial coordinates are fitted by Eq. (5.15), and the ultimate wake initial coordinate X_{uw} is computed by means of Eq. (5.14). Then, the azimuthal coordinates are fitted by Eq. (5.16), which describes the helix in the near wake region. Finally, $\Psi_{i,\infty} = \Psi(X_{uw}) - b_\infty X_{uw}$ is computed to define completely the TV helix. The black solid lines in Figure 5.8 represent the analytical fitting of the centre path, which is in good agreement with the data extracted from the RANS solution. It should be noted that X_{uw} lies downstream of the rear rotor, as shown in Figure 5.9. This result is physically consistent since the rear rotor is loaded and the stream-tube contraction cannot end in the region between FR and RR.

The values of the parameters of the TV helix obtained for the present test case are reported in Table 5.1. The parameters that depend on the rotor dimension, i.e., R_∞, X_{uw}, K_{r1}, K_{r2}, and K_Ψ, are normalized by the FR tip radius. Note that the values of the initial azimuthal coordinates, Ψ_i and $\Psi_{i,\infty}$ (see Eqs. (5.16) and (5.17)), given in the table refer to the trajectory of the TV released by the reference blade of the FR, that is, the blade having the PCA aligned with the axis Z. To calculate the trajectory of the vortices generated by the other front blades, the initial azimuthal coordinates must be shifted by $\Delta\Psi_k = \mathrm{k}(2\pi/B_1)$, where $\mathrm{k} = 1 \ldots (B_1 - 1)$.

The coordinates of the analytical TV helix extrapolated beyond the MP, up to the leading edge of the RR, are represented by the black dashed lines in Figure 5.8. A comparison is made with the TV centre trajectory extracted from URANS data and represented by the red bands in Figure 5.8.

Table 5.1 – Parameters of the analytical TV path.

Computed parameters			
$R_\infty/R_{T,1}$	$X_{uw}/R_{T,1}$	b_∞ $\left[\frac{\mathrm{rad}}{\mathrm{m}}\right]$	$\Psi_{i,\infty}$ [rad]
0.8663	0.9784	5.8275	2.0959
Calibrated parameters			
$K_{r1}/R_{T,1}$	$K_{r2} \cdot R_{T,1}$	Ψ_i [rad]	$K_\Psi \cdot R_{T,1}$
0.1961	3.1882	1.4388	0.6137

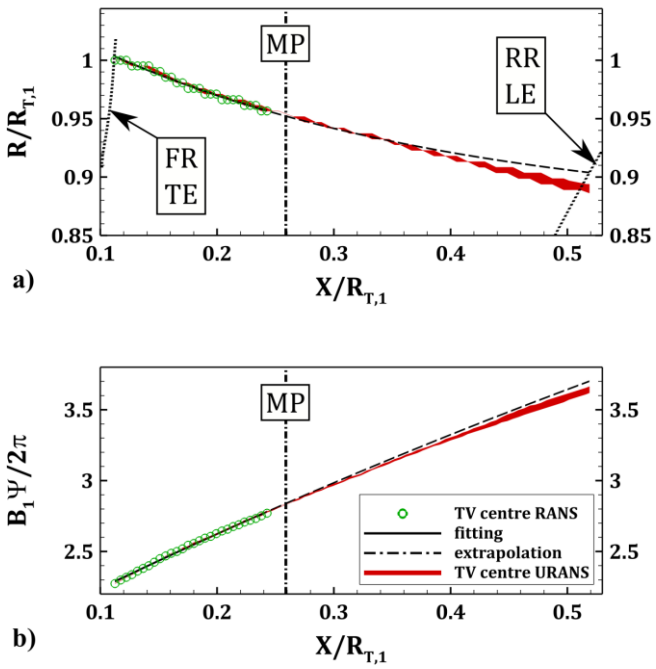

Figure 5.8 – Coordinates of the tip vortex centres extracted from RANS and URANS solutions, and analytical centre path (fitted upstream of the MP and extrapolated downstream). **a)** normalized (X, R) coordinates. **b)** normalized (X, Ψ) coordinates.

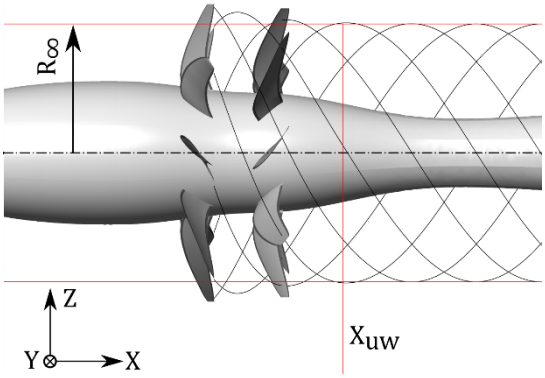

Figure 5.9 – Position of the interface between near wake and ultimate wake resulting from the model calibration.

These bands indicate the radial and azimuthal ranges spanned by the TV centre during the blade rotation and are obtained by extracting the centre coordinates at six blade angular positions, equally spaced over one mutual blade passage. It is observed that the location of the impingement on the RR leading edge is well predicted, with a difference $\Delta R/R_{T,1} \approx 0.013$ in the radial coordinate and $\Delta\Psi/(2\pi/B_1) \approx 0.07$ in the azimuthal coordinate. The coordinates extracted from the URANS solution show that the TV trajectory contracts radially when moving downstream with a higher rate than the fitted exponential law (Figure 5.8 a)), resulting in a slight error in the

radius extrapolation. Looking at the azimuthal coordinates (Figure 5.8 b)), a variation in the helix pitch at increasing X is clearly visible in the URANS data, which supports the assumption of variable pitch angle in the near wake region.

It is noted that the trajectory extracted from URANS lies within a very limited spatial range during the blade rotation. This can be interpreted as an indication that the circumferential perturbations due to the RR do not influence significantly the trajectory of the front rotor TVs and, presumably, the geometry of the perturbations generated by the FR during the blade rotation.

5.4.2 Velocity field parameters

To balance the velocity parameters by fitting Eq. (5.7), the RANS vorticity field is projected onto the TV local reference frame (x, r, ϑ), which can be defined after calibrating the vortex path parameters. Once the analytical representation of the TV helix has been obtained, the unit vector $\boldsymbol{e}_x$, locally tangent to the helix, is computed in the region between the FR trailing edge and the MP by means of the following equation:

$$\boldsymbol{e}_x(X) = \frac{\boldsymbol{\tau}(X)}{|\boldsymbol{\tau}(X)|} = \frac{\tau_X(X)\boldsymbol{e}_X + \tau_Y(X)\boldsymbol{e}_Y + \tau_Z(X)\boldsymbol{e}_Z}{|\boldsymbol{\tau}(X)|}, \tag{5.25}$$

The TV helix is a parametric curve in the global system of coordinates (X, Y, Z), and the components (τ_X, τ_Y, τ_Z) of a vector $\boldsymbol{\tau}$ parallel to $\boldsymbol{e}_x$ are computed as:

$$\begin{Bmatrix} \tau_X(X) \\ \tau_Y(X) \\ \tau_Z(X) \end{Bmatrix} = \begin{Bmatrix} \dfrac{\partial X_C(X)}{\partial X} \\ \dfrac{\partial Y_C(X)}{\partial X} \\ \dfrac{\partial Z_C(X)}{\partial X} \end{Bmatrix} = \tag{5.26}$$

$$= \begin{Bmatrix} 1 \\ -K_{r1}K_{r2}e^{-K_{r2}X}\cos[\Psi_i + A(1-e^{-K\Psi X})] - (R_\infty + K_{r1}e^{-K_{r2}X})\sin[\Psi_i + A(1-e^{-K\Psi X})]\,AK_\Psi e^{-K\Psi X} \\ -K_{r1}K_{r2}e^{-K_{r2}X}\sin[\Psi_i + A(1-e^{-K\Psi X})] + (R_\infty + K_{r1}e^{-K_{r2}X})\cos[\Psi_i + A(1-e^{-K\Psi X})]\,AK_\Psi e^{-K\Psi X} \end{Bmatrix},$$

where $Y_C(X)$ and $Z_C(X)$ are given by Eq. (5.12) and $A = b_\infty / K_\Psi e^{-K\Psi X_{uw}}$. Then, the local reference frame $(\boldsymbol{e}_x, \boldsymbol{e}_y, \boldsymbol{e}_z)$ is determined so that unit vector $\boldsymbol{e}_y$ (green segment in Figure 5.10) lies in the plane defined by $\boldsymbol{e}_x$ and global radial direction $\boldsymbol{e}_R$ (black line in Figure 5.10). Setting this orientation will be useful to select specific regions of the flow field for the calibration of the parameters of model (5.7).

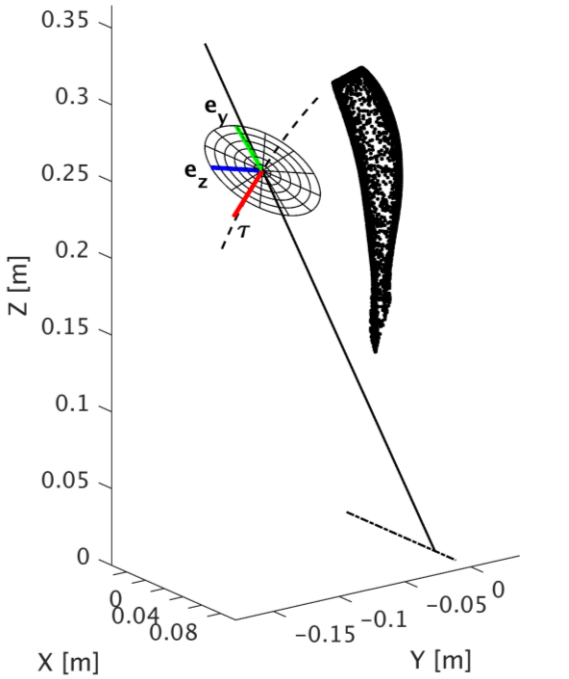

Figure 5.10 – Reference frame locally aligned with the analytical TV helix.

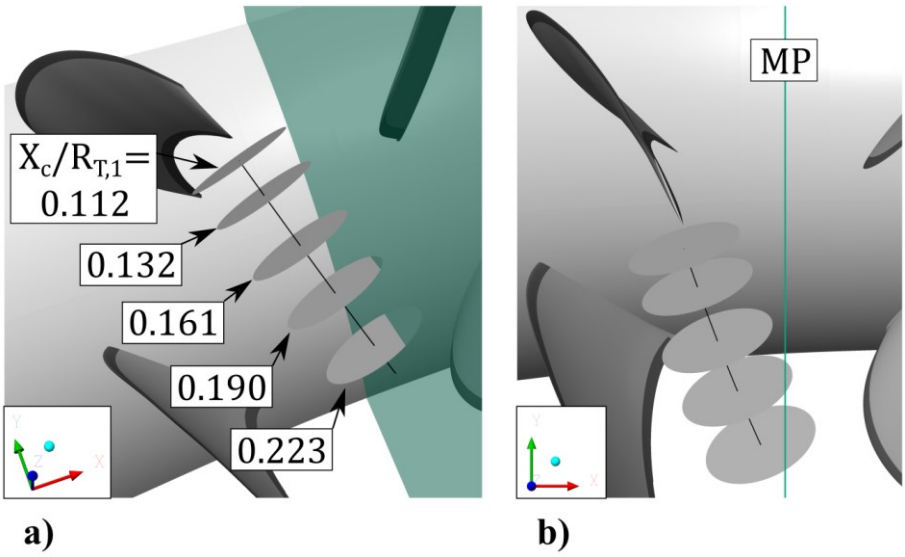

Figure 5.11 – Orientation of the grids for the vorticity extraction.
a) 3D view. **b)** projection onto $(\boldsymbol{e}_X, \boldsymbol{e}_Y)$ plane.

The RANS vorticity is interpolated on structured polar grids in plane $(\boldsymbol{e}_y, \boldsymbol{e}_z)$, centered at the helix (X_C, Y_C, Z_C), for several axial locations between the FR trailing edge and the MP. The grey discs in Figure 5.11 show the position and the orientation of some extraction grids. After interpolating the absolute vorticity on the local grids, the local components $(\omega_x, \omega_y, \omega_z)$ are

computed and their counterparts in the cylindrical coordinate system $(\omega_x, \omega_r, \omega_\vartheta)$ are finally obtained. The contours in Figure 5.12 show the vorticity, normalized using the FR angular velocity, extracted at the locations depicted in Figure 5.11 (the contours are incomplete at some locations simply because a portion of the grid lies beyond the mixing plane). The trace of the blade wake is visible in the region $y < 0$. At $X_C/R_{T,1} = 0.112$, which corresponds to the axial coordinate of the blade TE, the tip vortex is still developing (see Figure 5.12 a)) and the axisymmetric pattern of the vorticity is not well established. Moving downstream, the rollup process generates a good axisymmetric distribution of ω_x and ω_ϑ close to the vortex centre (see Figures 5.12 b)-e)), and the TV is considered completely developed for $X_C/R_{T,1} \geq 0.132$. Therefore, only the vorticity field extracted in this range is used for the model calibration. It is observed that the radial component of the vorticity is about one order of magnitude less that the other components in the region of the TV viscous core, which support the assumption $\omega_r = 0$ in the TV vorticity model.

The effect of the TV rollup is clearly shown in Figure 5.12 by the trace of the blade wake that moves in the negative z direction during the convection downstream [56,57]. Starting from the axial location where the TV is considered completely developed, the vorticity sheet of the blade wake lies entirely in the half-plane $z < 0$ (Figures 5.12 b)-e)), and the vorticity contained in the region $z > 0$ is ascribed solely to the tip vortex. Therefore, the azimuthal averages of ω_x and ω_ϑ in the range $0 \leq \vartheta \leq \pi$ (enclosed by the white dashed lines in Figure 5.12) can be considered as the axisymmetric distributions of the vorticity components associated with the TV in the local reference frame. In this way, the contribution of a single TV has been singled out.

A quantitative assessment of the azimuthal averaging at different axial locations is given in Figure 5.13. The grey bands represent the ranges between the minimum and maximum values of ω_x and ω_ϑ in the interval $0 \leq \vartheta \leq \pi$, whereas the black lines indicate the azimuthal averages. It is observed that the minimum and maximum values of ω_x differ very little from the average, confirming that the axial component of the vorticity is essentially axisymmetric. Concerning ω_ϑ, the variation band is wider. Nevertheless, the assumption of axial symmetry is considered acceptable.

At each extraction grid, the azimuthally averaged profiles of ω_x and ω_ϑ are fitted with the corresponding vorticity distribution of Eq. (5.7) to calibrate the unknown parameters of the model, i.e., Γ, r_c and $V_{x,def}$, along the vortex helix. The fitting was performed using the Trust-Region-Reflective algorithm available in MATLAB. First, the axial component is fitted, so determining Γ and r_c at each axial position. Then, $V_{x,def}$ is balanced by fitting the tangential component of the vorticity. Note that the choice of calibrating parameters r_c and Γ together is arbitrary. As an alternative, the couple r_c and $V_{x,def}$ could be calibrated by fitting ω_ϑ, and Γ could be balanced

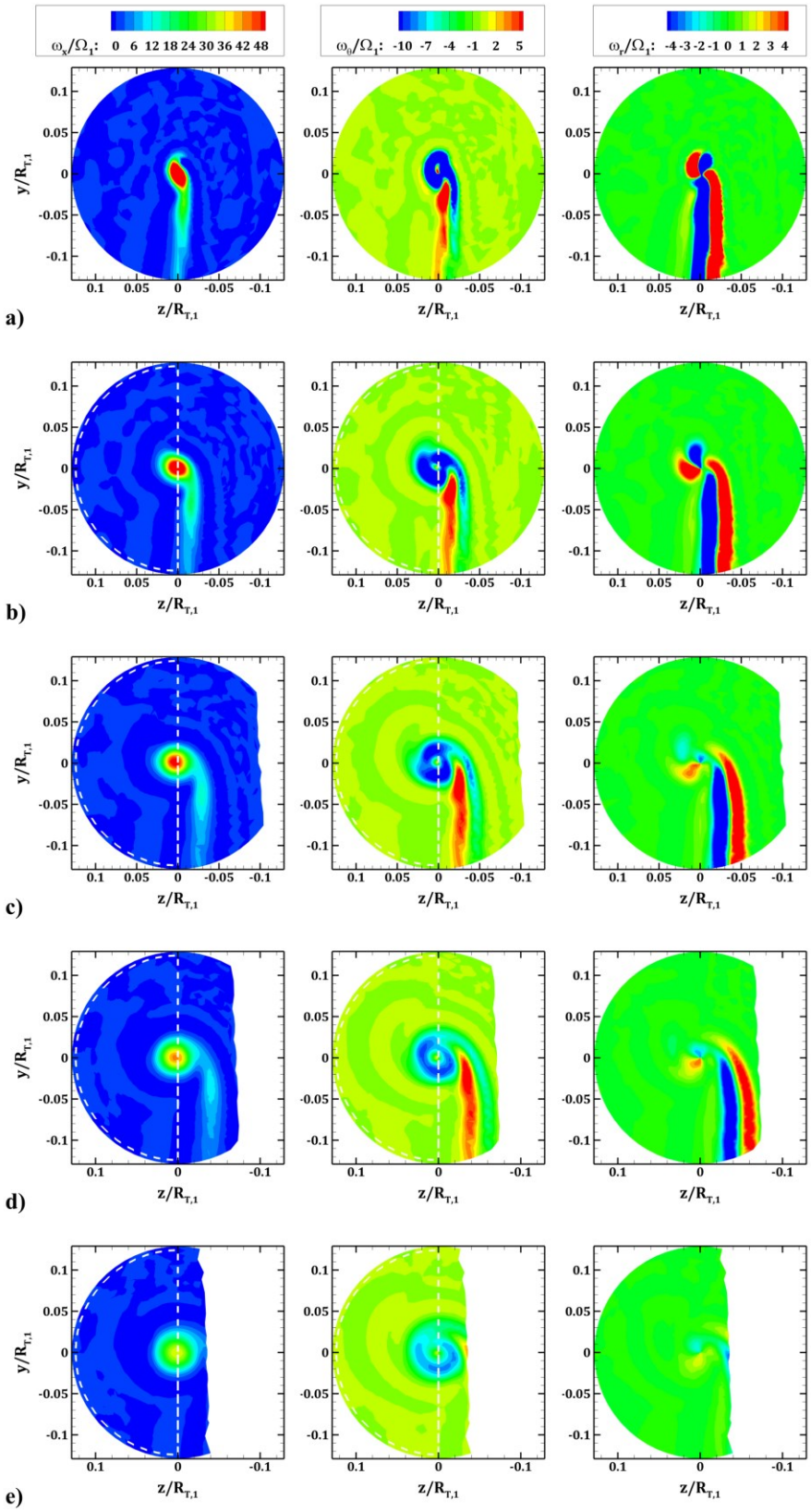

Figure 5.12 – Vorticity contours in the local reference frame of the TV, extracted from RANS solution at different axial locations: **a)** $X_C/R_{T,1} = 0.112$, **b)** $X_C/R_{T,1} = 0.132$, **c)** $X_C/R_{T,1} = 0.161$, **d)** $X_C/R_{T,1} = 0.190$, **e)** $X_C/R_{T,1} = 0.233$.

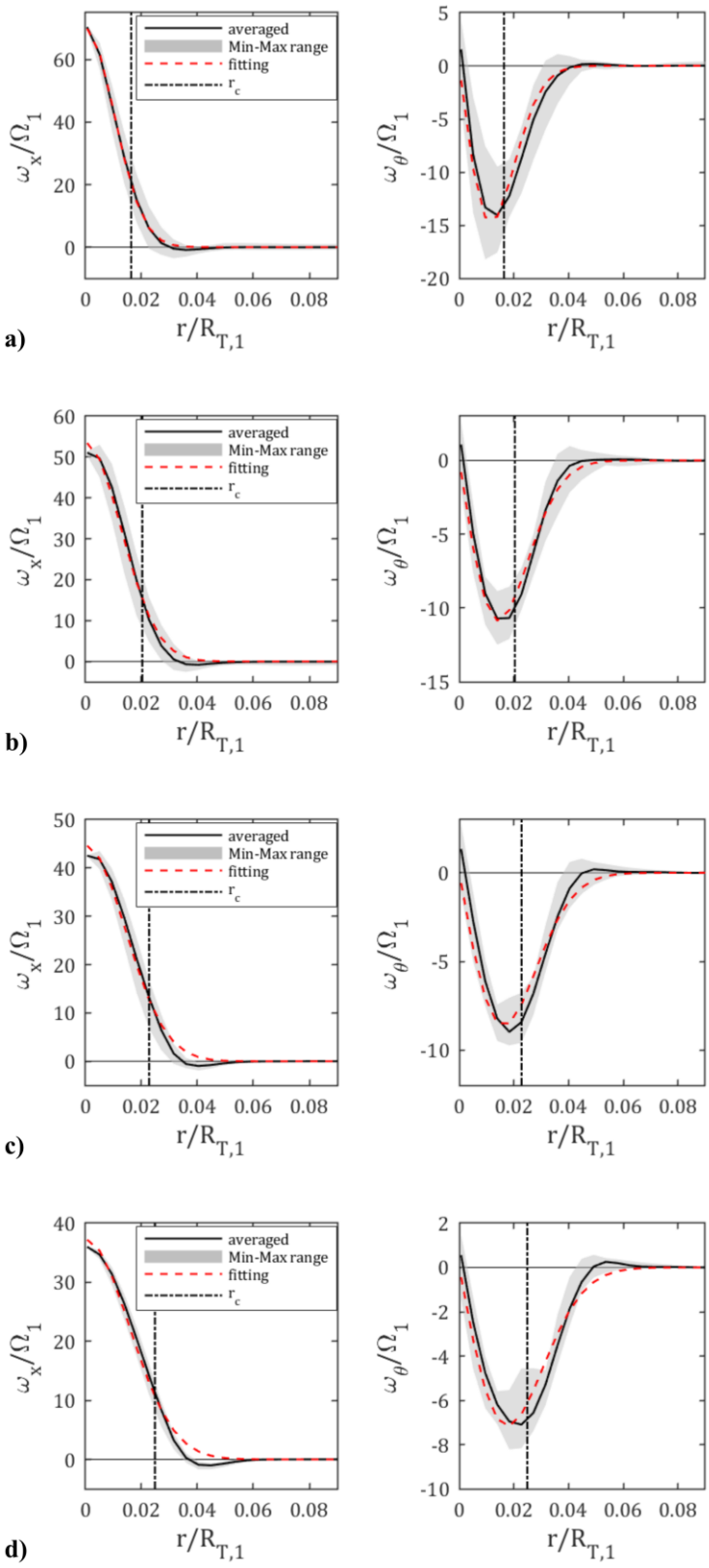

Figure 5.13 – Fitting of the vorticity in the local reference frame of the TV at different axial locations: **a)** $X_C/R_{T,1} = 0.132$, **b)** $X_C/R_{T,1} = 0.161$, **c)** $X_C/R_{T,1} = 0.190$, **d)** $X_C/R_{T,1} = 0.233$.

subsequently by fitting ω_x . A further possibility is to calibrate all three parameters simultaneously. Nevertheless, the coupled calibration of one of the two parameters, Γ or $V_{x,def}$, with r_c should give a more accurate identification of that parameter, since the fitting model has two degrees of freedom. As it will be shown later on, the velocity deficit is non-zero within a region of very limited extent close to the TV trajectory, whereas the induced velocity exhibits a significant magnitude along a wide portion of the rear blade span. Therefore, it is preferable to privilege the accuracy in the identification of Γ instead of $V_{x,def}$.

In Figure 5.13, red dashed lines represent the fitted profiles. A very good agreement with the averaged profiles is obtained for component ω_x, with slight differences limited to the outer region of the vortex core where the vorticity tends to zero. Also fitted component ω_ϑ exhibits moderate deviations at the outer radii, accompanied by a slight radial shift of the profiles. The latter misalignment is most probably a consequence of the choice to calibrate r_c and ω_x together, thus letting $V_{x,def}$ to be the only free parameter for the ω_ϑ fitting. Nevertheless, the observed deviations are minor and the result of the overall fitting can be considered satisfactory.

Figure 5.13 also shows that the fitted r_c (black dotted lines) increases moving downstream, according to the diffusion of the viscous core.

After calibrating the velocity parameters Γ, r_c and $V_{x,def}$ at each extraction grid, their axial distributions are fitted by means of Eqs. (5.21)-(5.23). In Figure 5.14, the empty circles represent the velocity parameters at all the extraction grids considered, while the black solid lines represent their analytical fitting. r_c and $V_{x,def}$ are normalized with respect to the FR tip radius and the freestream velocity, respectively. It is observed that the fitted distributions represent well the axial evolution of the parameters in the region from the FR trailing edge to the MP. An increase in the TV circulation moving downstream is clearly visible in Figure 5.14 a), indicating that an ingestion of vorticity takes place during the vortex rollup and supporting the model assumption of a variable circulation along the vortex trajectory.

The values of the parameters of the axial distributions of r_c, $V_{x,def}$ and Γ (see Eqs. (5.21)-(5.23)) obtained for the present test case are reported in Table 5.2. The parameters are normalized using the FR tip radius and the freestream velocity (apart from parameters related to the circulation, Γ_I and $K_{\Gamma 1}$, which are kept dimensional).

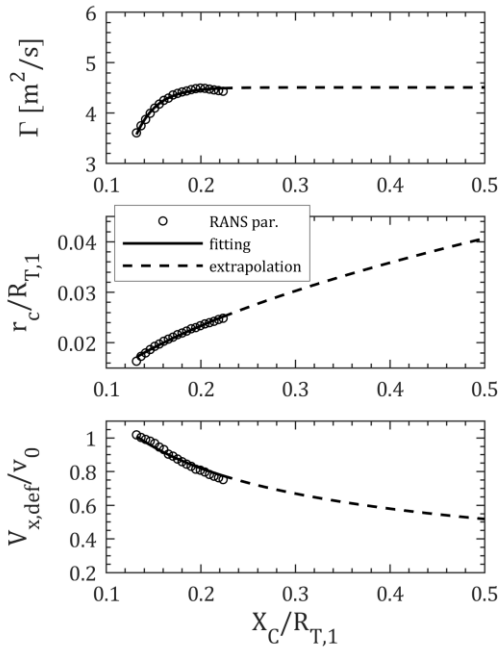

Figure 5.14 – Calibrated velocity parameters and fitted analytical distributions along the TV helix. **a)** Circulation, **b)** Viscous core radius, **c)** Peak of the axial velocity deficit.

Table 5.2 – Parameters of the axial distributions of r_c, $V_{x,def}$ and Γ.

$r_I/R_{T,1}$	$r_X/\sqrt{R_{T,1}}$	V_I/v_0	$V_X/(v_0\sqrt{R_{T,1}})$	Γ_I $\left[\frac{\mathrm{m}^2}{\mathrm{s}}\right]$	$K_{\Gamma 1}$ $\left[\frac{\mathrm{m}^2}{\mathrm{s}}\right]$	$K_{\Gamma 2} \cdot R_{T,1}$
0.0139	0.0608	$3.3564 \cdot 10^{-16}$	0.3665	2.3020	2.2078	44.5683

5.5 Velocity field ascribed to the tip vortices

Once the TV model parameters have been calibrated, the velocity field generated by a single tip vortex is evaluated at any point of the space by means of the Biot-Savart law (Eq. (5.18)) and Eq. (5.20). Then, the velocity field due to the vortices released by all the FR blades is computed as the superposition of the single contributions according to Eq. (5.24). In order to calculate the unsteady loading on the rear blades, the velocity field of the TVs is extrapolated beyond the MP, and evaluated along circumferences located at the LE of the rear rotor, that is, along the curve $X_{LE,2}(R)$. Figure 5.15 shows the contours of the absolute velocity components due to all the TVs, computed at the surface of revolution generated by the curve $X_{LE,2}(R)$ and represented in the coordinate system (X, R, Ψ) of the FR. The velocity field due to the TVs is steady in such a

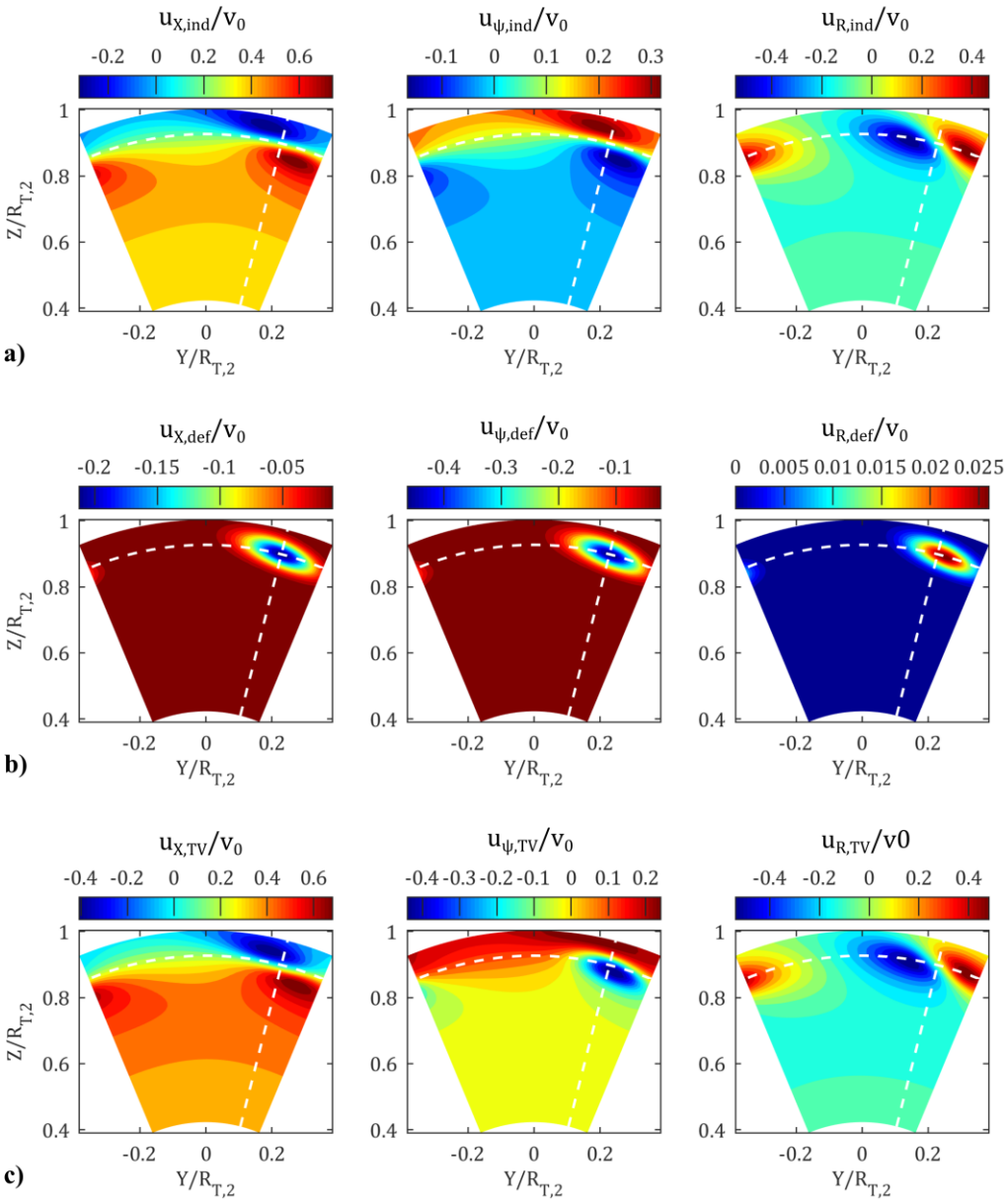

Figure 5.15 – Contours of the velocity components due to the tip vortices, computed at the rear rotor inlet (surface of revolution generated by the curve $X_{LE,2}(R)$). **a)** Velocity induced by the circulation, $\boldsymbol{u}_{ind}$, **b)** axial velocity deficit, $\boldsymbol{u}_{def}$, **c)** total, $\boldsymbol{u}_{TV} = \boldsymbol{u}_{ind} + \boldsymbol{u}_{def}$.

coordinate system. The considered azimuthal range is limited to one blade passage of the FR, since the flow field is periodic, and it repeats identically in the other blade passages. The angular sectors depicted in Figure 5.15 represent the projection of the surface of revolution onto plane (Y, Z). Figures 5.15 a) and b) show the contributions of the circulation and the axial velocity deficit, respectively, while Figure 5.15 c) shows the total velocity $\boldsymbol{u}_{TV} = \boldsymbol{u}_{ind} + \boldsymbol{u}_{def}$. The spatial coordinates are normalized with respect to the RR tip radius and the velocity components are normalized using the freestream velocity. The white dashed circular and straight lines indicate

the radial and azimuthal coordinates, respectively, of the point where the vortex helix intersects the surface of revolution (only one of the helices intersects the surface within one blade passage). Note that the induced velocity maintains a significant magnitude at large distances, compared to the viscous core radius, from the vortex helix. Therefore, it is expected that the flow fields of the individual vortices influence significantly each other at the location of the RR leading edge, and this is automatically accounted for by the model. Concerning the axial deficit, its magnitude tends rapidly to zero as the distance from the vortex centre is increased (see Figure 5.15 b)), and hence there is no mutual influence of adjacent TVs. In fact, the viscous core radius, which is directly related to the standard deviation of the gaussian function defining $\boldsymbol{u}_{def,k}$ (see Eq. (5.20)), is of order $r_c/R_T = O(10^{-2})$ close to the RR leading edge. Nevertheless, the maximum magnitudes of $\boldsymbol{u}_{ind}$ and $\boldsymbol{u}_{def}$ are comparable, and therefore the contribution of the axial deficit must be properly taken into account for the computation of the unsteady loading on the RR blades. Finally, it is observed that the radial component of $\boldsymbol{u}_{def}$ is one order of magnitude lower than the axial and tangential ones, because of the small contraction angle of the analytical vortex helix close to the RR leading edge (see Figure 5.8 a)). By comparing Figures 5.15 a) and c) it is also noted that $u_{R,TV}$ is slightly influenced by the contribution $u_{R,def}$, unlike the axial and tangential velocity components.

5.6 Merging TV and 2D flow perturbations

Considering the RANS solution in the region between the FR trailing edge and the mixing plane, we denote by $\boldsymbol{v'}_{2D}$ the azimuthal flow perturbations generated by flow structures other than tip vortices, that is, the viscous wake and the potential field bound to the FR blades. Perturbations $\boldsymbol{v'}_{2D}$ are obtained by subtracting the tip vortex flow field from the RANS solution. The 2D extrapolation model is then used to propagate $\boldsymbol{v'}_{2D}$ through the MP, up to the leading edge of the RR. Finally, the extrapolated $\boldsymbol{v'}_{2D}$ is added to the tip vortex contribution, $\boldsymbol{v'}_{TV}$, to obtain the complete description of the azimuthal perturbations responsible for the unsteady loading on the rear blades.

5.6.1 Subtraction of the tip vortex velocity field from the RANS solution

For a proper calibration of the 2D model, the influence of the TVs must be removed from the RANS flow field, so that $\boldsymbol{v'}_{2D}$ can be isolated. Recalling Eqs. (5.2) and (5.3), the RANS flow field between the FR trailing edge and the MP can be split into the azimuthal average and the perturbations in azimuthal direction, i.e., $\boldsymbol{v}_{RANS} = \overline{\boldsymbol{v}}_{RANS} + \boldsymbol{v'}_{RANS} = \overline{\boldsymbol{v}}_{RANS} + \boldsymbol{v'}_{2D} + \boldsymbol{v'}_{TV}$.

Contribution $\boldsymbol{u'}_{TV}$, computed by means of the TV model, is subtracted from the RANS solution, and the fitting of the 2D model is performed using the resulting perturbations:

$$\begin{aligned}\boldsymbol{v'}_{2D}(X,R,\Psi) &= \boldsymbol{v}_{RANS}(X,R,\Psi) - \overline{\boldsymbol{v}}_{RANS}(X,R) - \boldsymbol{u'}_{TV}(X,R,\Psi) = \\ &= \boldsymbol{v'}_{RANS}(X,R,\Psi) - \boldsymbol{u'}_{TV}(X,R,\Psi)\,.\end{aligned} \tag{5.27}$$

To do this, the TV velocity field $\boldsymbol{u}_{TV}$ is calculated as circumferential profiles at different axial positions along azimuthally averaged streamlines, and the perturbations $\boldsymbol{u'}_{TV}$ are computed as $\boldsymbol{u'}_{TV} = \boldsymbol{u}_{TV} - \overline{\boldsymbol{u}}_{TV}$, where $\overline{\boldsymbol{u}}_{TV}$ is the azimuthal average.

Figure 5.16 shows the (X,R) coordinates of the circumferential profiles considered for the calibration of the 2D model along streamlines 30, 46 and 55. The black dashed lines represent these averaged streamlines, while the empty circles indicate the locations of the 8 circumferential profiles considered. The numbering of the axial locations runs from $i = 1$ at the FR trailing edge to $i = 8$ close to the MP. The TV trajectory is indicated by the red dash-dotted line. Figure 5.17 compares $\boldsymbol{v'}_{RANS}(X_i,\Psi)$, $\boldsymbol{u'}_{TV}(X_i,\Psi)$ and $\boldsymbol{v'}_{2D}(X_i,\Psi)$, showing the effect of removing the TV velocity perturbations. Figures 5.17 a), b) and c) refer to the axial location $i = 4$ along streamlines 30, 46 and 55, respectively. Although $\boldsymbol{u}_{TV}$ has a significant magnitude up to the rotor hub, it was found that the amplitude of $\boldsymbol{u'}_{TV}$ decreases moving radially inward from the TV helix. Figure 5.17 a) shows that when the radial distance from the TV trajectory is sufficiently large, $\boldsymbol{v'}_{2D}$ differs slightly from $\boldsymbol{v'}_{RANS}$, indicating that the flow field in this region is not influenced by the

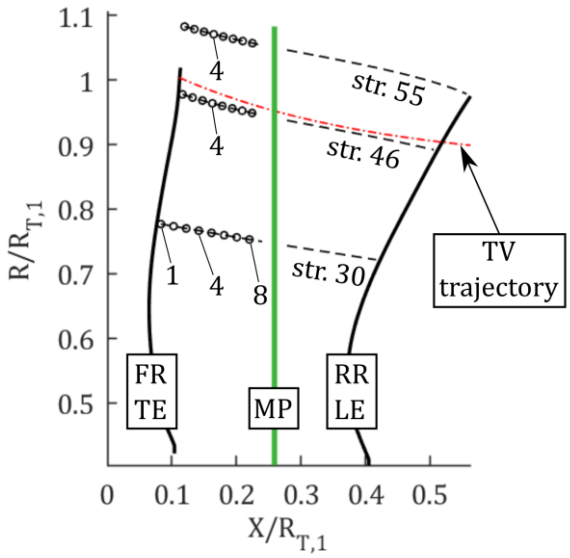

Figure 5.16 – Azimuthally averaged streamlines 30, 46 and 55 (dashed lines), and locations of the circumferential profiles for the calibration of the 2D model (empty circles).

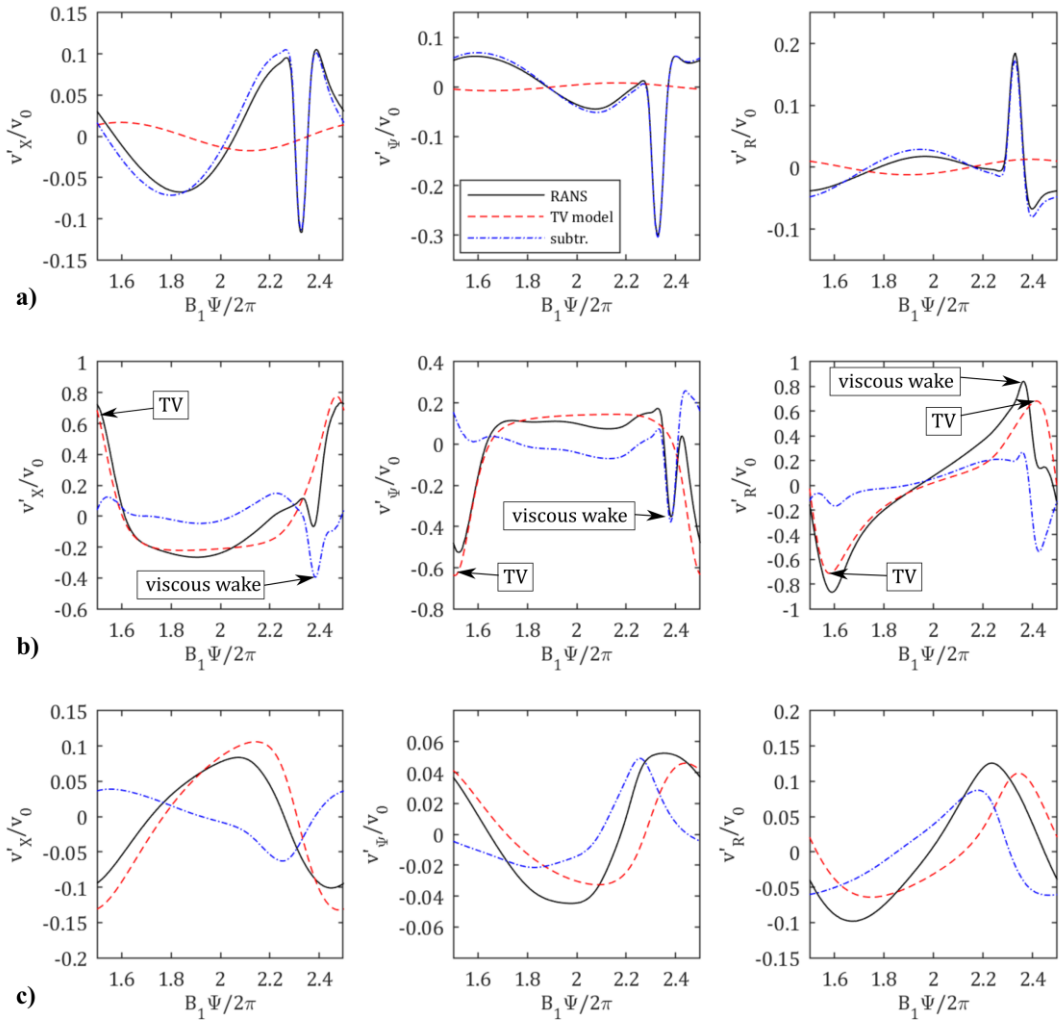

Figure 5.17 – Comparison of the velocity perturbations $\boldsymbol{v}'_{RANS}$ (black solid lines), $\boldsymbol{u}'_{TV}$ (red dashed lines) and $\boldsymbol{v}'_{2D}$ (blue dash-dotted lines), computed at the axial location $i = 4$ along azimuthally averaged streamlines.
a) streamline 30, **b)** streamline 46, **c)** streamline 55.

three-dimensional effects due to the tip vortices. In fact, the velocity profiles exhibit an almost 2D behaviour, and the influence of the viscous wake can be clearly identified by local peaks (at $B_1\Psi/2\pi = 2.33$ in Figure 5.17 a)).

The influence of the tip vortices increases at reducing the radial distance from the TV helix. In Figure 5.17 b), the peaks of $\boldsymbol{v}'_{RANS}$ due to the viscous wake are still visible, but secondary strong peaks are observed at $B_1\Psi/2\pi = 1.51$ for the axial and tangential components, and at $B_1\Psi/2\pi = 1.59$ for the radial component. The red dashed lines show that contribution $\boldsymbol{v}'_{TV}$ dominates the velocity perturbations within the entire azimuthal range, and that the secondary peaks can certainly be ascribed to the tip vortices. When $\boldsymbol{u}'_{TV}$ is subtracted from the overall perturbation field, the resulting velocity profiles ($\boldsymbol{v}'_{2D}$) show features similar to those observed

at smaller radii, where the flow field can be considered approximately two-dimensional (compare blue dash-dotted lines in Figures 5.17 a) and b)). Note that the three-dimensional effects are significant up to the outermost streamline (streamline 55), as can be observed in Figure 5.17 c).

5.6.2 Calibration of the 2D flow model

The perturbation field $\boldsymbol{v'}_{2D}$, computed from RANS data according to Eq. (5.27), is used to calibrate the 2D model of the viscous wake and potential field due to the front rotor blades. In the present application, $\boldsymbol{v'}_{2D}$ was extracted at 8 axial locations along each averaged streamline (see Figure 5.16).

To assess the effect of removing the TV velocity perturbations, the model fitting has been performed using both $\boldsymbol{v'}_{RANS}$ (as done by Jaron et al. [42]) and $\boldsymbol{v'}_{2D}$, and representative results are shown in Figure 5.18 and Figure 5.19, respectively. The black solid lines represent the velocity perturbations to be fitted, while the red dashed lines represent the model velocity u'. For a clearer visualization, only the profiles at the axial locations i $= 2, 4$ and 6 are shown. Consider that the trend of the fitting is the same at the other axial locations.

Figure 5.18 a) refers to streamline 46, where the flow field is strongly influenced by the tip vortices. It is observed that the presence of three-dimensional effects leads to a wrong calibration of the model, even though the quality of the fitting may appear good. This is particularly evident

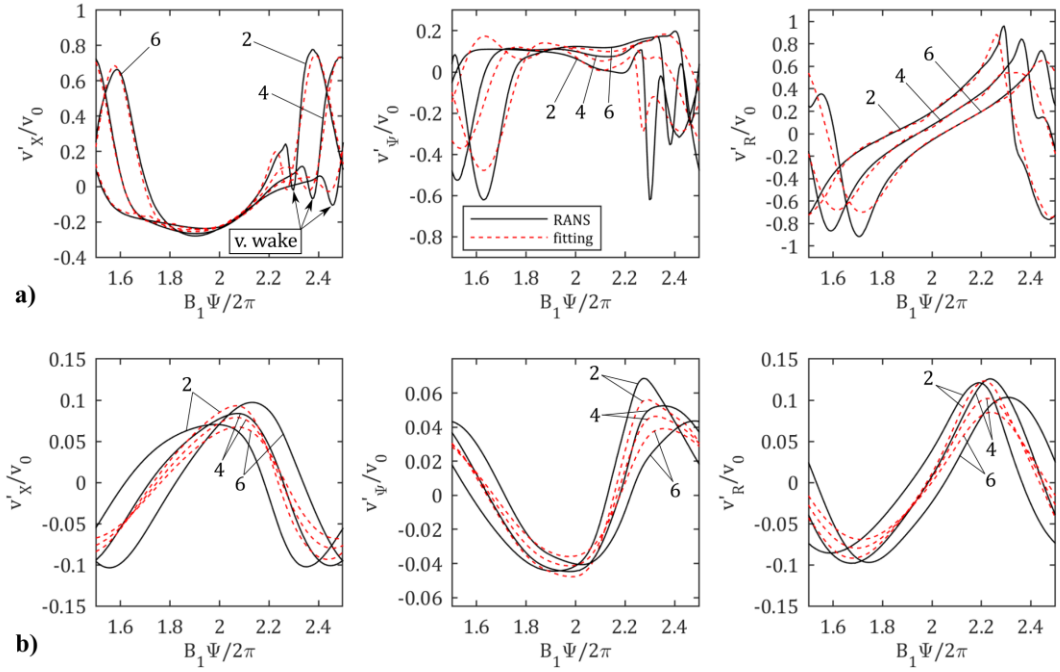

Figure 5.18 – Fitting of the 2D flow model using $\boldsymbol{v'}_{RANS}$. Velocity profiles at axial locations $i = 2, 4$ and 6. **a)** streamline 46, **b)** streamline 55.

for component v'_X. In this case, the positive peaks due to the TVs are considerably stronger than the peaks due to the viscous wake (indicated by the arrows), and the fitting procedure ascribes these TV peaks to the wake contribution, u'_w, leading to an incorrect identification of the 2D model parameters. A similar behaviour is found for the tangential and radial velocity components. Note that a bad fitting of the wake contribution automatically affects the identification of the parameters of the potential field model.

The fitting of $\boldsymbol{v'}_{RANS}$ on streamline 55 is shown in Figure 5.18 b). This streamline passes over the FR blade, and hence only the potential field contribution is considered. The bad quality of the fitting indicates that the model velocity u'_p is inappropriate to describe the perturbations at the outer radii if the TV contribution is not removed from the RANS solution. In fact, considering the axial distribution of u'_p in Eq. (4.2), wavenumber $(M_X^2 \tan\beta_{rel}\,(X - X_{TE,1})/(1 - M_X^2)R)$ and

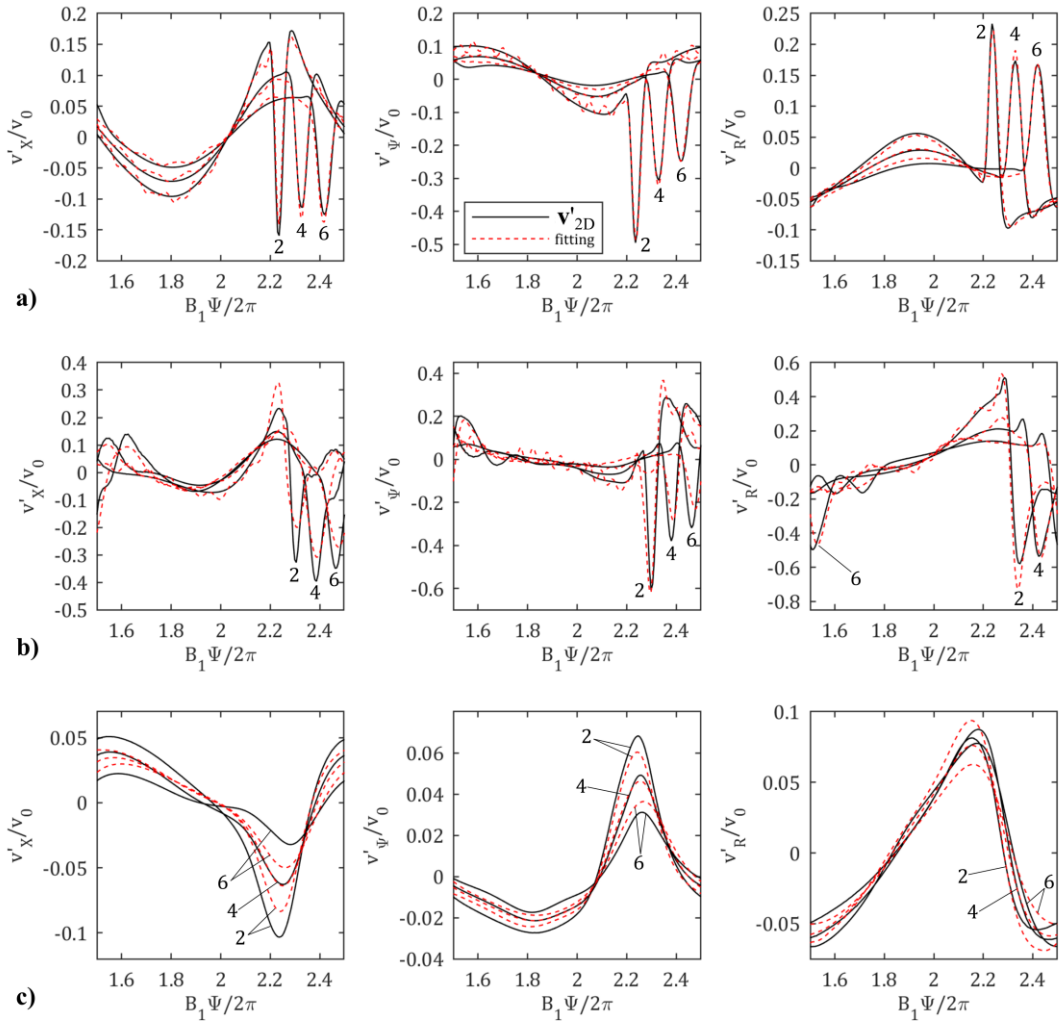

Figure 5.19 – Fitting of the 2D flow model using $\boldsymbol{v'}_{2D}$. Velocity profiles at axial locations $i = 2, 4$ and 6. **a)** streamline 30, **b)** streamline 46, **c)** streamline 55.

amplitude decay rate ($exp\left\{-\left[hB_1\sqrt{1-M_{rel}^2}\left|X-X_{TE,1}\right|/(1-M_X^2)R\right]\right\}$) are quite different from those of the TV (see Eqs. (5.15)-(5.17) and (5.19)-(5.20)).

Figure 5.19 a) shows the fitting performed using $\boldsymbol{v}'_{2D}$ on streamline 30, where the three-dimensional effects of the TV are negligible. The quality of the fitting is very good, in spite of small fluctuations due to higher order harmonics. Similar results were obtained for all the streamlines where $\boldsymbol{v}'_{TV}$ is small compared to $\boldsymbol{v}'_{RANS}$ (from the hub to $R/R_{T,1} \approx 0.85$).

The impact of removing $\boldsymbol{u}'_{TV}$ from $\boldsymbol{v}'_{RANS}$ on the calibration of the 2D flow model emerges from the comparison of Figures 5.19 b-c) with Figures 5.18 a)-b). Figure 5.19 b) refers to streamline 46 and shows that the peaks due to the viscous wake, emphasized by the removal of the three-dimensional effects (compare with Figure 5.18 a)), are clearly identified by the model. Although the match is not perfect, the calibration based on $\boldsymbol{v}'_{2D}$ leads to physically meaningful values of the unknown parameters of both $u'_w(X,\Psi)$ and $u'_p(X,\Psi)$. In Figure 5.19 c), which refers to streamline 55, it can be observed that the 2D model is able to reproduce the axial evolution of $\boldsymbol{v}'_{2D}$ reasonably well, resulting in a significant improvement compared to the fitting based on $\boldsymbol{v}'_{RANS}$ in Figure 5.18 b). Similar results are obtained for all the streamlines where the influence of the TVs is not negligible.

Although the fitting of the 2D flow model using $\boldsymbol{v}'_{2D}$ appears satisfactory, some inconsistencies can be observed in Figures 5.19 b) and c). In fact, the plots in Figure 5.19 b) show small oscillations of v'_Ψ and v'_R in the azimuthal range $1.5 < B_1\Psi/2\pi < 1.75$, which can be hardly justified by the superposition of typical velocity profiles of the wake and potential flows generated by the FR blades. Moreover, the last plot in Figure 5.19 c) shows that the amplitude v'_R increases from $\mathrm{i} = 2$ to $\mathrm{i} = 4$, in contrast to the perturbation decay that should occur at increasing X. This behaviour is observed also in Figure 5.18 b), but in that case it could be justified by the increasing influence of $\boldsymbol{v}'_{TV}$ when moving downstream along streamline 55.

The above inconsistencies can be ascribed to the model approximations, that is, the assumption of linear superposition of perturbations and the simplified model of the flow field around the tip vortex. Nevertheless, these inaccuracies are minor effects, and the general quality of the fitting is substantially improved on almost all the streamlines where the 3D effects of the tip vortices are significant. Consequently, also the velocity perturbations extrapolated beyond the mixing plane should be more physically consistent.

6 RESULTS

The results of the numerical simulations and the predictions of the considered semi-analytical models are presented in order to assess and validate the present method for the fast prediction of the IN tones emitted by the rear rotor. First, the results of the RANS and URANS simulations are validated against experimental data. The comparison between RANS and URANS flow fields is also presented. The extrapolated velocity perturbations, computed at the RR leading edge, are compared with the URANS solution to assess the reconstruction of the flow unsteadiness by means of the RANS-informed model. Then, a comparison between the unsteady loading provided by the blade response model and the one computed from the URANS blade pressure is presented. The IN emission is evaluated and compared with the results of the FWH analogy. Finally, a comparison between the predicted noise emission and wind tunnel noise measurements found in the literature is presented.

6.1 Numerical simulations

6.1.1 Validation of the CFD simulations

Since the reproduced and actual blade geometries are not identical, local differences between computed and real flow fields may occur under the same operating condition. Therefore, it was decided to compare the numerical predictions with measured integral quantities representative of the CROR performance to assess whether the main features of the computed flow field (viscous wake velocity deficit, tip vortex intensity, stream-tube contraction, etc.) are consistent with the considered operating condition. In this view, the benchmark for the simulated test case is the experiment conducted in the 9- by 15- Anechoic Wind Tunnel at NASA Lewis Research Center [50]. The operating condition is representative of take-off at freestream Mach number $M_0 = 0.2$. The scaled CROR model built for the experiment had rotor diameters $D_1 = 0.622\ m$ for the FR and $D_2 = 0.607\ m$ for the RR. In the present work, the 8 x 8 blade number configuration (the notation refers to the number of blades of the FR and the RR) was considered, with axial distance $\Delta X_a = 0.15\ m$ between the pitch change axes of the rotors, corresponding to $\Delta X_a / R_{T,1} = 0.482$ (see Figure 3.1). The operating parameters are summarized in Table 6.1. β_1 and β_2 are the nominal pitch angles of the blades, while J_1 and J_2 are the advance ratios of the two rotors ($J = v_0/(nD)$).

Table 6.1 – Test case operating condition.

Blades number	FR speed [rpm]	RR speed [rpm]	β_1 [deg]	β_2 [deg]	J_1	J_2
8 x 8	7610	7120	36.2	38.4	0.862	0.951

Table 6.2 – Errors of the RANS and URANS predictions.

$\Delta\beta_1$ [deg]	$\Delta\beta_2$ [deg]	Q_1 Err [%]	Q_2 Err [%]	T Err [%]	η_{net} Err [%]
RANS					
-1	-1	1.02	-3.61	-0.92	-0.41
URANS					
-1	-1	1.04	-1.83	0.07	-0.48

In order to improve the matching of computational and experimental results, slight pitch angle corrections, $\Delta\beta_1$ and $\Delta\beta_2$, have been applied. This is a common procedure in propeller simulations (see Mikkelson et al. [63]). The final corrections resulting from a reasonable number of numerical simulations are reported in Table 6.2, together with the corresponding errors in the predictions of torque (Q), total thrust (T) and net efficiency ($\eta_{net} = v_0 T/(\Omega_1 \mathrm{Q}_1 + \Omega_2 \mathrm{Q}_2)$). The prediction errors of the URANS have been computed from the time-average values of torque and thrust after the simulation had reached a converged periodic solution. The small errors obtained are considered as an indication that the main features of the computed and real flow fields are very similar.

6.1.2 RANS flow field

This section reports the velocity and vorticity fields past the CROR resulting from the RANS simulation with the mixing plane boundary condition. The velocity field was extracted at the surfaces S1, S2 and S3 depicted in Figure 6.1. The azimuthal extension of these surfaces corresponds to the angular interval of a single blade passage, that is, $\Delta\Psi = 360°/B_1 = 360°/B_2 = 45°$ for both rotors. In the simulation setup, the pitch change axes of front and rear blades are parallel and the blade passages of FR and RR are aligned. Recalling that the Z axis of the FR reference frame (X, Y, Z) coincides with the PCA of one of the front blades, that is, the simulated blade (see Figure 6.1 a)), the limits of the azimuthal angle of the blade passage considered for both FR and RR are $\Psi_{min} = 90° - 45°/2 = 67.5°$ and $\Psi_{max} = 90° + 45°/2 = 112.5°$.

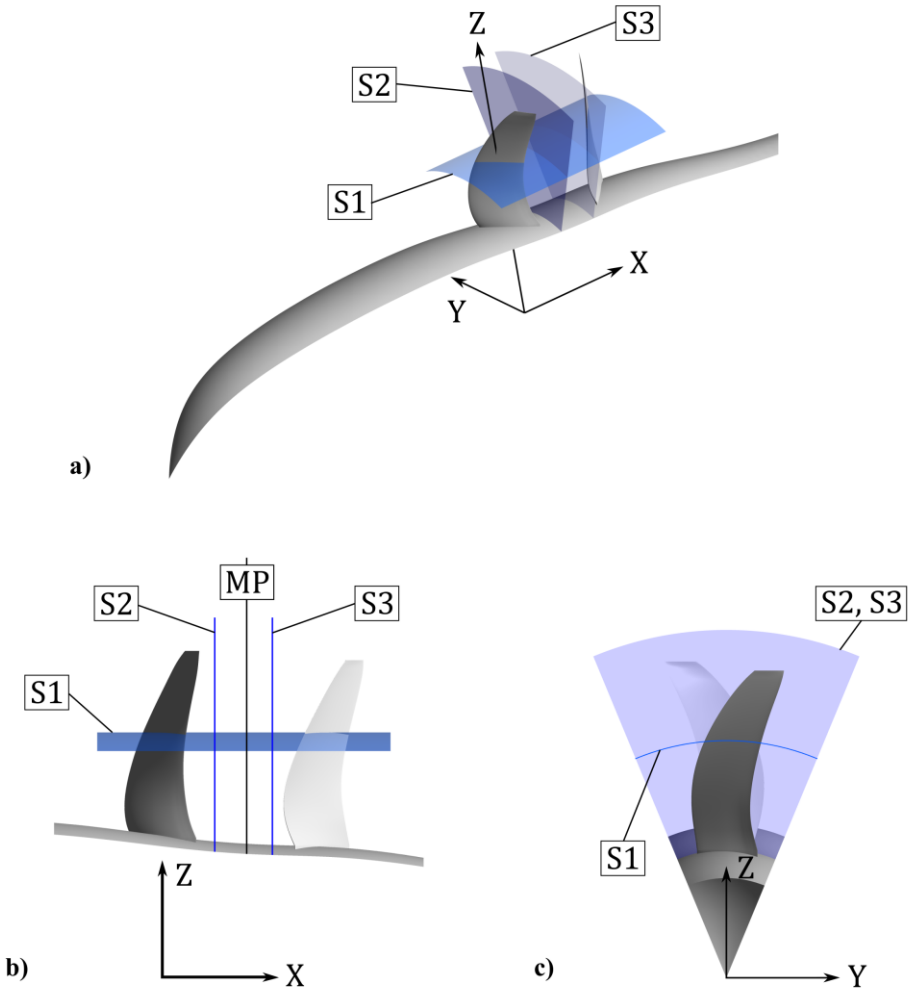

Figure 6.1 – Surface of constant radius $R/R_{T,1} = 0.75$ (S1) and surfaces normal to the rotation axis located at $X/R_{T,1} = 0.161$ (S2) and $X/R_{T,1} = 0.338$ (S3). **a)** 3D view, **b)** projection onto (X, Z) plane, **c)** projection onto (Y, Z) plane.

S1 is a cylindrical surface of radius $R/R_{T,1} = 0.75$ and axial extension $-0.2 \leq X/R_{T,1} \leq 0.7$. As shown in Figure 6.1, this surface intersects both front and rear blades. Surfaces S2 and S3 are normal to the rotation axis and they extend radially from the hub to $R/R_{T,1} = 1.1$. The former is located inside the computational domain of the FR, i.e. upstream of the MP, whereas the latter lies inside the computational domain of the RR, i.e. downstream of the MP (see Figure 6.1 b)). The axial coordinates of S2 and S3 are $X/R_{T,1} = 0.161$ and $X/R_{T,1} = 0.338$, respectively, while the MP is located at $X/R_{T,1} = 0.259$.

Both relative, $\boldsymbol{w}_1$ and $\boldsymbol{w}_2$, and absolute, $\boldsymbol{v}$, velocity fields have been analysed. $\boldsymbol{w}_1$ is defined in the reference frame of the FR (X, Y, Z), while $\boldsymbol{w}_2$ is defined in the frame of reference (X_2, Y_2, Z_2) rotating with the RR. As shown in Figure 6.2, the origins of the two reference frames are coincident, and the Z_2 axis is parallel to the PCA of the rear blade.

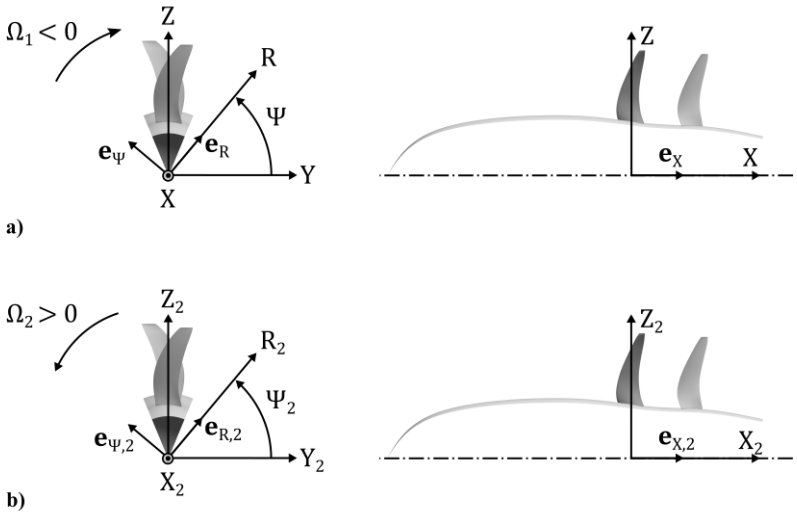

Figure 6.2 – Cartesian and cylindrical coordinate systems in the reference frames of **a)** front rotor, **b)** rear rotor.

Considering the relative velocities in the reference frames of the two rotors, (X, R, Ψ) and (X_2, R_2, Ψ_2), the absolute velocities are simply computed as:

$$\boldsymbol{v}(X, R, \Psi) = \boldsymbol{w}_1 + \Omega_1 \boldsymbol{e}_X \times R\boldsymbol{e}_R = \boldsymbol{w}_1 + \Omega_1 R \boldsymbol{e}_\Psi \ , \tag{6.1}$$

and

$$\boldsymbol{v}(X_2, R_2, \Psi_2) = \boldsymbol{w}_2 + \Omega_2 \boldsymbol{e}_{X,2} \times R_2 \boldsymbol{e}_{R,2} = \boldsymbol{w}_2 + \Omega_2 R_2 \boldsymbol{e}_{\Psi,2} \ , \tag{6.2}$$

where $(\boldsymbol{e}_X, \boldsymbol{e}_R, \boldsymbol{e}_\Psi)$ and $\left(\boldsymbol{e}_{X,2}, \boldsymbol{e}_{R,2}, \boldsymbol{e}_{\Psi,2}\right)$ are the unit vectors of the cylindrical coordinate systems of the FR and RR, respectively (see Figure 6.2). Note that the absolute and relative velocities differ from each other only for the tangential component,

$$v_\Psi(X, R, \Psi) = w_{\Psi,1}(X, R, \Psi) + \Omega_1 R \ , \tag{6.3}$$

$$v_\Psi(X_2, R_2, \Psi_2) = w_{\Psi,2}(X_2, R_2, \Psi_2) + \Omega_2 R_2 \ , \tag{6.4}$$

while the axial and radial components do not change ($v_X = w_{X,1} = w_{X,2}$ and $v_R = w_{R,1} = w_{R,2}$).

The contours in Figure 6.3 show the normalized velocity at the cylindrical surface S1. In the figure, the surface is projected onto plane (X, Y). Figure 6.3 a) reports the map of the axial velocity, v_X, while Figure 6.3 b) shows the tangential components of the relative velocities. $w_{\Psi,1}$

and $w_{\Psi,2}$ are depicted in the region upstream and downstream of the MP, respectively (i.e., in the computational domains of the FR and RR, respectively). The tangential component of the absolute velocities, v_Ψ, is depicted in Figure 6.3 c). The figure shows that the velocity perturbations in space generated by each rotor are suppressed at the MP, where a discontinuity in the contours is clearly visible. For instance, it is observed that the trace of the viscous wake released by the front blade stops abruptly at $X/R_{T,1} = 0.259$ (axial coordinate of the MP). In particular, the flow perturbations in the azimuthal direction, which are responsible for the periodic fluctuation of the blade loads during the rotation, do not propagate through the MP. Indeed, the RANS solution in the computational domain of each rotor is steady in the reference frame of the rotor and it gives a good approximation of the time averaged flow field.

The axial flow acceleration can be observed in Figure 6.3 a). At axial coordinate $X/R_{T,1} = -0.2$ (upstream of the considered section of the front blade), the axial velocity is $1.25 < v_X/v_0 < 1.40$ and it undergoes an increase moving downstream. At $X/R_{T,1} = 0.7$ (downstream of the rear blade section), the range of the axial flow velocity is $1.98 < v_X/v_0 < 2.07$. Similar results were found at other radial coordinates along the blade span.

Looking at the tangential components of the absolute velocity at surface S1 (see Figure 6.3 c)), it is observed that the FR produces a negative swirl velocity that affects the axial region between the front and rear blades. The RR performs an effective recovery of the swirl kinetic energy, as shown by the small values of the azimuthally averaged tangential velocity downstream of the rear blade section ($\bar{v}_\Psi/v_0 = -0.047$ at $X/R_{T,1} = 0.7$). Similar results were found at other radial coordinates along the blade span. This support the assumption of no residual swirl adopted in the modelling of the tip vortex path.

The velocity contours in Figure 6.4 refer to surface S2, which is normal to the rotation axis and located in the computational domain of the FR. The maps of axial, tangential and radial velocity components are shown. Surface S2 span the single blade passage of the FR, where the RANS solution is periodic in the azimuthal direction. On the left side of the figure, the velocity contours are reproduced circumferentially in order to show the full annulus velocity field, and the black lines indicate the boundaries of S2. On the right side of the figure, the contours are limited to S2 for a clearer visualization.

The relative tangential velocity in the reference frame of the FR, $w_{\Psi,1}$, (Figure 6.4 b)), rapidly increases moving radially outward. Figure 6.4 c) shows that v_Ψ, represented in the coordinate system of the FR, is negative in almost the whole region $R/R_{T,1} < 0.95$, illustrating the distribution of the swirl velocity generated by the front blades. Also the radial velocity component, v_R, is negative on almost the entire surface S2 (Figure 6.4 d)), indicating that the flow contracts radially.

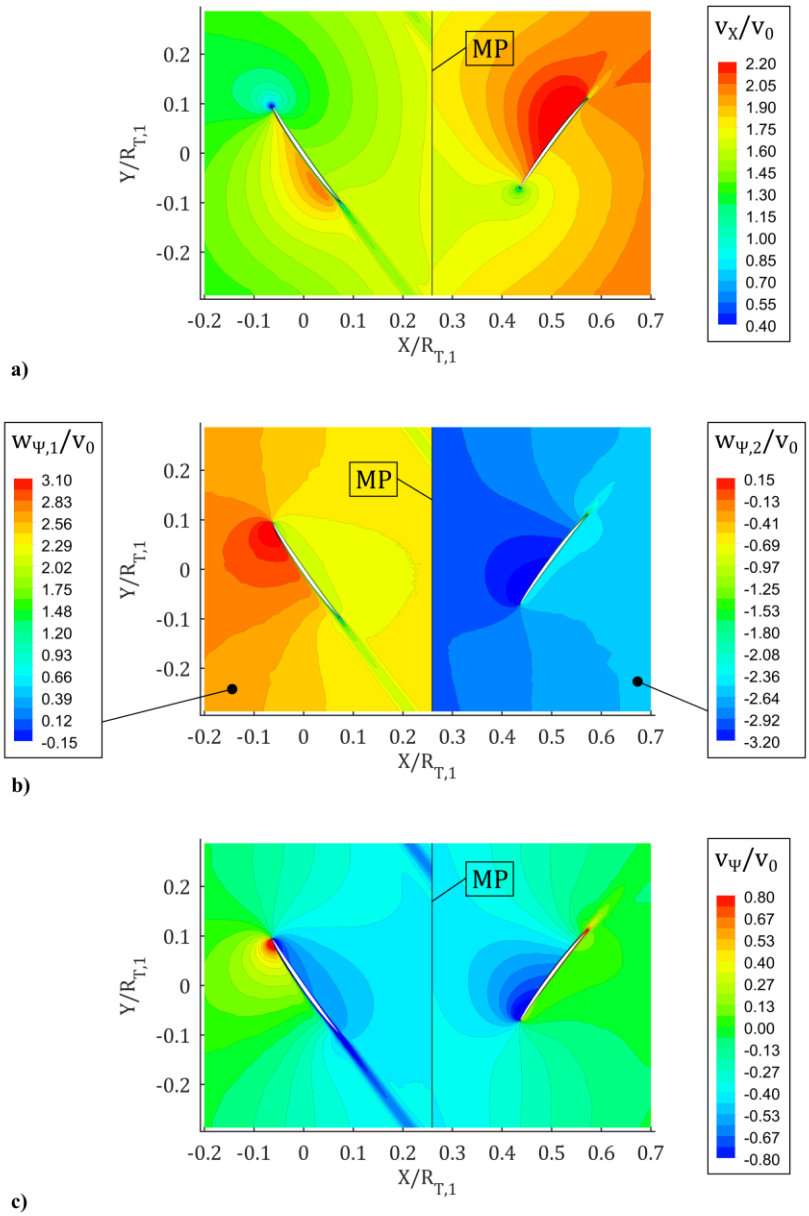

Figure 6.3 – Contours of the velocities extracted from the RANS solution at surface S1. **a)** axial velocity, v_X, **b)** relative tangential velocity, w_Ψ, **c)** absolute tangential velocity, v_Ψ.

The velocity perturbations in space observed in Figure 6.4 are ascribed to viscous wakes, tip vortices and bound potential field of the front blades. In the figure, the trace of the viscous wake is identified by the radial pattern of velocity deficit enclosed by the dashed oval, and it is particularly visible in the maps of v_X (Figure 6.4 a)) and v_Ψ (Figure 6.4 c)). The black circles represent the points where the analytical TV trajectory intersects surface S2. The TVs released by the front blades are mainly responsible for the intense velocity perturbations observed in the regions near the vortex trajectory. For instance, the axial and radial velocity components vary

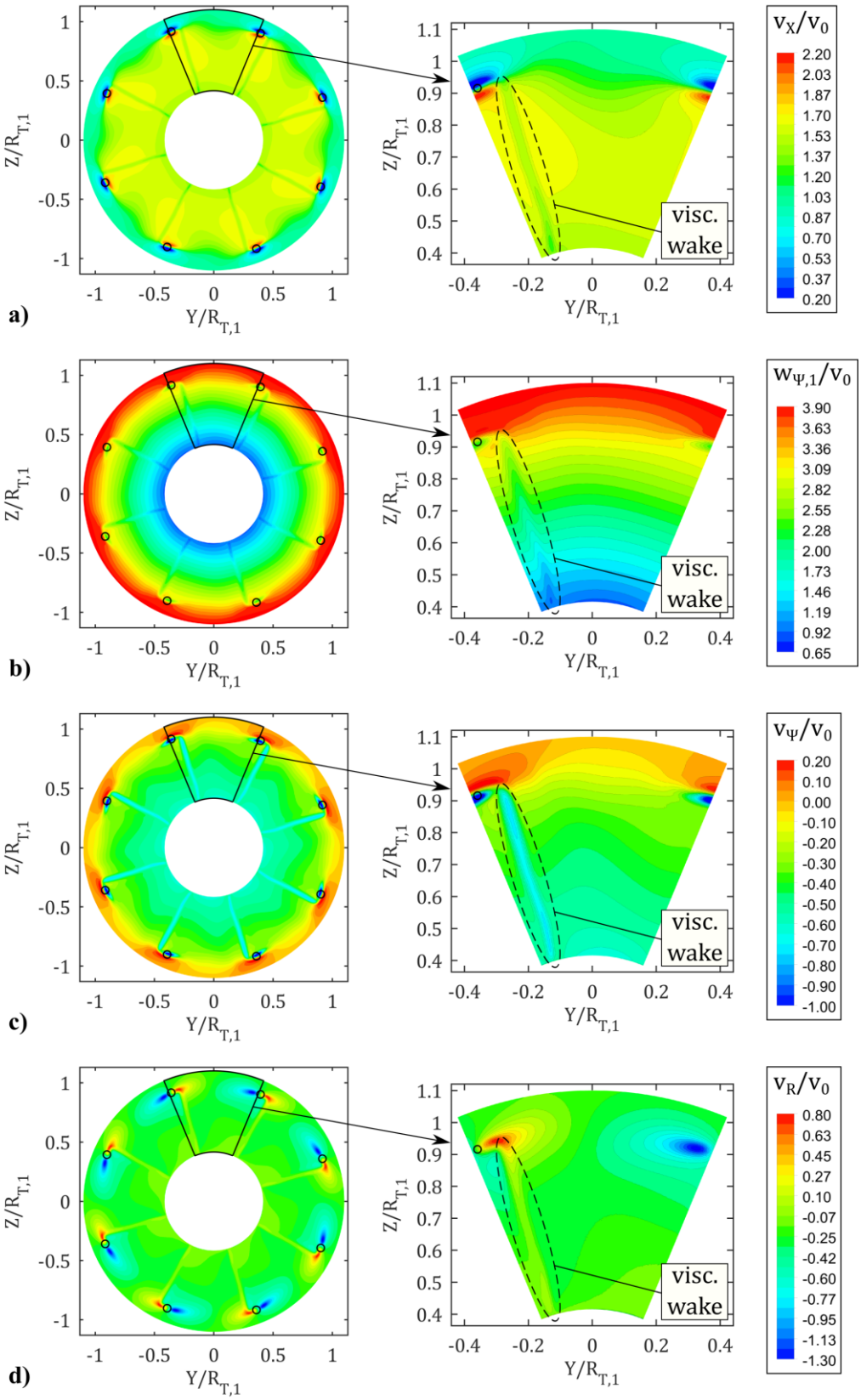

Figure 6.4 – Contours of the velocities extracted from the RANS solution at surface S2. **a)** axial velocity, v_X, **b)** relative tangential velocity, $w_{\Psi,1}$, **c)** absolute tangential velocity, v_Ψ, **d)** radial velocity, v_R.

approximatively in ranges $-0.2 < v_X/v_0 < 2.2$ and $-1.3 < v_R/v_0 < 0.8$, respectively, within regions of limited extension around the TV centres.

The contours in Figure 6.5 show the velocity fields on surface S3, which is normal to the rotation axis and located in the computational domain of the RR. Similarly to Figure 6.4, the full annulus velocity field is depicted on the left side of the figure, while the plots on the right side illustrate the velocity maps over a the single blade passage of the RR. The axial, tangential and radial velocity components are represented in the coordinate system of the RR.

Note that the velocity perturbations in space generated by the FR do not affect the flow on surface S3 since they are suppressed at the MP. Therefore, the perturbations observed in Figure 6.5 are generated by the RR and they are ascribed to the bound potential field of the rear blades.

The stream-tube has undergone a significant radial contraction with respect to the axial position of the front blades. In fact, at the X_2 coordinate of surface S3, the axial velocity and the absolute tangential velocity are nearly $v_X/v_0 = 1$ and $v_\Psi/v_0 = 0$, respectively, for radial coordinates larger than about $R_2/R_{T,1} = 0.93$ (see Figures 6.5 a) and c)). This indicates that the flow in that region lies outside the stream-tube crossing the FR disc, since it does not exhibit the axial acceleration and swirl velocity generated by the front rotor. Moreover, v_R shows significant negative values over S2 (Figure 6.5 d)), meaning that the flow is still contracting radially.

The absolute vorticity, $\boldsymbol{\omega}$, represented in the coordinate system (X, Y, Z) of the FR, is shown in Figures 6.6 and 6.7. The figures illustrate the vorticity calculated by RANS in the computational domain of the FR, i.e., the vorticity released by the front blades. The RANS solution for a single blade passage is repeated circumferentially to visualize the vorticity field over the full annulus result.

Figure 6.6 shows the contours of vorticity magnitude, normalized using the FR angular velocity, at 9 planes normal to the rotation axis, located from $X = 0$ to the MP. The range of the contours is $6 < |\boldsymbol{\omega}|/|\Omega_1| < 44$ and the values outside this interval are not displayed in favour of the visualization of multiple planes. It is observed that the vorticity is generated at the blade surface and is convected downstream, giving rise to tip vortices and viscous wakes. The region of high vorticity indicated by the arrows in Figure 6.6 identifies the viscous core of the TV. Moving downstream, the maximum value of $|\boldsymbol{\omega}|$ within the TV core decreases, while the region where $|\boldsymbol{\omega}|/|\Omega_1| > 6$ enlarges (compare the contours on different planes), due to the vorticity diffusion and viscous dissipation.

In Figure 6.6, the vorticity ascribed to the viscous wake is also visible in the region radially inward with respect to the TV viscous core. Note that the magnitude of the vorticity of the viscous wake is significantly smaller than that of the tip vortex.

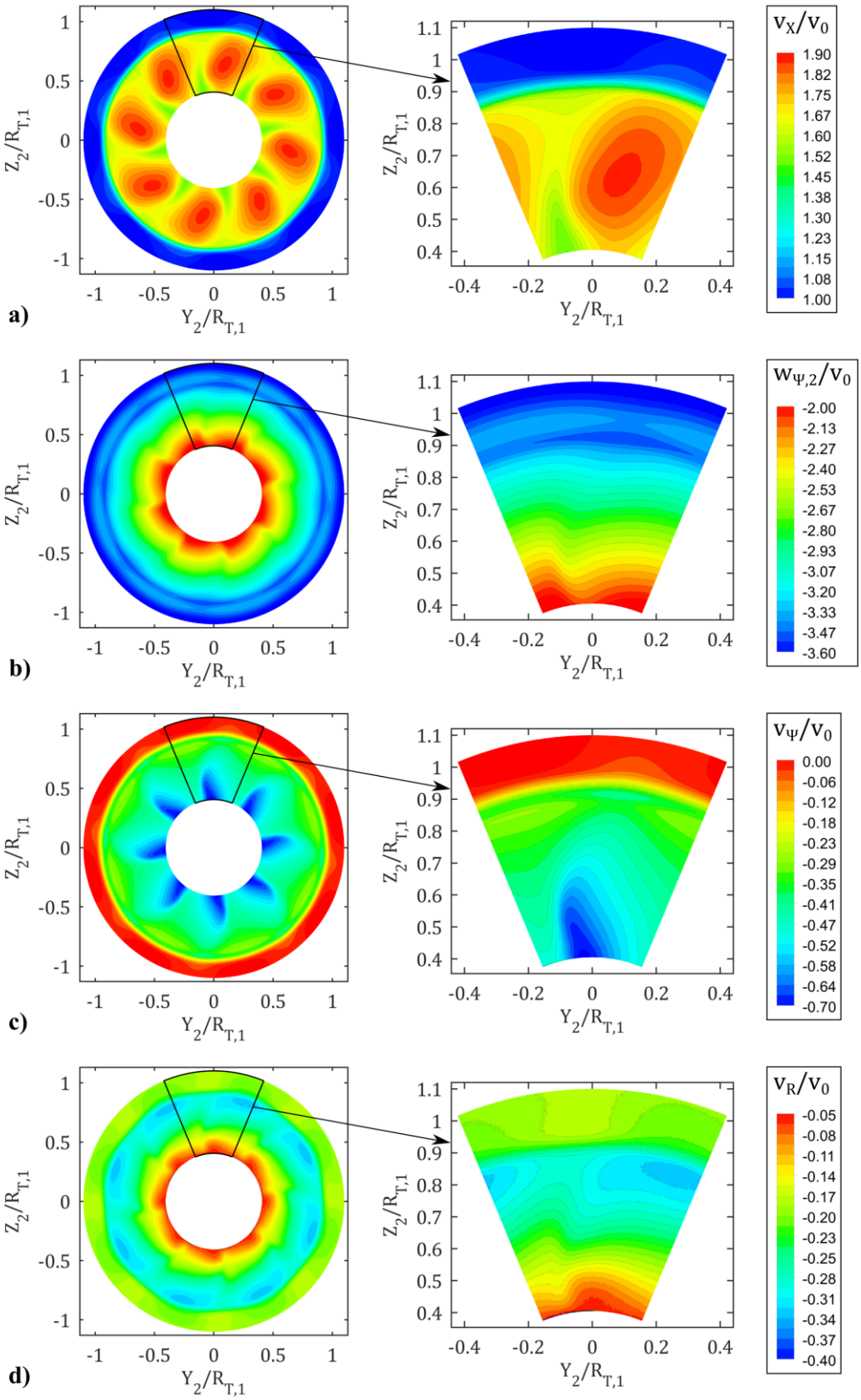

Figure 6.5 – Contours of the velocities extracted from the RANS solution at surface S3. **a)** axial velocity, v_X, **b)** relative tangential velocity, $w_{\Psi,2}$, **c)** absolute tangential velocity, v_Ψ, **d)** radial velocity, v_R.

The blue surfaces in Figure 6.7 are those of constant vorticity magnitude $|\boldsymbol{\omega}|/|\Omega_1| = 10$, and show the morphology of the tip vortices generated by the FR. The vorticity sheet released by the front blade quickly rolls up while moving downstream from the tip trailing edge, generating the tube-shaped surface of $|\boldsymbol{\omega}|/|\Omega_1| = 10$ indicated by the arrows in the figure. This surface encloses most of the TV viscous core and provides a representation of the TV shape.

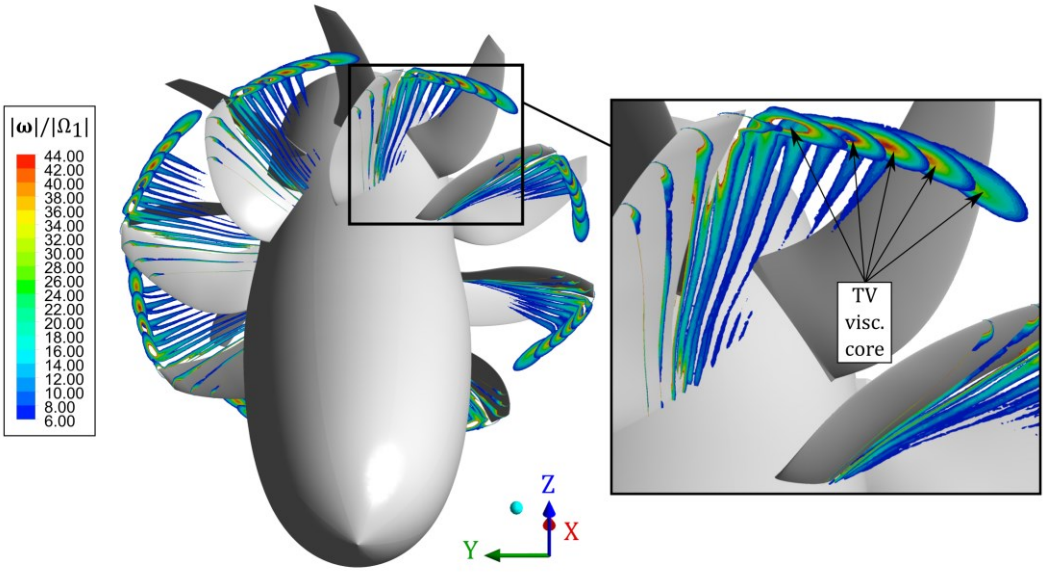

Figure 6.6 – Contours of normalized vorticity magnitude, $|\boldsymbol{\omega}|/|\Omega_1|$, extracted from the RANS solution at 9 planes normal to the rotation axis located from $X = 0$ to the MP.

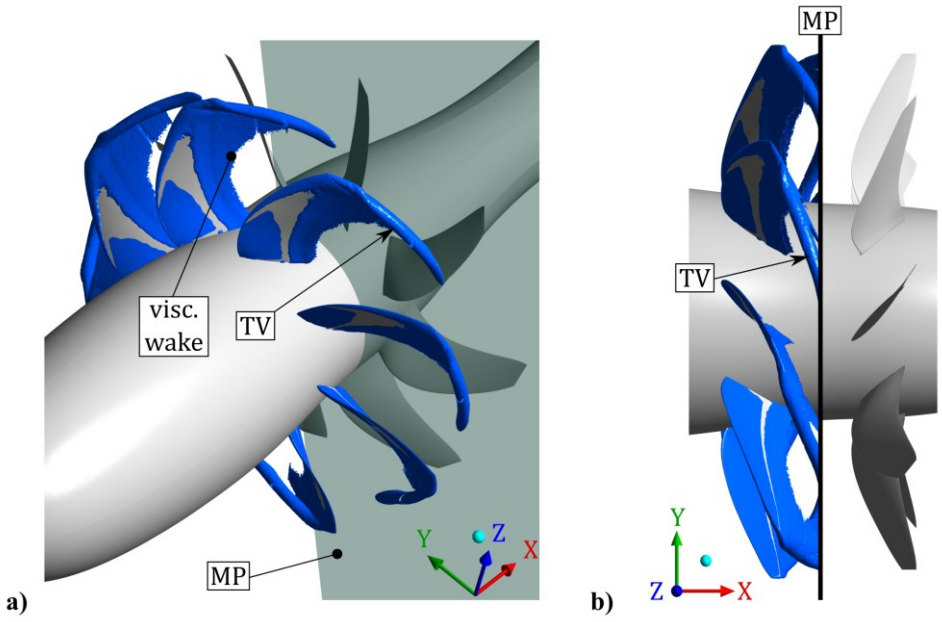

Figure 6.7 – Surfaces of constant vorticity $|\boldsymbol{\omega}|/|\Omega_1| = 10$ (blue surfaces) obtained from the RANS simulation in the computational domain of the FR. **a)** 3D view, **b)** projection onto (X, Y) plane.

6.1.3 URANS flow field

The absolute velocity and vorticity fields past the CROR blades, computed by means of the URANS simulation, are presented below. The reported results refer to 4 time instants, equally spaced within the time interval, Δt, taken by the rotors to span one mutual blade passage:

$$\Delta t = \frac{\Delta\Psi}{|\Omega_1| + |\Omega_2|} = \frac{2\pi}{B_1(|\Omega_1| + |\Omega_2|)} = \frac{2\pi}{B_2(|\Omega_1| + |\Omega_2|)} \ . \tag{6.5}$$

The first time instant, t_0, was chosen as the time when the front and rear blades are aligned, while the other time instants are $t_1 = t_0 + \Delta t/3$, $t_2 = t_0 + 2\Delta t/3$ and $t_3 = t_0 + \Delta t$.

The positions of the blades in the absolute frame of reference, (X_a, Y_a, Z_a), at the 4 time instants are depicted in Figure 6.8. Only two blades per rotor are shown for a clearer visualization. Consider the numbering $k_1 = 1 \ldots B_1$ and $k_2 = 1 \ldots B_2$ for the front and rear blades, respectively, where the values increase in the direction of rotation of each rotor. At time t_0, the pitch change

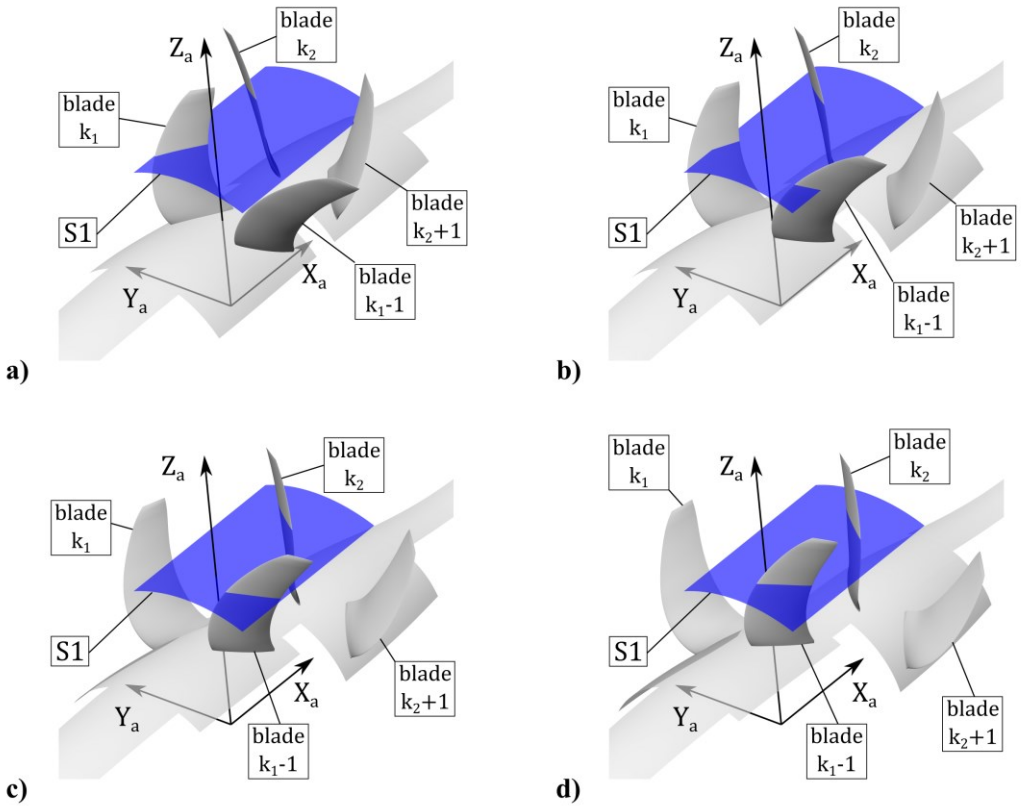

Figure 6.8 – Surface of constant radius $R/R_{T,1} = 0.75$ (S1) and relative positions of the FR and RR blades at 4 time instants: **a)** t_0 (FR and RR blades aligned), **b)** $t_1 = t_0 + \Delta t/3$, **c)** $t_2 = t_0 + 2\Delta t/3$, **d)** $t_3 = t_0 + \Delta t$ (FR and RR blades realigned).

axes of blades k_1 and k_2 are parallel, as well as the pitch change axes of blades $(k_1 - 1)$ and $(k_2 + 1)$, and so on (see Figure 6.8 a)). After time interval Δt, that is at time t_3, the blades of the FR and RR return to align. Therefore, at time t_3, the pitch change axes of blades $(k_1 - 1)$ and k_2 are parallel (see Figure 6.8 d)), as well as the pitch change axes of blades $(k_1 - 2)$ and $(k_2 + 1)$, and so on.

The velocity field shown hereafter was extracted from the URANS solution on the cylindrical surface S1 of radius $R_a/R_{T,1} = 0.75$ depicted in Figure 6.8. The azimuthal extension of S1 is limited to one blade passage, $\Delta\Psi = 45°$, with $\Psi_{a,min} = 90° - \Delta\Psi/2 = 67.5°$ and $\Psi_{a,max} = 90° + \Delta\Psi/2 = 112.5°$. Figure 6.8 shows the locations where surface S1 intersects the blades of the FR and RR at the 4 time instants considered.

The contours in Figure 6.9 illustrate the axial and tangential components of the absolute velocity on surface S1, from time t_0 (Figure 6.9 a)) to time t_3 (Figure 6.9 d)). In the figure, S1 is projected onto plane (X_a, Y_a). Recalling that only a single blade passage was simulated, v_X and v_Ψ from URANS are repeated circumferentially to show the solution on the whole surface S1 at each time. Note that the absolute velocity components in the cylindrical coordinate system (X_a, R_a, Ψ_a) are periodic in the azimuthal direction over S1 (e.g., $v_\Psi(X_a, R_a, \Psi_{a,min}, t) = v_\Psi(X_a, R_a, \Psi_{a,max}, t)$), as can be observed in Figure 6.9.

The URANS solution allows assessing the effects of the aerodynamic interaction of the two rotors. Figure 6.9 shows the influence of the azimuthal perturbations $\boldsymbol{v'}_{FR}$ and $\boldsymbol{v'}_{RR}$, generated by FR and RR, respectively (see Eq. (5.2)), on the velocity field. $\boldsymbol{v'}_{FR}$ and $\boldsymbol{v'}_{RR}$ are velocity perturbations in space that rotate with the front and rear blades, respectively. For instance, the velocity deficit due to the viscous wake shed by front blade k_1, which contributes to $\boldsymbol{v'}_{FR}$, is visible in Figure 6.9 a) (time t_0). The movement of this wake on surface S1 during the rotation of the blades can be observed by comparing Figures 6.9 from a) to d). The viscous wakes of the FR periodically impact the rear blades, leading to a periodic fluctuation of the velocity perceived by an observer rotating with the RR. Figure 6.9 shows that significant variations of v_X and v_Ψ occur close to the rear blade during the rotation, due to the impingement of $\boldsymbol{v'}_{FR}$. This causes significant fluctuations of the rear blade loading.

The perturbations $\boldsymbol{v'}_{RR}$ in the region upstream of the RR are due to the potential field of the rear blades, which decays very rapidly moving away from the rotor. It was found that $\boldsymbol{v'}_{RR}$ does not influence significantly the velocity field at the axial location of the front blades. In fact, the contours in Figure 6.9 show that v_X and v_Ψ for $X_a/R_{T,1} < 0.1$ are almost constant for an observer rotating with the front blades. Similar results were found along the entire span of the

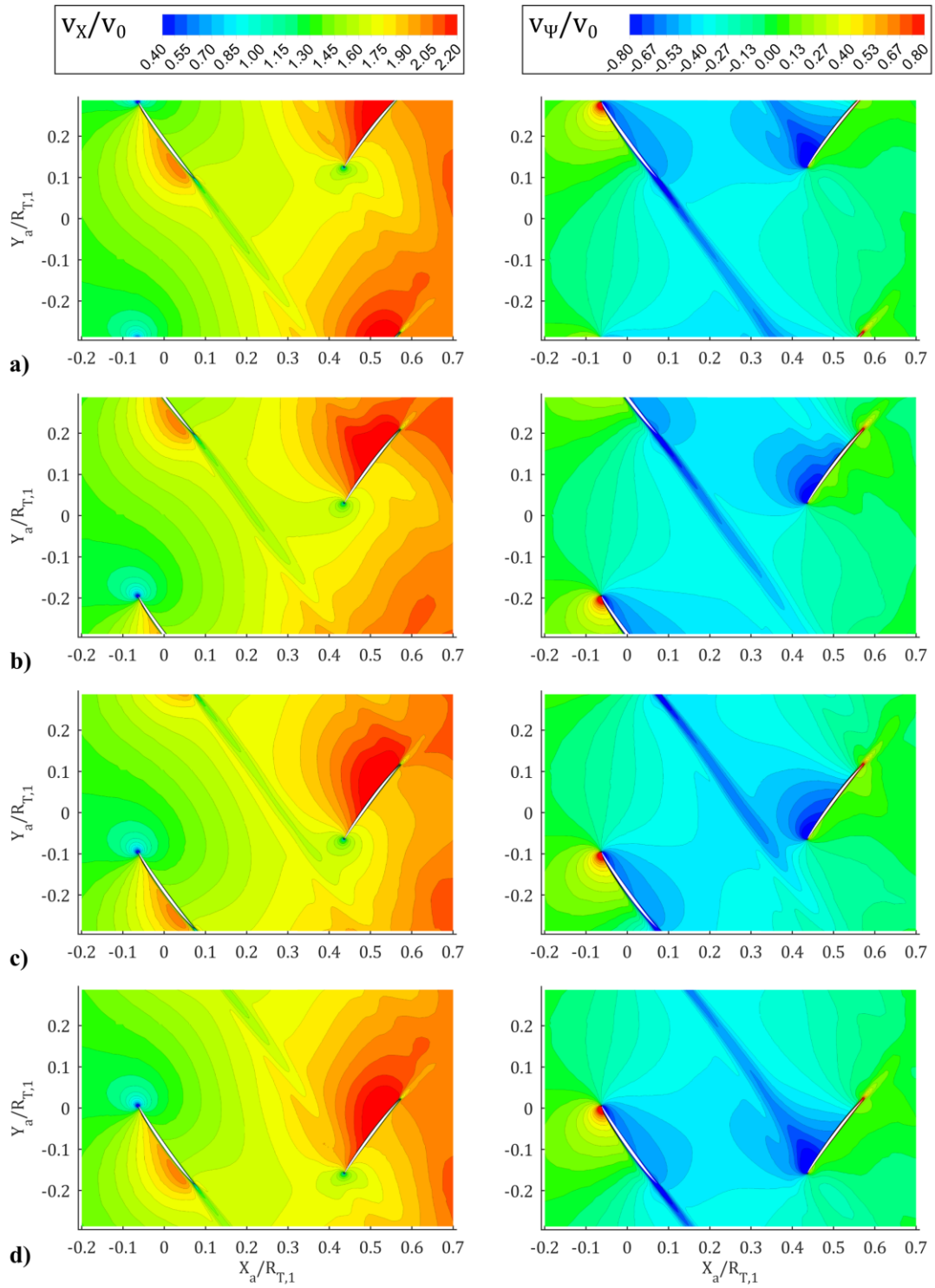

Figure 6.9 – Contours of axial velocity, v_X, and absolute tangential velocity, v_Ψ, extracted from the URANS solution on surface S1. Four time instants are considered: **a)** t_0 (FR and RR blades aligned), **b)** $t_1 = t_0 + \Delta t/3$, **c)** $t_2 = t_0 + 2\Delta t/3$, **d)** $t_3 = t_0 + \Delta t$ (FR and RR blades realigned).

front blade, also regarding the radial velocity component, v_R. Consequently, the amplitude of the unsteady loading on the front blades is negligible.

The absolute vorticity computed by means of the URANS simulation is shown in Figure 6.10, which illustrates the surfaces of constant vorticity magnitude $|\boldsymbol{\omega}|/|\Omega_1| = 10$ at time instants t_0, t_1, t_2 and t_3. The URANS solution for a single blade passage is repeated circumferentially to visualize the results over the full annulus. The TVs generated by the FR are identified by the tube-shaped surfaces where $|\boldsymbol{\omega}|/|\Omega_1| = 10$ (indicated by arrows in Figure 6.10 a)), which depart from the front blade tips. It is observed that the FR tip vortices are convected downstream through the RR. Also the TVs generated by the rear rotor blades can be identified in the figure (see the arrows labelled RR TV). Note that the vorticity is dissipated very rapidly moving downstream of the RR. This occurrence is mostly ascribed to the numerical dissipation. In fact, the computational grid was refined in the region between the two rotors, whereas it is coarse in the remainder of the computational domain (see Figure 3.4). Therefore, significant numerical viscosity is introduced downstream of the rear blades.

Figures 6.10 a)-d) show the phases of the impingement of the FR tip vortices on the rear blades. Since in the present test case the FR and RR have the same number of blades, all the blades of the rear rotor are hit by a TV released by the front rotor at the same time during the rotation. At time t_0 (Figure 6.10 a)), the rear blade is cutting the viscous core of the TV. The vorticity tube with $|\boldsymbol{\omega}|/|\Omega_1| = 10$, which identifies the shape of the TV core, is dissected by the blade and the portion that lies on the blade pressure side is visible in Figure 6.10 a).

At time t_1 (Figure 6.10 b)), the TV core has left the rear blade surface and is located between two consecutive blades of the RR. Figure 6.10 c) shows that at time t_2 the viscous core of the TV is impinging the leading edge of the rear blade. The radial coordinate of the impingement point is about $R_a/R_{T,2} = 0.91$. For $t > t_2$ the rear blade enters the region of the viscous core, thus repeating the cutting process of the tip vortex.

At time t_3 (Figure 6.10 d)), the mutual azimuthal position of front and rear blades is the same as at time t_0, and a period of the cyclic impact of the TV on the rear blade is then completed. Because of the periodic TV-blade impingement, an observer rotating with the RR perceives a periodic velocity fluctuation due to the passage of the strong azimuthal perturbations, $\boldsymbol{v}'_{TV}$, ascribed to the FR tip vortices (see Eqs. (5.2) and (5.3)). This produces unsteady loads of large amplitude on the rear blades close to the impingement radius.

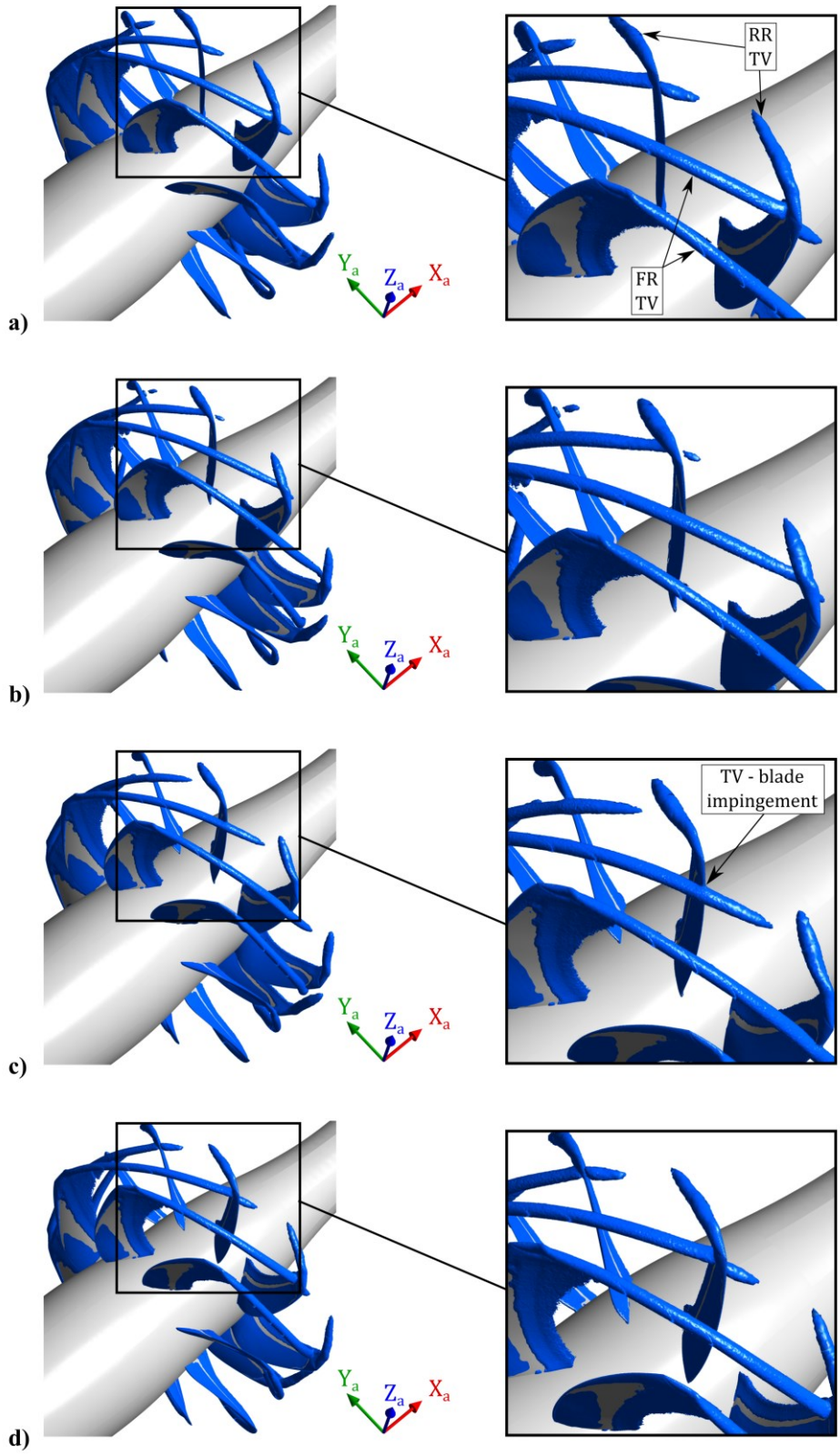

Figure 6.10 – Surfaces of constant vorticity $|\boldsymbol{\omega}|/|\Omega_1| = 10$ (blue surfaces) obtained from the URANS simulation. Four time instants are considered: **a)** t_0 (FR and RR blades aligned), **b)** $t_1 = t_0 + \Delta t/3$, **c)** $t_2 = t_0 + 2\Delta t/3$, **d)** $t_3 = t_0 + \Delta t$ (FR and RR blades realigned).

6.2 Extrapolated velocity perturbations

In the absolute reference frame (X_a, R_a, Ψ_a), the unsteady flow field approaching the rear rotor can be reconstructed by adding perturbations $\boldsymbol{v'}_{FR}$ (steady with respect to the FR) to RANS solution $\boldsymbol{v}_{RANS}$ (steady with respect to the RR) at corresponding azimuthal positions at any time instant. However, reconstructing the overall unsteadiness at the inlet of the rear rotor is not required because the unsteady loads on the RR are only due to the perturbations generated by the front rotor, $\boldsymbol{v'}_{FR}$.

To validate the perturbations extrapolated to the leading edge of the RR, $\boldsymbol{v'}_{FR}(X_{LE,2}, R, \Psi)$ is compared with the perturbations $\boldsymbol{v'}_{U-R}$ (subscript U – R means URANS – RANS) computed as:

$$\boldsymbol{v'}_{U-R}(X_{LE,2}, R, \Psi) = \langle \boldsymbol{v}_{URANS}(X_{LE,2}, R, \Psi, t) \rangle - \overline{\boldsymbol{v}}_{RANS}(X_{LE,2}, R, \Psi)\,, \tag{6.6}$$

where $\langle \cdot \rangle$ denotes time averaging. In Eq. (6.6), the absolute velocities are extracted in the coordinate system (X, R, Ψ) rotating with the FR. An observer fixed to the front rotor perceives variations in time of the URANS velocity field due to the relative motion of the perturbations in space generated by the rear rotor and fixed to it. Therefore, averaging in time $\boldsymbol{v}_{URANS}$ leads to the removal of such RR perturbations from the URANS solution. Finally, the URANS flow perturbations due to the front rotor are obtained by subtracting the azimuthally averaged RANS solution ($\overline{\boldsymbol{v}}_{RANS}$) from the time averaged URANS flow field.

The contours in Figure 6.11 are computed on the surface of revolution generated by the curve $X_{LE,2}(R)$ in the azimuthal range of a single blade passage. The angular sectors depicted in Figure 6.11 represent the projection of the surface of revolution onto plane (Y, Z). Figure 6.11 a) shows the normalized axial, tangential and radial components of $\boldsymbol{v'}_{U-R}$. The trace of the viscous wake is visible in the region from the hub to about $R/R_{T,2} = 0.85$, while the TVs emitted by the FR are mainly responsible for the complicated flow structures observed in the outer region.

It should be noted that the radial velocity component is not useful for the computation of the blade response, which is based on the assumption of 2D flow field. However, it is considered hereafter for a more complete representation and validation of the results of the extrapolation models.

Figures 6.11 b) to 6.11 e) show the velocity perturbations predicted by the different extrapolation models at the LE of the rear rotor, pointing out the influence of the 3D effects. The results in Figure 6.11 b) are obtained by means of the 2D extrapolation model, calibrated using the complete RANS solution, which includes also the TV effects. This means that the calibration of the model parameters is affected by the TV flow field. A comparison with $\boldsymbol{v'}_{U-R}$ (Figure 6.11

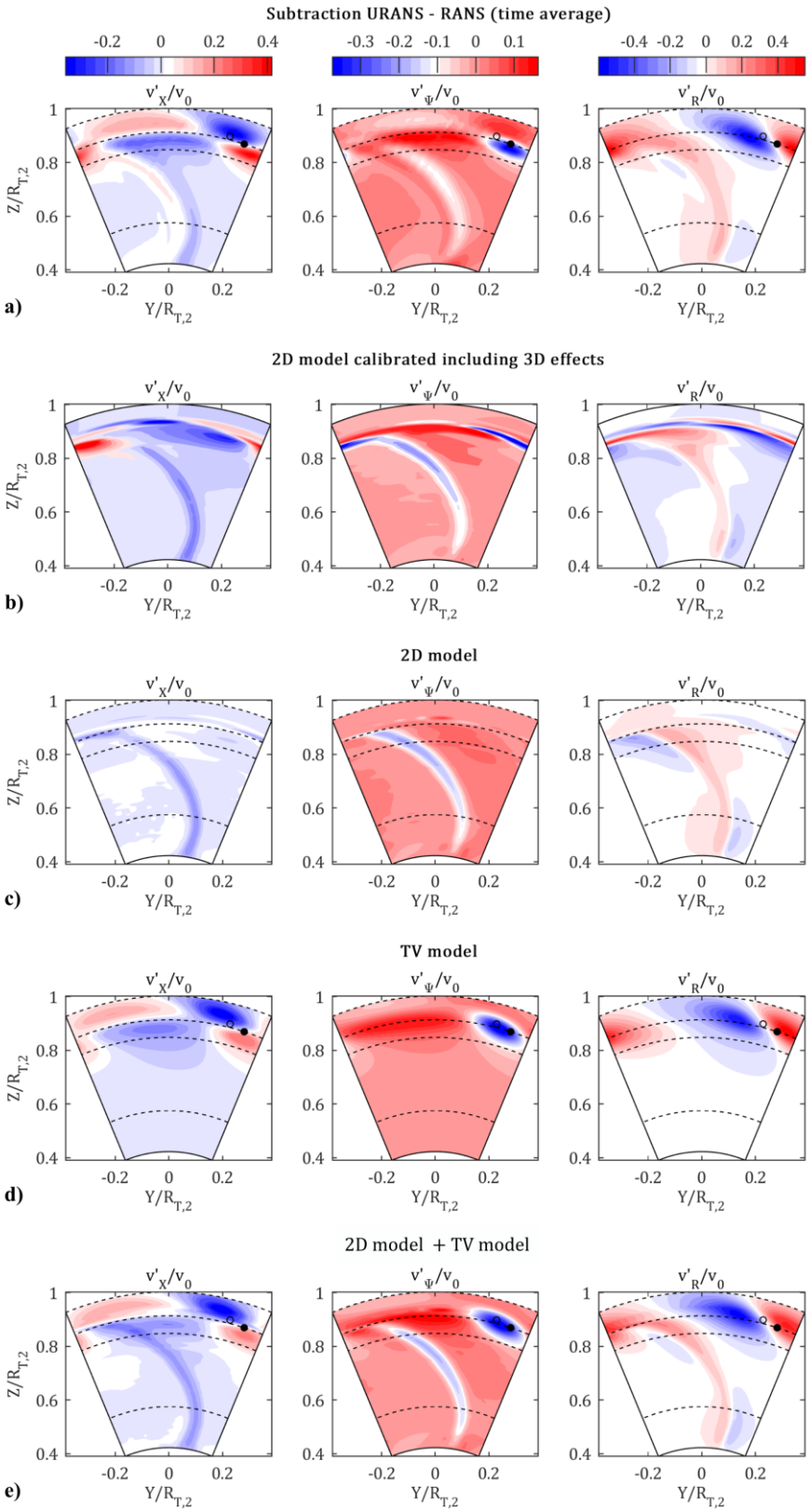

Figure 6.11 – Contours of velocity perturbations generated by the FR and computed at the rear rotor inlet (surface of revolution generated by the curve $X_{LE,2}(R)$). **a)** $\boldsymbol{v'}_{U-R}$ computed from URANS solution (see Eq. (6.6)), **b)** 2D model $\boldsymbol{u'}$ calibrated using $\boldsymbol{v'}_{RANS}$, **c)** 2D model $\boldsymbol{u'}$ calibrated using $\boldsymbol{v'}_{2D}$, **d)** TV model $\boldsymbol{u'}_{TV}$, **e)** $\boldsymbol{v'}_{FR} = \boldsymbol{u'}_{TV} + \boldsymbol{u'}$.

a)) shows that the general features of the perturbations produced by the FR are reproduced reasonably well in the inner region, up to about $R/R_{T,2} = 0.8$, whereas the reconstruction is very poor in the outer region.

The results of the 2D model, calibrated after removing the TV flow field from the RANS solution (see Eq. (5.27)), are depicted in Figure 6.11 c). In this case, the reconstructed unsteadiness is consistent with the effects of the viscous wake and potential field along the entire blade span. This indicates that the removal of the flow field ascribed to the TVs improves the result of the extrapolation of the essentially 2D flow structures.

The contribution of the TV model, $\boldsymbol{u'}_{TV}$, to the reconstructed perturbations is shown in Figure 6.11 d). The influence of the TV is limited to the outer part of the rear rotor and the perturbations are significantly stronger than the ones due to the wake and potential field (compare Figure 6.11 d) with Figure 6.11 c)). The general velocity distribution clearly resembles $\boldsymbol{v'}_{U-R}$ in the range $0.85 < R/R_{T,2} \leq 1$, even though a slight shift is observed in both radial and azimuthal directions. In the figure, the black solid and empty circles represent the points where the URANS (time averaged) and analytical TV trajectories, respectively, intersect the considered surface. The shift between these two points is a consequence of the misalignment of URANS and analytical TV trajectories close to the RR leading edge already discussed in Chapter 5.

The total unsteadiness $\boldsymbol{v'}_{FR} = \boldsymbol{u'}_{TV} + \boldsymbol{u'}$, reconstructed by adding the contributions of the TV and 2D models (calibrated after removing the three-dimensional effects), is shown in Figure 6.11 e). A good agreement with $\boldsymbol{v'}_{U-R}$ (Figure 6.11 a)) is observed along the entire blade span, and a remarkable improvement with respect to the merely 2D extrapolation (Figure 6.11 b)) is obtained in the outer flow region.

Figure 6.12 shows the velocity perturbations computed along the circumferential paths indicated by the dashed lines in Figure 6.11. The velocity profiles computed from the URANS solution, $\boldsymbol{v'}_{U-R}$, are indicated by solid black lines. The perturbation profiles extrapolated according to the 2D model and the TV model are indicated by dashed and dash-dotted black lines, respectively, while the overall reconstructed perturbations are represented by dotted red lines. Figure 6.12 a) refers to radial coordinate $R/R_{T,2} = 0.576$, where $\boldsymbol{u'}_{TV} \approx 0$, and the reconstruction relies only on the 2D model. A fairly good agreement with $\boldsymbol{v'}_{U-R}$ is found. The amplitude of the negative peaks, due to the viscous wake, is overpredicted for the axial and tangential components, but their azimuthal position is well reproduced. Similar results are found in the radial range from the hub to about $R/R_{T,2} = 0.75$.

Moving radially outward, the influence of $\boldsymbol{u'}_{TV}$ becomes increasingly important, and Figures 6.12 b) to 6.12 d) show that it is essential to obtain a satisfactory reconstruction of the flow unsteadiness. At $R/R_{T,2} = 0.848$ (Figure 6.12 b)), the 2D model predicts correctly the azimuthal

position of the wake (see the negative peaks of $\boldsymbol{v'}_{U-R}$ and $\boldsymbol{u'}$ at $B_2\Psi/2\pi = 2.16$ for the axial and tangential velocity components), and when adding the contribution of the TV model a good reproduction of $\boldsymbol{v'}_{U-R}$ is obtained over the whole azimuthal range.

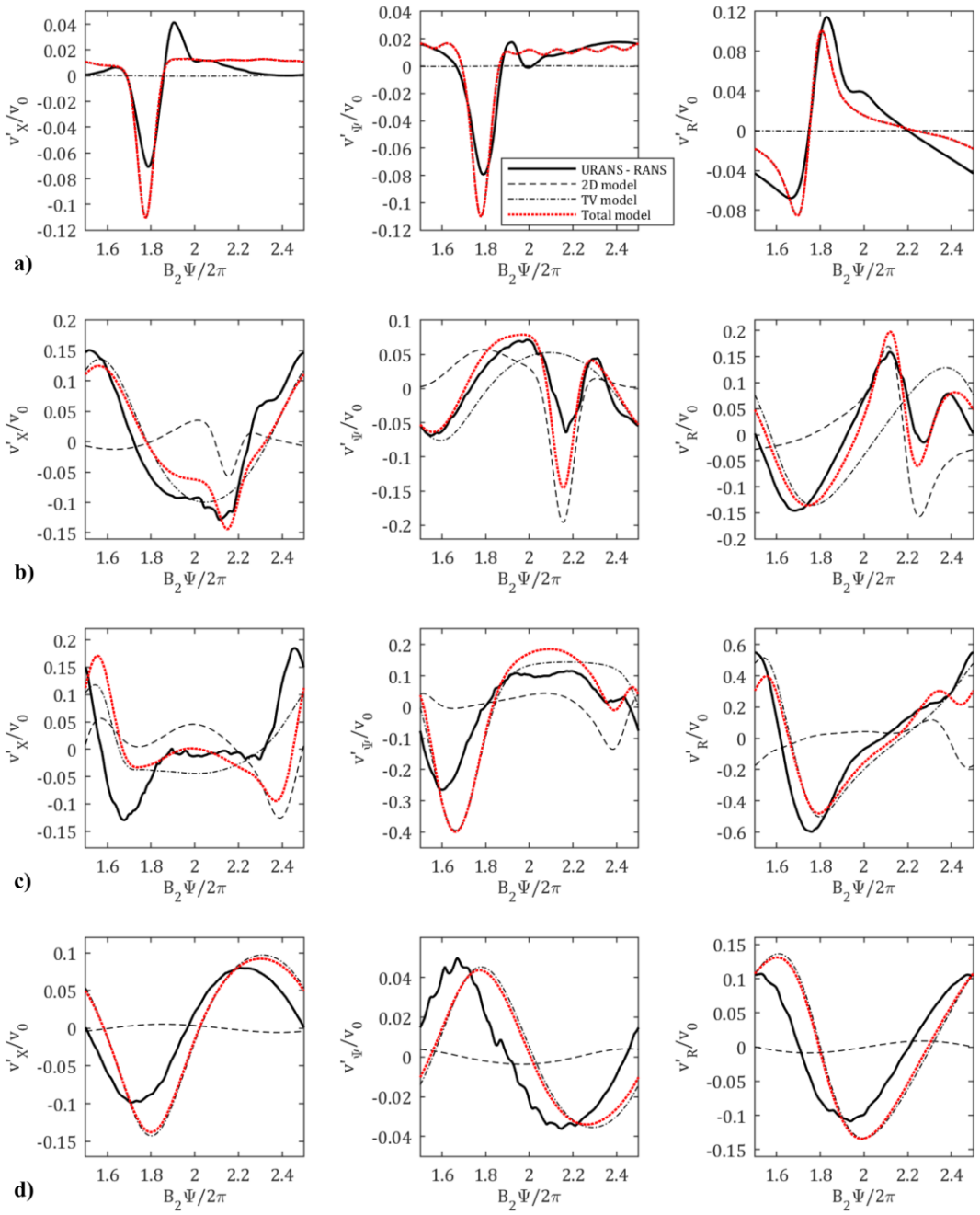

Figure 6.12 – Circumferential profiles of velocity perturbations generated by the FR and computed at the RR leading edge: $\boldsymbol{v'}_{U-R}$ (solid black lines), $\boldsymbol{u'}$ (dashed black lines), $\boldsymbol{u'}_{TV}$ (dash-dotted black lines) and $\boldsymbol{v'}_{FR}$ (dotted red lines). Profiles located at **a)** $R/R_{T,2} = 0.576$, **b)** $R/R_{T,2} = 0.848$, **c)** $R/R_{T,2} = 0.914$, **d)** $R/R_{T,2} = 1$.

The profiles in Figure 6.12 c) are located at $R/R_{T,2} = 0.914$, where the TV trajectory computed from URANS intersects the LE_2 surface. The differences between $\boldsymbol{v}'_{U-R}$ and the reconstructed velocities $\boldsymbol{v}'_{FR}$ are mainly due to the misalignment between URANS and analytical vortex trajectories. This is shown by the azimuthal shift of the positive peak of the axial velocity and the negative peak of the tangential velocity. Nevertheless, the main features of the $\boldsymbol{v}'_{U-R}$ profiles are reproduced fairly well.

Close to the blade tip (Figure 6.12 d)), the contribution of the viscous wake is not taken into account because the streamlines impacting the rear rotor originate over the FR tip (see Chapter 4), and the extrapolated potential field turns out to be very weak. The TV model leads to a good reproduction of the perturbation wave, even though the misalignment of the TV trajectory causes the observed azimuthal shift of the velocity profiles.

6.3 Unsteady loads on the rear rotor blade

To assess the impact of the error in the unsteadiness reconstruction on the computation of the blade loading, the lift and drag coefficients (Eqs. (4.14) and (4.15)) resulting from the blade response to $\boldsymbol{v}'_{FR}$ and $\boldsymbol{v}'_{U-R}$ have been compared. Furthermore, the blade response has been validated against C_{Lh_1} and C_{Dh_1} obtained by performing the DFT of the blade pressure distributions resulting from the URANS computation.

Figures 6.13 to 6.16 show the distributions of amplitude and phase of C_{Lh_1} and C_{Dh_1} along the RR blade span, up to harmonic order $h_1 = 4$. The blade responses to reconstructed ($\boldsymbol{v}'_{FR}$) and URANS ($\boldsymbol{v}'_{U-R}$) perturbations are indicated by dash-dotted red lines and dashed black lines, respectively. The former exhibits a larger amplitude along wide portions of the blade span, with a more pronounced overestimation for harmonic order $h_1 = 1$ (Figure 6.13). In the range from the hub radius to about $R/R_{T,2} = 0.8$, this is ascribed to an overestimation of the amplitude of the wake deficit (see Figure 6.12 a)). The differences at the outer radii, where the contribution of the TV model is stronger, are ascribed to the misalignment between extrapolated and URANS vortex trajectories and to the overestimation of the TV velocity deficit, $V_{x,def}$ (see Figure 5.15). Concerning the predicted phases, a good agreement is found along the whole blade span for $h_1 = 1$ and $h_1 = 2$. At the higher harmonic orders (Figs. 6.15 and 6.16), major differences are observed close to the blade tip ($R/R_{T,2} > 0.9$), and similar results were found for $h_1 > 4$. Despite the observed discrepancies in amplitude and phase, the general agreement between the responses to $\boldsymbol{v}'_{FR}$ and to $\boldsymbol{v}'_{U-R}$ can be considered satisfactory. In fact, as it will be shown in the following section, these deviations do not affect significantly the noise prediction.

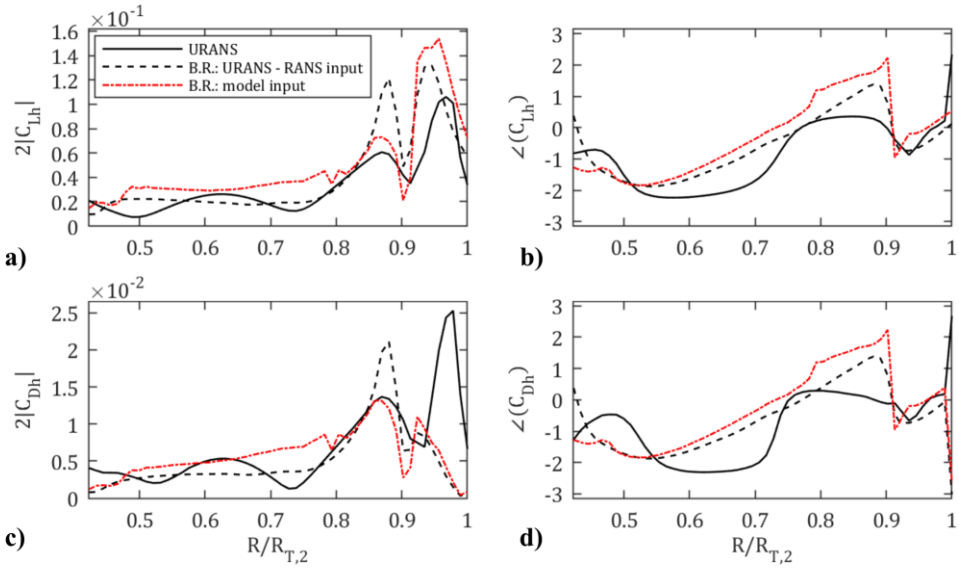

Figure 6.13 – Harmonic of the unsteady loading of order $h_1 = 1$.
Comparison among URANS results (black solid line), blade response to $\boldsymbol{v}'_{U-R}$ (dashed black line), and blade response to $\boldsymbol{v}'_{FR}$ (dash-dotted red line). **a)** Amplitude of C_{Lh_1}, **b)** Phase of C_{Lh_1}, **c)** Amplitude of C_{Dh_1}, **d)** Phase of C_{Dh_1}.

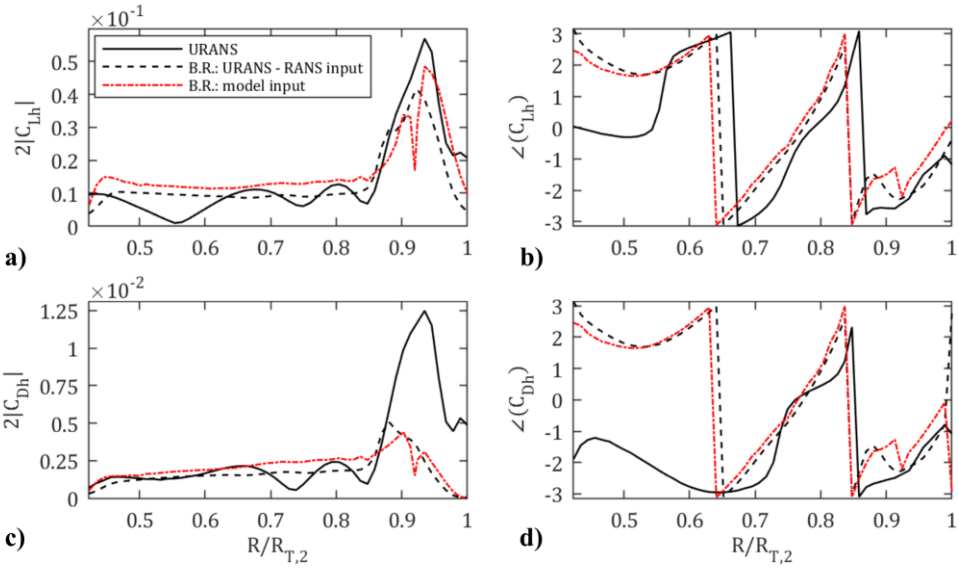

Figure 6.14 – Harmonic of the unsteady loading of order $h_1 = 2$.
Comparison among URANS results (black solid line), blade response to $\boldsymbol{v}'_{U-R}$ (dashed black line), and blade response to $\boldsymbol{v}'_{FR}$ (dash-dotted red line). **a)** Amplitude of C_{Lh_1}, **b)** Phase of C_{Lh_1}, **c)** Amplitude of C_{Dh_1}, **d)** Phase of C_{Dh_1}.

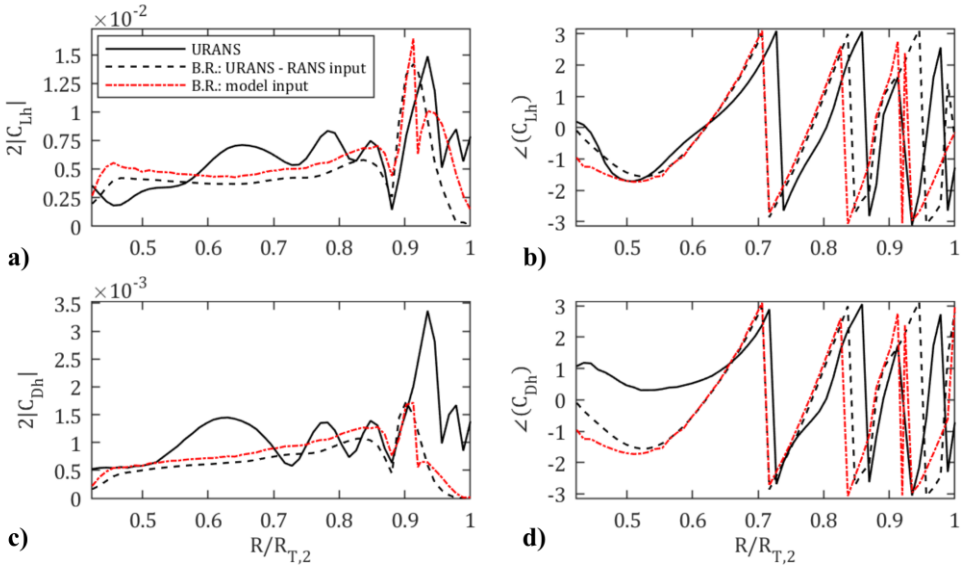

Figure 6.15 – Harmonic of the unsteady loading of order $h_1 = 3$.
Comparison among URANS results (black solid line), blade response to $\boldsymbol{v}'_{U-R}$ (dashed black line), and blade response to $\boldsymbol{v}'_{FR}$ (dash-dotted red line). **a)** Amplitude of C_{Lh_1}, **b)** Phase of C_{Lh_1}, **c)** Amplitude of C_{Dh_1}, **d)** Phase of C_{Dh_1}.

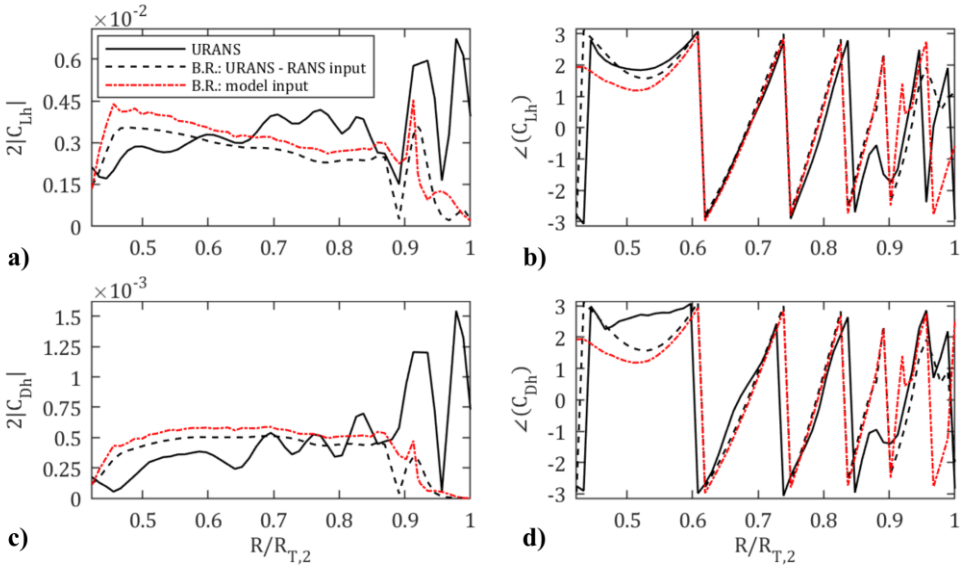

Figure 6.16 – Harmonic of the unsteady loading of order $h_1 = 4$.
Comparison among URANS results (black solid line), blade response to $\boldsymbol{v}'_{U-R}$ (dashed black line), and blade response to $\boldsymbol{v}'_{FR}$ (dash-dotted red line). **a)** Amplitude of C_{Lh_1}, **b)** Phase of C_{Lh_1}, **c)** Amplitude of C_{Dh_1}, **d)** Phase of C_{Dh_1}.

Amplitude and phase of lift and drag coefficients calculated from the URANS blade pressure are indicated by black solid lines in Figures 6.13 to 6.16. Note that the phases of C_{Lh_1} and C_{Dh_1} are quite similar to each other, except near the hub for $h_1 = 2$. The blade response to the reconstructed perturbations predicts reasonably well the trends of amplitude and phase of lift and drag for $R/R_{T,2} < 0.9$. The observed deviations between the blade response and URANS pressure results are partially ascribed to some inaccuracy in the reconstruction of the velocity perturbations. However, the major contribution to the prediction error is ascribed to the blade response model, especially close to the blade tip. In fact, span-end effects at the tip of the rear blades, which are not considered in the present blade response model, modify the lift and drag distributions close to the tip [45]. Moreover, the angle of attack of the mean flow for $0.9 < R/R_{T,2} \leq 1$ ranges from 7.4° to 14.1°, in contrast with the small angle of attacks assumed by the present blade response model. The comparison with the loads extracted from URANS highlights some limitations of the blade response model implemented in the present work, suggesting that more sophisticated models could be used.

6.4 Interaction noise estimation

The IN tones emitted by the rear rotor at frequencies $f = |h_1 BPF_1 + h_2 BPF_2|$ were computed by means of the Hanson model. The results are presented in terms of sound pressure level (SPL) directivity along a sideline parallel to the CROR axis and located at 4.514 RR tip radii from it.

The SPL is defined as:

$$SPL(\varrho, \varphi, f) = 20\log_{10}\left[\frac{\tilde{A}_p(\varrho, \varphi, f)}{p_{ref}}\right], \tag{6.7}$$

where $\tilde{A}_p(\varrho, \varphi, f)$ is the root mean square value of the harmonic amplitude, computed by Eq. (4.12), and $p_{ref} = 20\ \mu Pa$ is the reference pressure. For a more compact notation, a frequency of order h_1 and h_2 of the rotor $BPFs$ is denoted as $\{h_1, h_2\}$.

Results up to orders 2 and 3 of BPF_1 and BPF_2 are reported in Figure 6.17 and Figure 6.18, respectively. The noise emissions due to the 2D model perturbations (dash-dotted black line), $\boldsymbol{u}'$, calibrated after removing the three-dimensional effects, and to the overall perturbations $\boldsymbol{v}'_{FR}$ (red solid line) were computed separately to assess the influence of the tip vortices.

First, a comparison with the noise emissions produced by the URANS perturbations (dashed black lines), $\boldsymbol{v}'_{U-R}$, is addressed. This allows evaluating the impact of the accuracy in the

unsteadiness reconstruction on the IN estimation. When only the contribution of $\boldsymbol{u}'$ is considered, the magnitude of the SPL is considerably underestimated at most frequencies in wide angular ranges. For example, a difference of about 20 dB is observed for $20° < \varphi < 45°$ and $135° < \varphi < 160°$ at frequency $\{2,1\}$ (see Figure 6.17), and an underestimation from 5 dB to 30 dB results along the entire sideline at frequencies $\{1,3\}$ and $\{3,1\}$ (see Figure 6.18). Moreover, the shape of the SPL directivity predicted using perturbations $\boldsymbol{u}'$ exhibits strong deviations from the one resulting from $\boldsymbol{v}'_{U-R}$ along wide portions of the sideline, at all frequencies.

By adding the contribution of the TV model, both magnitude and shape of the SPL directivity are recovered very well, resulting in a good agreement with the IN generated by the URANS perturbations. At the lower frequencies (Figure 6.17), the shape of the directivity is reproduced almost perfectly. At frequencies $\{1,1\}$ and $\{1,2\}$ the only significant differences in the SPL amplitude observed for some negative peaks, while at $\{2,1\}$ a deviation of about 3 dB is found in the angular range $75° < \varphi < 110°$. Regarding the higher frequencies (Figure 6.18), the most significant differences in the shape of the directivity are limited to ranges $130° < \varphi < 140°$ and to $40° < \varphi < 49°$ for $\{2,3\}$ and $\{3,2\}$, respectively. Similar results were found for $h_1, h_2 > 3$. Assuming that the present TV model is reasonably founded and recognizing that the perturbations

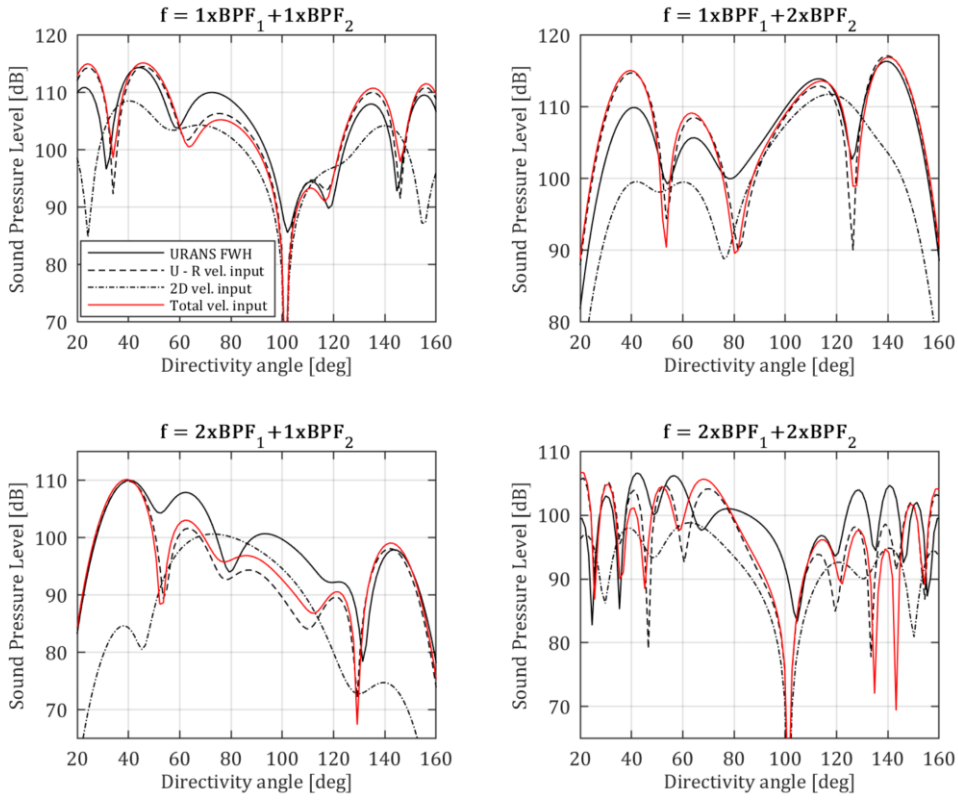

Figure 6.17 – Interaction noise up to harmonic order $h_1, h_2 = 2$ of the rotor $BPFs$.

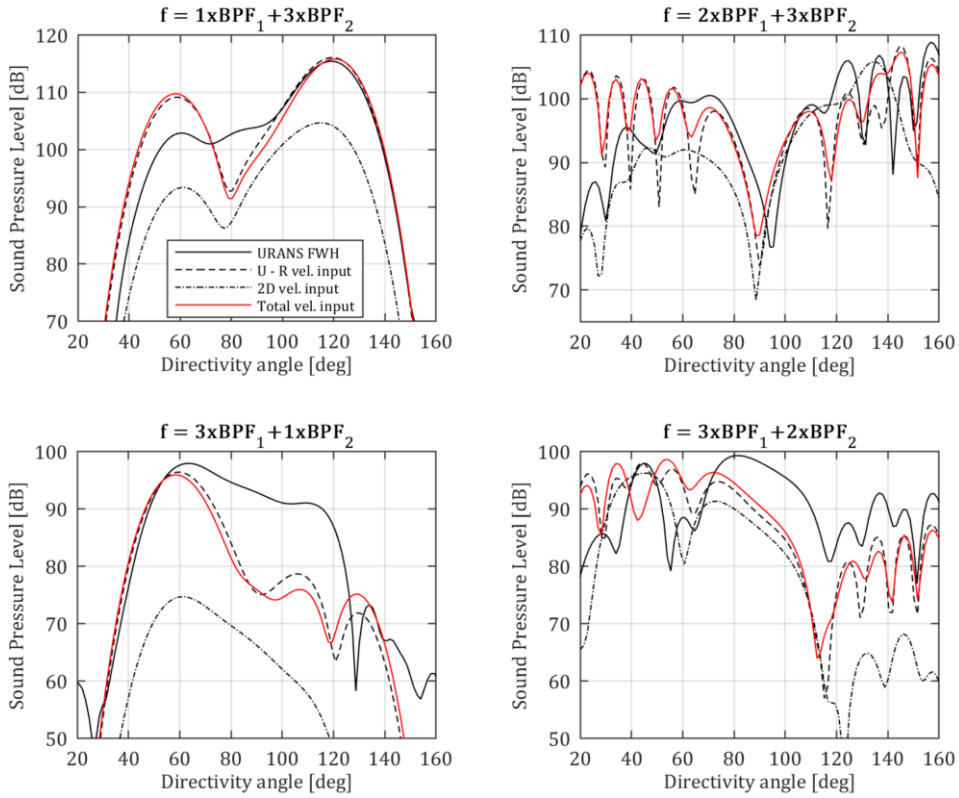

Figure 6.18 – Interaction noise up to harmonic order $h_1, h_2 = 3$ of the rotor $BPFs$.

due to the tip vortices largely influence the flow field, these comparisons show that including the effects of the front rotor TVs leads to a more consistent estimation of the IN.

The IN emission evaluated by means of the present model (accounting for the total perturbations $\boldsymbol{v'}_{FR}$) is validated against high fidelity FWH results (solid black lines in Figure 6.17 and Figure 6.18), obtained by means of a dedicated tool available in ANSYS Fluent. At the lower frequencies (Figure 6.17), a fairly good agreement is obtained, especially for {1,1}, {1,2} and {2,1}, where the maximum differences are limited to about 5 dB along most of the sideline. This indicates that the present model is able to reproduce properly the main flow features responsible for the IN emission.

At higher frequencies (Figure 6.18), larger discrepancies are observed. Since the harmonics of the noise emitted at higher frequencies are characterized by a shorter wavelength, the noise emission is very sensitive to the mutal phases of the sources distributed along the blade span. Therefore, even small errors in the phases of the blade loads predicted by the blade response model can lead to a significantly inaccurate noise estimation. However, predicted and FWH noise directivities agree reasonably within some angular intervals.

Since the noise estimations resulting from $\boldsymbol{v'}_{U-R}$ and $\boldsymbol{v'}_{FR}$ are very similar, the limitations of the blade response model are considered the main responsible for the differences between the present predictions and the FWH results. Moreover, the propagation model proposed by Hanson does not account for the contribution of radial dipoles (see Appendix C). This could explain the underestimation of the SPL generally observed in the angular range close to the propeller plane (see [41]).

Figure 6.19 and Figure 6.20 show a comparison between the noise emissions due to the 2D model perturbations (dashed black line), $\boldsymbol{u'}$, calibrated without removing the three-dimensional effects, and to the overall perturbations (solid red line), $\boldsymbol{v'}_{FR}$. The acoustic emissions resulting from the URANS velocity perturbations (solid black line), $\boldsymbol{v'}_{U-R}$, are taken as reference for the validation. This comparison allows assessing the benefits produced by a proper modelling of the tip vortices instead of mimicking their effects by means of the 2D extrapolation model.

Results up to harmonic orders 2 and 3 of BPF_1 and BPF_2 are reported in Figure 6.19 and Figure 6.20, respectively. For some frequencies, the accuracies of the 2D model and the present model are comparable. For instance, for frequency $\{1,1\}$ (see Figure 6.19), the purely 2D model

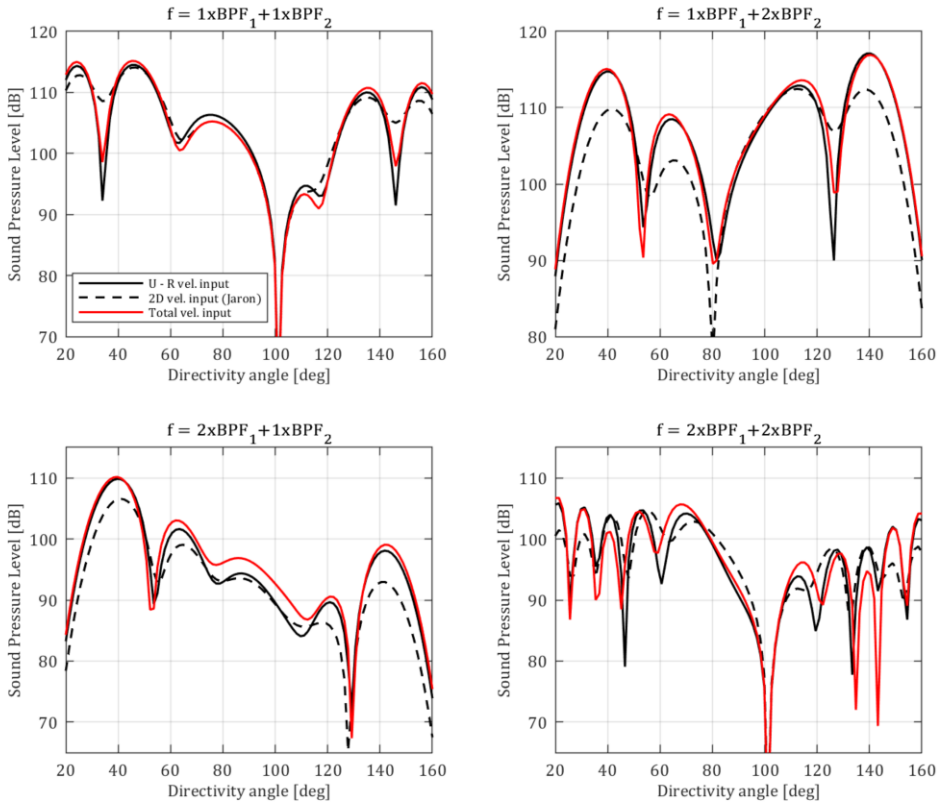

Figure 6.19 – Interaction noise up to harmonic order $h_1, h_2 = 2$ of the rotor $BPFs$. Comparison between the SPLs generated by $\boldsymbol{v'}_{U-R}$ (solid black line), $\boldsymbol{u'}$ calibrated without removing three-dimensional effects (dashed black line), and $\boldsymbol{v'}_{FR}$ (solid red line).

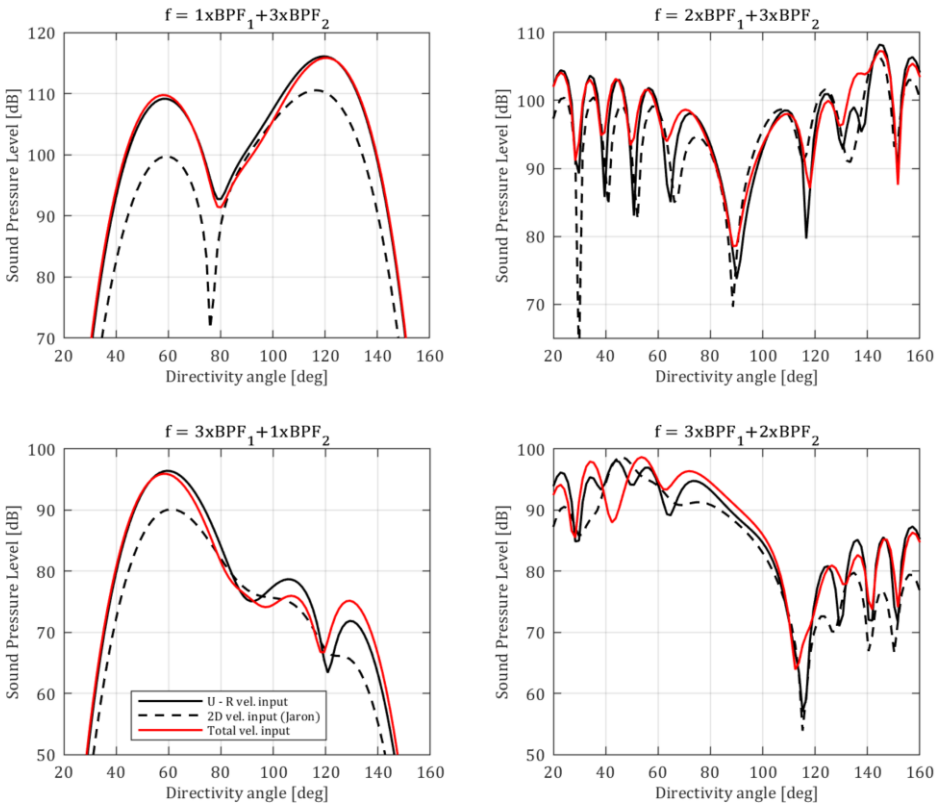

Figure 6.20 – Interaction noise up to harmonic order $h_1, h_2 = 3$ of the rotor $BPFs$. Comparison between the SPLs generated by $\boldsymbol{v}'_{U-R}$ (solid black line), $\boldsymbol{u}'$ calibrated without removing three-dimensional effects (dashed black line), and $\boldsymbol{v}'_{FR}$ (solid red line).

is particularly inaccurate within limited angular intervals, that is, near the negative SPL peaks at $\varphi = 34°$ and $\varphi = 146°$, which are better reproduced by the present model. Also for frequencies $\{2,2\}$ (Figure 6.19) and $\{2,3\}$ (Figure 6.20) the directivity shapes are similar, even though for the latter frequency a better match with the positive SPL peaks of the reference IN emission is obtained by means of the present model.

The comparable accuracy in the predictions of the IN tones for some frequencies is due to the fact that the 2D model, calibrated without removing the three-dimensional effects, partially ascribes the velocity perturbations generated by the TV to the viscous wake contribution (see Chapter 5). Therefore, the influence of the tip vortices to the reconstructed perturbations is partially included, even if in an inappropriate way. In fact, for many other frequencies, a remarkable improvement in the accuracy of the IN predictions is obtained by means of the present model.

For frequencies $\{1,2\}$ (Figure 6.19) and $\{1,3\}$ (Figure 6.20) the purely 2D model underestimates the magnitude of the SPL of about 10 dB along wide portions of the sideline. For frequency $\{2,1\}$, the predictions of the present model agree very well with the reference noise

emissions, while the 2D model underestimates the SPL of about 3 dB and 5 dB in the angular intervals $20 < \varphi < 65$ and $115 < \varphi < 160$, respectively. Accurate predictions are obtained by including properly the TV influence also for frequencies $\{3,1\}$ and $\{3,2\}$ (Figure 6.20). Similar results were found for $h_1, h_2 > 3$.

These results show that more accurate predictions of the IN tones can be obtained by means of a proper modelling of the influence of the tip vortices, as done by the present RANS-informed model.

6.5 Comparison with noise measurements

For completeness, the IN tones predicted by means of the present RANS-informed model are compared with noise measurements found in the literature, which refer to the benchmark experiment conducted in the 9- by 15- Anechoic Wind Tunnel at NASA Lewis Research Center [50]. The acoustic signal was measured along a sideline parallel to the CROR axis and located at 4.514 RR tip radii from it. The results are presented in terms of SPL directivity along this sideline.

Figures 6.21 a) to 6.21 c) show the SPL directivities at frequencies $\{1,1\}$, $\{1,2\}$ and $\{2,1\}$. The results of the wind tunnel measurements are indicated by solid black lines, while the SPLs predicted by the present RANS-informed model are depicted by solid red lines. For frequency $\{1,1\}$ (Figure 6.21 a)), a reasonable agreement is observed between the measured and estimated SPL directivities for angular ranges $40 < \varphi < 90$ and $125 < \varphi < 150$, while larger discrepancies are obtained for $90 < \varphi < 125$.

For frequency $\{1,2\}$ (Figure 6.21 b)), the measured SPL is predicted fairly well within the limited angular interval $135 < \varphi < 150$, while larger inaccuracies are found for the remaining portion of the sideline.

The measured SPL is underpredicted by the present model along the whole sideline for frequency $\{2,1\}$ (Figure 6.21 c)). However, the trend of the SPL directivity is predicted reasonably well in the angular intervals $40 < \varphi < 75$ and $110 < \varphi < 130$.

Although some features of the SPL directivity are estimated reasonably well, these comparisons show some inaccuracies in the prediction of the wind tunnel noise measurements using the present RANS-informed model. However, it is found that also the SPL computed by means of the high fidelity FWH analogy, depicted by dashed black lines in Figure 6.21, exhibits relevant inaccuracies in the prediction of the noise measurements along wide portions of the sideline. Indeed, significant improvements with respect to the present model are obtained only within the angular ranges $60 < \varphi < 80$ for frequency $\{1,1\}$ (Figure 6.21 a)) and $60 < \varphi < 75$ for frequency $\{2,1\}$ (Figure 6.21 c)).

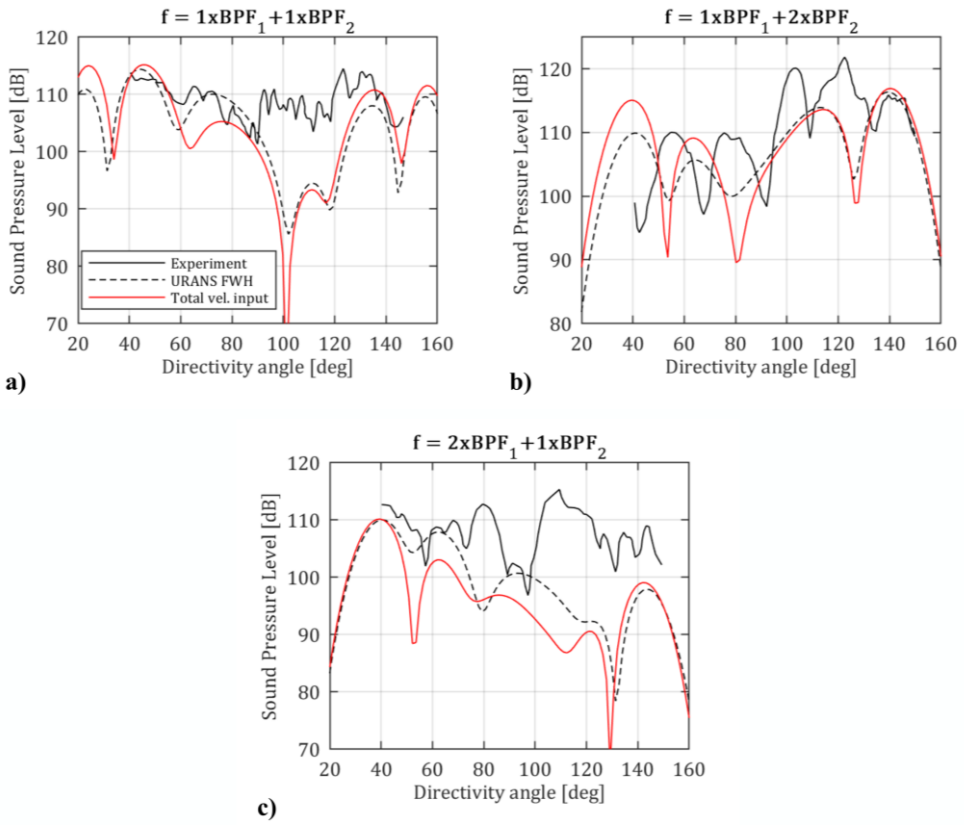

Figure 6.21 – Comparison between the SPLs obtained from wind tunnel measurements [50] (solid black line), predicted by the FWH analogy (dashed black line), and estimated by the present RANS-informed model (solid red line). Interaction noise tones at frequency **a)** $f = 1 \times BPF_1 + 1 \times BPF_2$, **b)** $f = 1 \times BPF_1 + 2 \times BPF_2$, **c)** $f = 2 \times BPF_1 + 1 \times BPF_2$.

Both the RANS-informed and URANS-FWH approaches are not capable of providing a highly accurate prediction of the IN tones measurements. This is due to the differences that certainly exist between the simulated and the actual flow field past the CROR in the wind tunnel facility. In fact, the flow field in the wind tunnel experiment is affected by complicated phenomena which are not considered in the present CFD simulations, such as ground and wall effects. Moreover, the reproduced geometries of the FR and RR blades are slightly different from the actual ones (see Chapter 2).

Also the broadband noise, which is not accounted for in the present work, may contribute significantly to the measured IN tones emitted by the CROR scaled model. Moreover, it should be noted that the contribution of the FR blades to the noise emission is not considered in the present work. Even though the acoustic pressure disturbances generated by the front blades have a smaller impact on the IN tones in comparison with the ones due to the rear blades, their influence may not be totally negligible. Therefore, the results reported in Figure 6.21 suggest that the

proposed RANS-informed model can be further improved by considering the contribution of the broadband noise and the front blades to the interaction noise emission.

7 CONCLUSIONS

The work carried out in this Ph.D thesis consists in the development of an improved RANS-informed model for the fast prediction of the noise emitted by CRORs including the effect of the blade tip vortex. The focus is on the estimation of the interaction noise tones emitted by the rear rotor, arising from the interaction with the flow perturbations generated by the front rotor. The RANS-informed model proposed by Jaron et al., based on 2D flow assumptions, is considered as the basis for further improvements. This 2D analytical model, calibrated using data extracted from RANS solutions, allows extrapolating the azimuthal perturbations of flow velocity generated by the FR beyond the mixing plane, up to the leading edge of the rear rotor. Then, the unsteady loads on the rear blades are computed by means of a blade response function and the IN emission is calculated through an analytical noise propagation model in the frequency domain. In the present work the 2D blade response model proposed by Goldstein and the noise propagation model by Hanson have been used.

A novel tip vortex model has been developed to properly account for the contribution to the IN emission of the FR tip vortices impacting the rear blades. The semi-analytical TV model is genuinely 3D and is calibrated using data extracted from RANS solutions. The model allows extrapolating the velocity perturbations due to the front blade tip vortices beyond the MP.

The CROR geometry UDF F7/A7 was taken as the reference test case. Realistic shapes of the blades and nacelle were reproduced based on data found in the literature.

RANS and URANS simulations of the flow field around the CROR were performed using commercial software ANSYS Fluent. Data extracted from the RANS simulation, conducted introducing the mixing plane boundary condition, were used for the calibration of the TV model and 2D extrapolation model. The results of the URANS simulation were used to validate the proposed RANS-informed model. The CROR operating condition considered is representative of take-off. The benchmark for the validation of the numerical simulations is an experiment conducted in the 9- by 15- Anechoic Wind Tunnel at NASA Lewis Research Center. Even though the reproduced and actual geometries of the CROR are slightly different, the small errors obtained in the predicted thrust and net efficiency are considered as an indication that the main features of the computed and real flow fields are very similar.

The proposed tip vortex model consists in a semi-analytical representation of the vortex trajectory and the absolute velocity field generated by a single TV released by the FR blade. The

velocity field is given by the superposition of the induced velocities, computed by means of the Biot-Savart law, and the wake-like velocity deficit, locally aligned with the vortex trajectory.

The path of the vortex centre is modelled as a helix having variable pitch and radius to account for flow acceleration and stream-tube contraction. The analytical path is calibrated by fitting the vortex trajectory extracted from the RANS solution in the region between the FR trailing edge and the MP. The path extrapolated beyond the MP agrees well with the vortex trajectory extracted from the URANS solution, with a slight misalignment observed at the location of the vortex impingement on the RR leading edge. This supports the assumption of a helical trajectory with variable pitch and radius.

A novel calibration procedure is proposed to identify the parameters of the TV velocity model. The procedure is based on the fitting of the absolute vorticity extracted from the RANS solution in specific regions close to the tip vortex trajectory. In this way, the contribution of a single tip vortex can be singled out from the RANS flow field, leading to a proper calibration of the model. To do so, a model describing the local vorticity distribution has been developed. The results of the fitting show that the analytical vorticity distribution reproduces well the local vorticity extracted from the RANS solution, thus providing physically consistent values of the velocity parameters.

The effect of the diffusion and the ingestion of vorticity in the viscous core of the tip vortex are also modelled by means of empirical laws, which are used to fit the evolution of the velocity parameters along the vortex helix. It is found that the fitted distributions represent well the axial evolution of the velocity parameters in the region between the FR trailing edge and the MP.

After calibrating the model parameters, the absolute velocity field due to a single TV is evaluated at any point in the system of coordinates fixed to the FR. The velocity field generated by all the tip vortices released by the FR blades is evaluated by superimposing the single contributions.

The velocity perturbations in space, that is, in the azimuthal direction, due to the FR tip vortices are subtracted from the RANS velocity field in the region between the FR trailing edge and the MP to remove the three-dimensional effects. It was found that the removal of the TV perturbations improves the fitting of the 2D model at the outer radial coordinates, where the tip vortices have a stronger influence, leading to a more physically consistent extrapolation of the viscous wake and potential field contributions along the entire span on the rear blade.

The velocity perturbations computed by means of the TV model and 2D model are added at the LE of the rear rotor to obtain the complete reconstruction of the flow unsteadiness due to tip vortices, viscous wakes and potential field. The reconstructed velocity perturbations have been validated by comparison with the perturbations extracted from the URANS solution. A

remarkable improvement is obtained with respect to the merely 2D extrapolation in the outer flow region, where the influence of the tip vortices is stronger.

Both reconstructed and URANS velocity perturbations have been used as an input to the blade response model to assess the impact of the errors in the unsteadiness reconstruction on the computed unsteady loading. The general trends of both amplitude and phase of the load coefficients of the two responses agree fairly well, especially for high harmonic orders. Some discrepancies are observed at the lower frequency, due to some inaccuracy in the velocity reconstruction. However, it is found that these deviations do not affect significantly the noise prediction.

The response to the reconstructed flow perturbations has also been compared with the loading obtained from the DFT of the blade pressure distributions resulting from the URANS computation. Fairly large errors are found in the prediction of both amplitude and phase of the lift and drag coefficients, especially in the blade tip region. This is ascribed to the limitations of the implemented blade response model, which is based on 2D flow assumptions.

The noise emission has been computed along a sideline parallel to the CROR axis. The blade response model and the Hanson's noise propagation model has been used to compute the noise generated by both reconstructed and URANS velocity perturbations. The latter are used as a reference for a first validation of the noise estimated by means of the RANS-informed model. It is found that considering the contribution of the tip vortices leads to a very good agreement of the predicted IN tones with the reference noise emission, which is an indication of the quality of the unsteadiness reconstruction.

The IN emission evaluated by means of the present RANS-informed model has finally been validated against high fidelity FWH results. The observed prediction errors are mainly ascribed to the limitations of the blade response model and to the fact that the Hanson's acoustic model does not account for the contribution of radial dipoles. However, the comparison with the noise generated by URANS perturbations indicates that the proposed RANS-informed method, based on the introduction of the TV model, leads to physically consistent results, significantly improving the capabilities of the 2D model from literature.

Further developments of the present work should include the implementation of a more refined blade response model and an acoustic propagation model that accounts for the contribution of radial dipoles.

The IN tones predicted by means of both the proposed RANS-informed model and the URANS-FWH approach have been compared with wind tunnel noise measurements found in the literature. Both the prediction approaches show some inaccuracies in the estimation of the noise measurements. This result suggests that the present RANS-informed model can be further

improved by accounting for the contribution of the broadband noise and the front blades to the interaction noise emission.

Finally, it is pointed out that the computation of CROR noise performed using the present RANS-informed approach requires about 20 hours of computing time on a 32-core computer, whereas the noise estimation by means of URANS coupled with FWH takes roughly 3 months with the same CPU resources. Therefore, the proposed model shows the potential to be successfully embedded into a multidisciplinary design strategy of CROR that includes acoustic targets.

Appendix A DERIVATION OF THE 2D EXTRAPOLATION MODEL

The RANS-informed model proposed by Jaron et al. [42] allows modelling the azimuthal perturbations of velocity, $\boldsymbol{v}'_{FR}$, generated by the front rotor. The model is based on the hypothesis of 2D flow and assumes that $\boldsymbol{v}'_{FR}$ is due to the contributions of the viscous wake and bound potential field. The circumferential profile of the velocity perturbations is decomposed into harmonics, considering different distributions for the wake and potential flow contributions. The model is valid for any velocity component in the cylindrical coordinate system (X, R, Ψ) of the FR reference frame [43], and the generic velocity perturbation, u', is expressed as a Fourier series:

$$u'(X,\Psi) = u'_w(X,\Psi) + u'_p(X,\Psi) = 2 \cdot Re\left\{\sum_{h=1}^{+\infty}\left[u_w(X,h) + u_p(X,h)\right]e^{ihB_1\Psi}\right\}, \quad \text{(A.1)}$$

where Fourier coefficients $u_w(X,h)$ and $u_p(X,h)$ represent the contributions of the viscous wake and potential field, respectively. The derivation of $u_w(X,h)$ and $u_p(X,h)$ is presented below, highlighting some important aspects of the model.

A.1 Contribution of the viscous wake

The viscous wake is modelled by a Gaussian distribution, modified to account for an asymmetric velocity deficit between the blade pressure and suction sides, typical of lifting airfoils [52]. A classic Gaussian distribution is characterized by the same phase for all harmonics. Therefore, the Gaussian model for the amplitude of the harmonics is maintained, while the zero-phase property is relaxed by introducing a different phase for each harmonic [42]. This allows reproducing circumferential periodic perturbations that are asymmetric about the wake centreline.

Consider a cylindrical section of the reference blade of the FR, as shown in Figure A.1. The cylindrical coordinate system $\left(\tilde{X}, R, \tilde{\Psi}\right)$ fixed to the rotor is defined so as the coordinates $\tilde{X} = 0$ and $\tilde{\Psi} = 0$ are located at the trailing edge of the considered blade section (see Figure A.1). The contribution of the wake to the velocity perturbations is given by the equation:

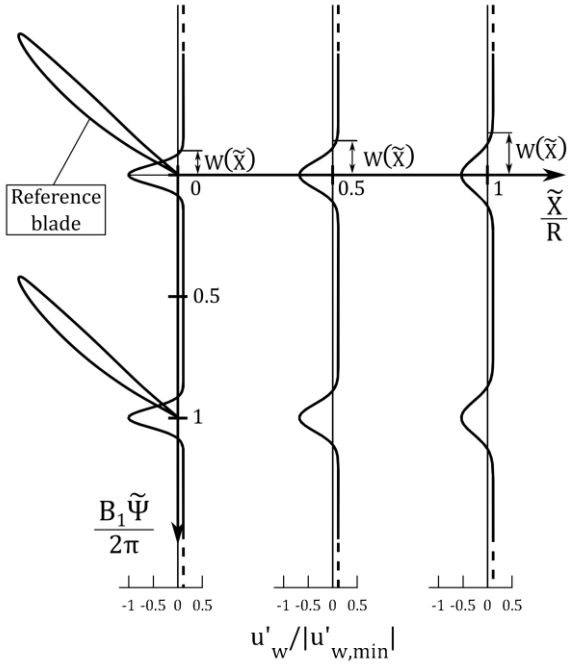

Figure A.1 – Example of axial evolution of the normalized velocity perturbation $u'_w(\tilde{X},\tilde{\Psi})/|u'_{w,min}|$, under the assumptions of Gaussian wake and axial mean flow. $W_0 = 0.1$ and $K \cdot R = 0.02$ are assumed.

$$u'_w(\tilde{X},\tilde{\Psi}) = 2 \cdot Re\left\{\sum_{h=1}^{+\infty} u_w(\tilde{X},h)e^{ihB_1\tilde{\Psi}}\right\}. \tag{A.2}$$

Assuming an axial mean flow and a Gaussian distribution centered at $\tilde{\Psi} = 0$ for the velocity deficit due to the wake, the Fourier coefficients in Eq. (A.2) are [42]:

$$u_w(\tilde{X},h) = u_{w0}e^{-\pi W(\tilde{X})^2h^2}e^{i\pi} = -u_{w0}e^{-\pi W(\tilde{X})^2h^2}\,, \tag{A.3}$$

where u_{w0} determines the peak value of the velocity deficit at the trailing edge and W is the wake width, normalized by the azimuthal interval of one blade passage, $\Delta\tilde{\Psi} = 2\pi/B_1$. $W(\tilde{X})$ describes the spreading of the wake moving downstream (it is proportional to the standard deviation of the Gaussian function) and is modelled by [42,64]:

$$W(\tilde{X}) = \sqrt{W_0^2 + K\tilde{X}}\,, \tag{A.4}$$

where W_0 represents the non-dimensional wake width at the TE and K is a coefficient that accounts for the wake expansion in the downstream direction.

An example illustrating the axial evolution of the circumferential profile $u'_w(\tilde{X}, \tilde{\Psi})$, obtained by means of Eqs. (A.2)-(A.4), is given in Figure A.1. In the figure, the axial and azimuthal coordinates are normalized by the blade section radius and azimuthal interval $\Delta\tilde{\Psi}$, respectively. The three velocity profiles depicted are located at $\tilde{X}/R = 0$, $\tilde{X}/R = 0.5$ and $\tilde{X}/R = 1$, and they are computed assuming $W_0 = 0.1$, $K \cdot R = 0.02$ and considering the sum of $N = 40$ harmonics. The velocity perturbation profiles are normalized using the amplitude of the initial deficit peak at the wake centreline:

$$\left|u'_{w,min}\right| = \left|u'_w(\tilde{X} = 0, \tilde{\Psi} = 0)\right| = \left|2 \cdot \sum_{h=1}^{N} -u_{w0} e^{-\pi W_0^2 h^2}\right|. \tag{A.5}$$

The wake spreading described by the model can be observed in Figure A.1 by comparing the perturbation profiles at different axial coordinates. In fact, moving downstream, the amplitude of the deficit peak decreases while the wake width, $W(\tilde{X})$, increases. It is also observed that u'_w is periodic in the azimuthal direction with period $2\pi/B_1$, corresponding to the azimuthal angle between two consecutive blades.

It should be noted that the phase term $e^{i\pi}$ in Eq. (A.3) is not present in the original formulation of Jaron et al. Since it is known a priori that the viscous wake generates a velocity deficit, this term was introduced in the present formulation in order to have $u'_w(\tilde{X}, \tilde{\Psi} = 0) < 0$ under the assumption of a classic Gaussian wake. However, as it will be shown later on, the introduction of a different phase for each harmonic allows obtaining a deficit at the wake centreline even though term $e^{i\pi}$ is not present.

Typically, the actual mean flow is characterized by a swirl in the reference frame of the rotor. Therefore, the Fourier coefficients $u_w(\tilde{X}, h)$ are modified by introducing a phase shift which depends on the axial coordinate, $\tilde{X}$, to model properly the convection of the wake. The phase shift $exp[-ihB_1(\tan\beta_{rel}/R)\tilde{X}]$ is assumed [42], and the coefficients become:

$$u_w(\tilde{X}, h) = -u_{w0} e^{-\pi W(\tilde{X})^2 h^2} e^{-ihB_1 \frac{\tan\beta_{rel}}{R}\tilde{X}}, \tag{A.6}$$

where β_{rel} is the mean outflow angle in the reference frame of the rotor.

Figure A.2 shows the effect of considering the swirl accounting to Eq. (A.6) in the calculation of the circumferential profiles $u'_w(\tilde{X}, \tilde{\Psi})$. In the reported example, the outflow angle $\beta_{rel} = 45°$

and blade number $B_1 = 8$ are assumed. The wake deficit, computed at different axial coordinates, undergoes an azimuthal shift defined by the direction of the swirling flow in the plane $(\tilde{X}, \tilde{\Psi})$ (dashed arrow in Figure A.2).

The final formulation of the viscous wake model is obtained by relaxing the zero-phase property of the harmonics of a classic Gaussian distribution, which allows the reproduction of an asymmetric velocity deficit. Therefore, a different phase, $\tilde{\varphi}_w(h)$, is introduced for each harmonic and the final form of the Fourier coefficients is [42]:

$$u_w(\tilde{X}, h) = -u_{w0} e^{-\pi W(\tilde{X})^2 h^2} e^{-ihB_1 \frac{\tan\beta_{rel}}{R}\tilde{X}} e^{i\tilde{\varphi}_w(h)} . \tag{A.7}$$

By substituting Eq. (A.7) into Eq. (A.2), the wake model accounting for the swirl and the asymmetric velocity distribution is obtained:

$$u'_w(\tilde{X}, \tilde{\Psi}) = 2 \cdot Re\left\{\sum_{h=1}^{+\infty} -u_{w0} e^{-\pi W(\tilde{X})^2 h^2} e^{i\left[hB_1\left(\tilde{\Psi} - \frac{\tan\beta_{rel}}{R}\tilde{X}\right) + \tilde{\varphi}_w(h)\right]}\right\}. \tag{A.8}$$

Figure A.3 shows the circumferential profiles of $u'_w/|u'_{w,min}|$ computed by setting $\tilde{\varphi}_w(h=1) = \pi/8$ and keeping $\tilde{\varphi}_w(h) = 0$ for $h = 2 \dots N$. The sum of $N = 40$ harmonics is considered. The values of the other model parameters are the same as in the examples of Figures A.1 and A.2. The asymmetric periodic perturbations obtained by introducing the phase shift can be observed.

When considering the relative reference frame (X, R, Ψ), where the coordinates X and Ψ are not centered at the TE of the blade sections, the model perturbations $u'_w(X, \Psi)$ are computed by applying the coordinate transformations $\tilde{X} = X - X_{TE,1}$ and $\tilde{\Psi} = \Psi - \Psi_{TE,1}$. Thus, defining the phase as $\varphi_w(h) = \tilde{\varphi}_w(h) - hB_1\Psi_{TE,1}$ and considering the sum of a finite number of harmonics ($N < +\infty$, in view of the numerical implementation of the model), Eq. (A.8) becomes Eq. (4.1).

Model parameters u_{w0}, W_0, K and $\varphi_w(h)$ have to be calibrated by fitting the RANS solution extracted in the coordinate system (X, R, Ψ) (see Chapter 4).

It should be noted that the phase term $e^{i\pi}$ (see Eq. (A.3)) may be repealed, thus recovering the formulation of the model proposed by Jaron et al. Indeed, the fitting procedure would balance the phase parameters $\varphi_w(h)$ accordingly, and a velocity deficit at the wake centreline could be obtained anyway.

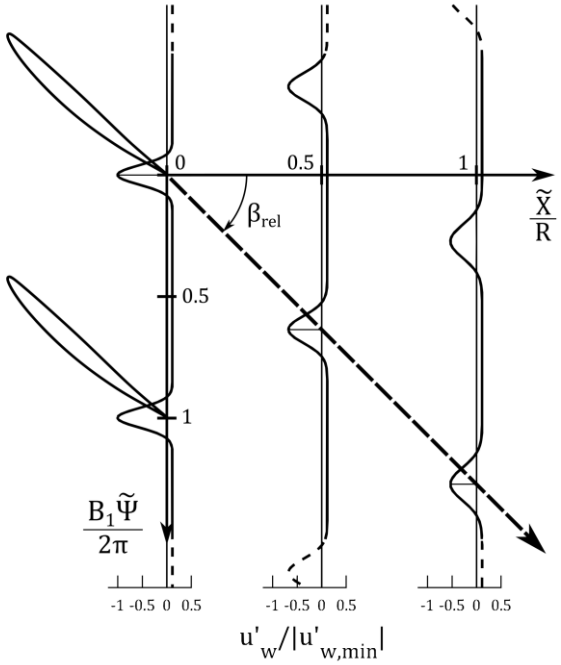

Figure A.2 – Example of axial evolution of the normalized velocity perturbation $u'_w(\tilde{X},\tilde{\Psi})/|u'_{w,min}|$, under the assumptions of Gaussian wake and swirling mean flow. $\beta_{rel} = 45°$, $B_1 = 8$, $W_0 = 0.1$ and $K \cdot R = 0.02$ are assumed.

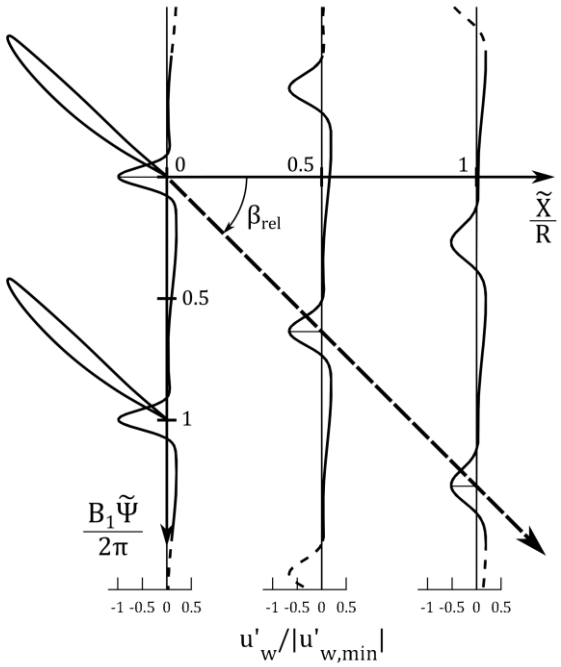

Figure A.3 – Example of axial evolution of the normalized velocity perturbation $u'_w(\tilde{X},\tilde{\Psi})/|u'_{w,min}|$, under the assumptions of asymmetric wake and swirling mean flow. $\tilde{\varphi}_w(h=1) = \pi/8$, $\beta_{rel} = 45°$, $B_1 = 8$, $W_0 = 0.1$ and $K \cdot R = 0.02$, are assumed.

A.2 Contribution of the potential flow

The contribution of the potential flow perturbations is given by the following equation:

$$u'_p(\tilde{X},\tilde{\Psi}) = 2 \cdot Re\left\{\sum_{h=1}^{+\infty} u_p(\tilde{X},h)e^{ihB_1\tilde{\Psi}}\right\}, \tag{A.9}$$

where the modes $u_p(\tilde{X},h)exp(ihB_1\tilde{\Psi})$ are derived from the theory of waves in ducted swirling flows [53]. They represent cut-off modes of the velocity field bound to a subsonic rotor, corresponding to a special solution for the wave equation in an infinitely long circular duct [42,53,65]. The coefficients $u_p(\tilde{X},h)$ are written as follows:

$$u_p(\tilde{X},h) = u_{p0}(h)e^{ik_{X,mn}|\tilde{X}|}e^{i\tilde{\varphi}_p(h)}\,, \tag{A.10}$$

where $k_{X,mn}$ is the axial wavenumber of a mode of azimuthal order $m = hB_1$ and radial order n, while $u_{p0}(h)$ and $\tilde{\varphi}_p(h)$ are the initial amplitude and phase, respectively, of that mode at the trailing edge.

The expression for $k_{X,mn}$ is derived under the assumption of radial equilibrium (i.e., $v_R = 0$) and a solid-body swirl for the absolute mean flow:

$$\bar{v}_\Psi(R) = \Omega R\,. \tag{A.11}$$

A mean flow of axially and radially constant axial Mach number is further assumed ($\partial M_X/\partial X = \partial M_X/\partial R = 0$). Under these assumptions, the axial wavenumber of the modes propagating in downstream direction is given by [53]:

$$k_{X,mn} = \frac{-M_X\left(k_\Psi - m\frac{\Omega}{a_0}\right) + \sqrt{\left(k_\Psi - m\frac{\Omega}{a_0}\right)^2 - (1-M_X^2)\mu_{mn}^2}}{1-M_X^2}, \tag{A.12}$$

where a_0 is the speed of sound, k_Ψ is the azimuthal wavenumber and μ_{mn} is the radial eigenvalue of the wave function.

A 2D flow approximation is adopted, which leads to $\mu_{mn} = m/R$ [42]. Then, the axial wavenumber becomes:

$$k_{X,m} = \frac{-M_X\left(k_\Psi - m\frac{\Omega}{a_0}\right) + \sqrt{\left(k_\Psi - m\frac{\Omega}{a_0}\right)^2 - (1-M_X^2)\left(\frac{m}{R}\right)^2}}{1-M_X^2}. \tag{A.13}$$

Since the modes describe the bound potential field generated by the rotor, they rotate with the rotor itself, and the relation between the azimuthal wavenumber and the blade angular speed, Ω_1, is given by the equation:

$$k_\Psi = m\frac{\Omega_1}{a_0}, \tag{A.14}$$

and the axial wavenumber is:

$$k_{X,m} = \frac{-M_X m\frac{\Omega_1-\Omega}{a_0} + \sqrt{\left(m\frac{\Omega_1-\Omega}{a_0}\right)^2 - (1-M_X^2)\left(\frac{m}{R}\right)^2}}{1-M_X^2}. \tag{A.15}$$

Considering the following relationships for the azimuthal Mach number, $M_{\Psi,rel}$, and the outflow angle, β_{rel}, in the reference frame of the rotor:

$$M_{\Psi,rel}(R) = -R\frac{\Omega_1-\Omega}{a_0}, \tag{A.16}$$

$$\tan\beta_{rel} = \frac{M_{\Psi,rel}}{M_X}, \tag{A.17}$$

and neglecting the radial mean flow component, which gives $M_{rel}^2 = M_X^2 + M_{\Psi,rel}^2$, the final form of the axial wavenumber is obtained:

$$k_{X,m} = \frac{M_X^2 m\frac{\tan\beta_{rel}}{R} + i\frac{|m|}{R}\sqrt{1-M_{rel}^2}}{1-M_X^2}. \tag{A.18}$$

Finally, by substituting Eqs. (A.10) and (A.18) into Eq. (A.9), the potential flow perturbation field is given by:

$$u'_p(\tilde{X},\tilde{\Psi}) = \\ = 2\cdot Re\left\{\sum_{h=1}^{+\infty} u_{p0}(h)\, e^{-hB_1\frac{\sqrt{1-M_{rel}^2}}{1-M_X^2}\frac{|\tilde{X}|}{R}}\, e^{i\left[hB_1\left(\tilde{\Psi}-\frac{M_X^2\tan\beta_{rel}}{1-M_X^2}\frac{\tilde{X}}{R}\right)+\tilde{\varphi}_p(h)\right]}\right\}. \quad \text{(A.19)}$$

For cut-off modes, which vanish moving away from the rotor, the axial wavenumber is complex (see Eq. (A.18)). The real part, $Re(k_{X,m})$, represents the phase shift along the axial coordinate, which describes the mode spinning. The imaginary part, $Im(k_{X,m})$, describes the axial decay of the mode amplitude. Notice that the higher is the blade number the larger is the decay rate.

An example illustrating the axial evolution of the circumferential profile $u'_p(\tilde{X},\tilde{\Psi})$, computed by means of Eq. (A.19), is provided in Figure A.4. The three perturbation profiles depicted are located at $\tilde{X}/R = 0$, $\tilde{X}/R = 0.1$ and $\tilde{X}/R = 0.2$, and they are calculated as the sum of $N = 40$ harmonics. An exponential distribution of the initial amplitudes, $u_{p0}(h) = u_0 exp[-(h-1)]$, and zero initial phases, $\tilde{\varphi}_p(h) = 0$ for $h = 1 \dots N$, are assumed. The blade number, outflow angle and axial Mach number are set to $B_1 = 8$, $\beta_{rel} = 45°$ and $M_X = 0.2$. Consequently, $M_{\Psi,rel} = M_X \tan\beta_{rel} = 0.2$ and $M_{rel}^2 = M_X^2 + M_{\Psi,rel}^2 = 0.08$. The profiles are normalized by the maximum amplitude of the perturbation at the trailing edge, computed as:

$$u'_{p,max} = u'_p(\tilde{X}=0,\tilde{\Psi}=0) = 2\cdot\sum_{h=1}^{+\infty} u_{p0}(h)\,. \quad \text{(A.20)}$$

It is observed that the amplitude of the potential field perturbations decay significantly faster than those of the viscous wake moving away from the rotor (compare Figure A.4 with Figure A.3).

The azimuthal shift of the potential field moving downstream, defined by the spinning of the modes, is indicated by the dashed arrow in Figure A.4. Note that, differently from the viscous wake, the potential field is not convected by the mean flow, and its swirl is influenced by the term $M_X^2/(1-M_X^2)$ (see Eq. (A.19)).

Similarly to the wake model, by applying the coordinate transformations $\tilde{X} = X - X_{TE,1}$ and $\tilde{\Psi} = \Psi - \Psi_{TE,1}$ and defining the phase as $\varphi_p(h) = \tilde{\varphi}_p(h) - hB_1\Psi_{TE,1}$, Eq. (A.19) reduces to Eq. (4.2), which describes the potential flow perturbations in the relative reference frame (X, R, Ψ).

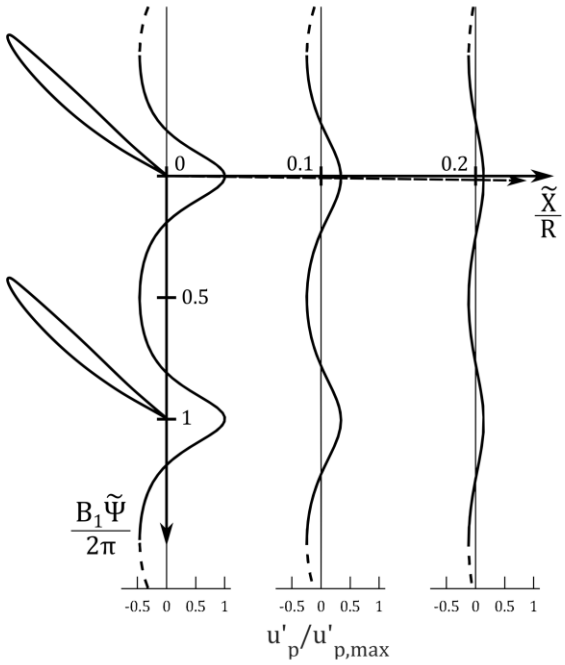

Figure A.4 – Example of axial evolution of the normalized velocity perturbation $u'_p(\tilde{X},\tilde{\Psi})/u'_{p,max}$. $u_{p0}(h) = u_0 exp[-(h-1)]$, $\tilde{\varphi}_p(h) = 0$, $B_1 = 8$, $\beta_{rel} = 45°$ and $M_X = 0.2$ are assumed.

Model parameters $u_{p0}(h)$ and $\varphi_p(h)$ have to be calibrated by fitting the RANS solution extracted in the coordinate system (X, R, Ψ) (see Chapter 4).

Appendix B DERIVATION OF THE BLADE RESPONSE MODEL

In this Appendix, the blade response model adopted in the present work for the calculation of the unsteady blade loads is presented. First, the formulation for the calculation of the unsteady aerodynamic forces acting on a 2D airfoil due to the impingement of a velocity gust is discussed, along with relevant considerations about the phase of the forces. Then, the application of the model to the CROR configuration, involving kinematic considerations for the computation of the model parameters, is reported.

B.1 Unsteady aerodynamic forces on a thin airfoil

Consider a 2D airfoil and a reference frame (x_2, y_2) attached to it, as shown in Figure B.1. It is assumed that the 2D flow relative to the airfoil is inviscid and compressible, consisting of a uniform mean flow, $W\boldsymbol{e}_{x_2}$, that convects a spatial velocity disturbance, $\boldsymbol{v}'$:

$$\boldsymbol{w} = W\boldsymbol{e}_{x_2} + \boldsymbol{v}' , \tag{B.1}$$

where the unit vector $\boldsymbol{e}_{x_2}$ has the direction of the x_2 axis. The flow is steady but not spatially uniform in the reference frame (x_1, y_1) moving with velocity $W\boldsymbol{e}_{x_2}$. The velocity perturbation, $\boldsymbol{v}'$, is frozen with respect to the mean flow and is usually called a gust. $\boldsymbol{v}'$ is perceived as a time disturbance by the airfoil, which causes fluctuating aerodynamic forces on the airfoil surface.

It is assumed that $\boldsymbol{v}'$ is small with respect to the mean flow velocity. Moreover, the aifoil is considered thin, with small camber and at small angle of attack with respect to $W\boldsymbol{e}_{x_2}$. Also, it is reasonable to assume that the presence of the airfoil does not modify the gust $\boldsymbol{v}'$. Under these assumptions, the flow field can be considered linear.

Considering the relationship between coordinates (x_1, y_1) and (x_2, y_2):

$$\begin{cases} x_1 = x_2 - Wt \\ y_1 = y_2 \end{cases} , \tag{B.2}$$

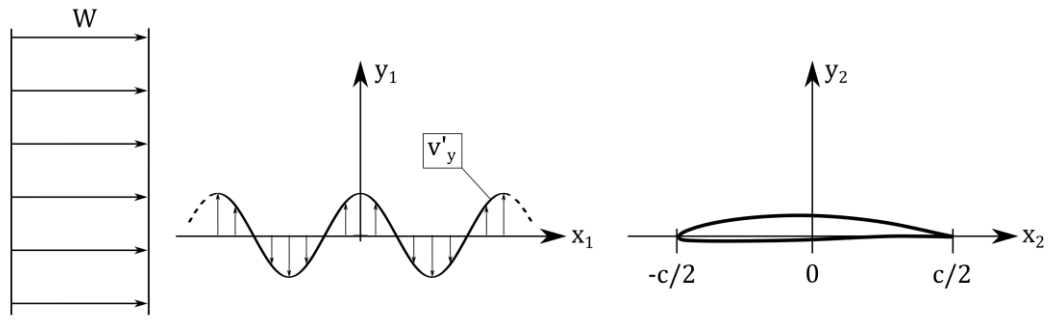

Figure B.1 – Reference frame of the airfoil, (x_2, y_2), reference frame of the gust, (x_1, y_1), and representation of the harmonic of the upwash velocity gust, v'_y.

the gust velocity can be represented as a superposition of plane waves [37] according to the equation:

$$\boldsymbol{v'} = \int \boldsymbol{v'}_k e^{i(k_x x_1 + k_y y_1)} d\boldsymbol{k} = \int \boldsymbol{v'}_k e^{i(k_x x_2 + k_y y_2 - k_x W t)} d\boldsymbol{k}\,, \tag{B.3}$$

where k_x and k_y are the components of the wavenumber $\boldsymbol{k} = k_x \boldsymbol{e}_{x_2} + k_y \boldsymbol{e}_{y_2}$. Since the flow field is linear, the unsteady forces induced by any velocity disturbance $\boldsymbol{v'}$ can be obtained by superposing the effects of incident harmonic gusts:

$$\boldsymbol{v'} = \boldsymbol{v'}_k e^{i(k_x x_2 + k_y y_2 - k_x W t)}\,. \tag{B.4}$$

A closed form solution of the problem is given by Goldstein [37], under the additional assumption that the airfoil is a semi-infinite flat plate, normal to y_2 and extending from $x_2 = -c/2$ to infinity. Moreover, it is assumed that the gust is a harmonic of the upwash velocity component, i.e., the component parallel to y_2, and its wavefront is normal to the plate, i.e., normal to x_2 (see Figure B.1), that is:

$$\boldsymbol{v'}(x_2, t) = v'_y(x_2, t)\boldsymbol{e}_{y_2} = v_{y,k} e^{i(k_x x_2 - k_x W t)} \boldsymbol{e}_{y_2}\,, \tag{B.5}$$

where $v_{y,k}$ represents the amplitude of the harmonic. Hence, the fluctuating pressure difference across the plate is given by the following equation [37]:

$$\Delta p'(x_2,t) = \frac{-i2\rho_0 W v_{y,k} e^{-i\sigma_x}}{\sqrt{i\pi\sigma_x(1+M_{rel})(2x_2/c+1)}} e^{i\left[\frac{M_{rel}\sigma_x(2x_2/c+1)}{1+M_{rel}} - k_x W t\right]}. \tag{B.6}$$

In this equation, ρ_0 and $M_{rel} = W/a_0$ are the freestream density and Mach number, respectively, while $\sigma_x = k_x c/2$ is the reduced frequency of the perturbation. By integrating Eq. (B.6) over the chord length, the net fluctuating lift force per unit span is obtained:

$$L'(t) = \int_{-c/2}^{c/2} \Delta p'(x_2,t) dx_2 = \pi\rho_0 c v_{y,k} W S_c(\sigma_x, M_{rel}) e^{-i\, k_x W t}\,, \tag{B.7}$$

where S_c is the high-frequency approximation of the compressible Sears function, already given in Eq. (4.8) and here reported for convenience:

$$S_c(\sigma_x, M_{rel}) = \frac{e^{-i\sigma_x}}{\sigma_x \pi} \sqrt{\frac{2i}{M_{rel}}} F\left(\sqrt{\frac{4\sigma_x M_{rel}}{\pi(1+M_{rel})}}\right), \tag{B.8}$$

and

$$F(\chi) = \int_0^{\chi} e^{i\frac{\pi}{2}\xi^2} d\xi \tag{B.9}$$

is the complex Fresnel integral. The validity condition of Eq. (B.7) is $M_{rel}\sigma_x/\left(1-M_{rel}^2\right) > 1$, which indicates that the compressibility effects become important at high frequencies, even when M_{rel} is small.

Note that, in the case of incompressible flow, the unsteady lift obtained by means of the linearized theory acts through the quarter-chord point (see Von Kármán and Sears [66] and Sears [67]). However, in a real compressible flow, the centre of lift moves toward the trailing edge as the frequency of the impinging perturbation increases. Therefore, the contribution of the trailing edge region to the net lift can be considered relatively unimportant. This justifies the adopted simplification of considering the airfoil as a semi-infinite flat plate.

Eqs. (B.2) and (B.5) imply that, at time $t = 0$, the origins of the reference frames (x_1, y_1) and (x_2, y_2) are coincident, and the phase of the harmonic gust is zero at $x_1 = x_2 = 0$, as shown in Figure B.2 a). Therefore, the initial phase of $L'(t = 0)$, corresponding to the phase of the complex

function S_c (see Eq. (B.7)), is related to this particular initial condition for the upwash gust. The more general case of a harmonic upwash with arbitrary initial phase, ϕ, in the reference frame (x_1, y_1), and an initial position, Δx_2, with respect to the midchord point is here considered (see Figure B.2 b)). Thus, the relationship between the axial coordinates becomes:

$$x_1 = x_2 - \Delta x_2 - Wt\,, \tag{B.10}$$

and the gust is given by the equation:

$$v'_y = v_{y,k} e^{i(k_x x_1 + \phi)} = v_{y,k} e^{i(k_x x_2 - k_x W t)} e^{i(-k_x \Delta x_2 + \phi)}\,, \tag{B.11}$$

showing that the phase of the gust at time $t = 0$ with respect to the midchord point $x_2 = 0$ corresponds to $\Delta\phi = -k_x \Delta x_2 + \phi$. The initial phase of the unsteady lift is changed accordingly by introducing the phase shift $\Delta\phi$:

$$L'(t) = \pi \rho_0 c v_{y,k} W S_c(\sigma_x, M_{rel}) e^{i(-k_x \Delta x_2 + \phi)} e^{-i\, k_x W t}. \tag{B.12}$$

As it will be shown later, this general formulation, which accounts for arbitrary initial phases of the harmonic upwash gust, is useful for the application of the blade response model to the CROR configuration. Indeed, in that case, the harmonic gusts are computed at the leading edge of the blade sections (that is, $\Delta x_2 = -c/2$), where they may have an initial phase $\phi \neq 0$.

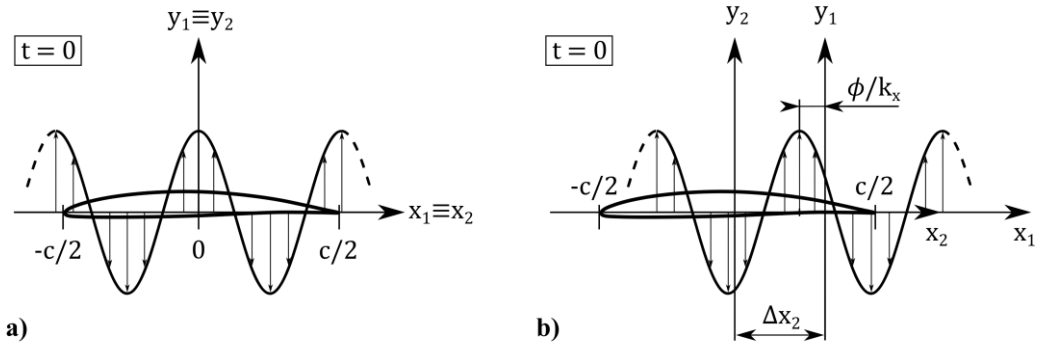

Figure B.2 – Initial condition ($t = 0$) for the harmonic gust.
a) initial phase zero at the midchord point $x_2 = 0$,
b) initial phase $\Delta\phi = -k_x \Delta x_2 + \phi$ at the midchord point $x_2 = 0$.

B.2 Application of the blade response to the CROR configuration

The blade response model proposed by Goldstein can be used to compute the unsteady lift on a rotor blade due to the interaction with periodic velocity perturbations. Since the model relies on 2D assumptions, the blade is divided into cylindrical sections, which are treated as isolated thin airfoils, and the blade response is computed separately for each section.

Suppose that the velocity perturbation, $\boldsymbol{v}'$, is generated by the FR and impacts a blade of the RR. In this case, particular conditions hold for $\boldsymbol{v}'$ and some important considerations are presented hereafter to clarify how the perturbation is perceived by the rear blade. The equations for the wavenumber and reduced frequency of the perturbation detected by an airfoil radial section of the rear blade are then obtained.

Consider a cylindrical reference frame (X, R, Ψ^*) fixed to the FR, where the azimuthal coordinate, Ψ^*, is measured in the rotation direction of the rotor. The blade sections of radius R of front and rear rotors are represented in the unwrapped 2D reference frame $(X, R\Psi^*)$ moving with the FR, as shown in Figure B.3. It is assumed that the velocity perturbation $\boldsymbol{v}'$ is generated by the front blades and is convected by a uniform flow, $\boldsymbol{W}_1$, in the reference frame $(X, R\Psi^*)$. Due to the relative rotation of the two rotors, the blade sections of the RR perceive the perturbation as convected by the relative mean flow $\boldsymbol{W}_2$ (see Figure B.3). Consider the coordinate system (x_2, y_2) attached to the blade section of one of the rear blades (say, the reference blade), where x_2 and y_2 are parallel and normal to $\boldsymbol{W}_2$, respectively. The blade section is considered thin, with small camber and small angle of attack with respect to $\boldsymbol{W}_2$. Therefore, it is assumed that the airfoil lies on $y_2 = 0$ and $-c_2/2 \leq x_2 \leq c_2/2$.

According to the blade response model of Goldstein, the component of $\boldsymbol{v}'$ responsible for the loading fluctuation is the upwash ${v'}_{y_2}$, parallel to axis y_2. Since the model is linear, a single harmonic of the upwash gust is considered. The objective is to obtain the analytical form of ${v'}_{y_2}(x_2, t)$, from which the chordwise wavenumber of the perturbation perceived by the blade section can be identified.

It is assumed for the moment that the harmonic ${v'}_{y_2}(X, R\Psi^*)$ has zero phase at coordinates $X = 0$ and $R\Psi^* = 0$. Since $\boldsymbol{v}'$ is periodic in the circumferential direction Ψ^* with period equal to $\Delta\Psi^* = 2\pi/B_1$, the harmonic of order h of the velocity gust in the coordinate system $(X, R\Psi^*)$ is given by the equation:

$$ {v'}_{y_2}(X = 0, R\Psi^*) = \left|v_{y_2}(h)\right| e^{i\left(h\frac{2\pi}{R\Delta\Psi^*}R\Psi^*\right)} = \left|v_{y_2}(h)\right| e^{i\left(h\frac{B_1}{R}R\Psi^*\right)}, \qquad \text{(B.13)} $$

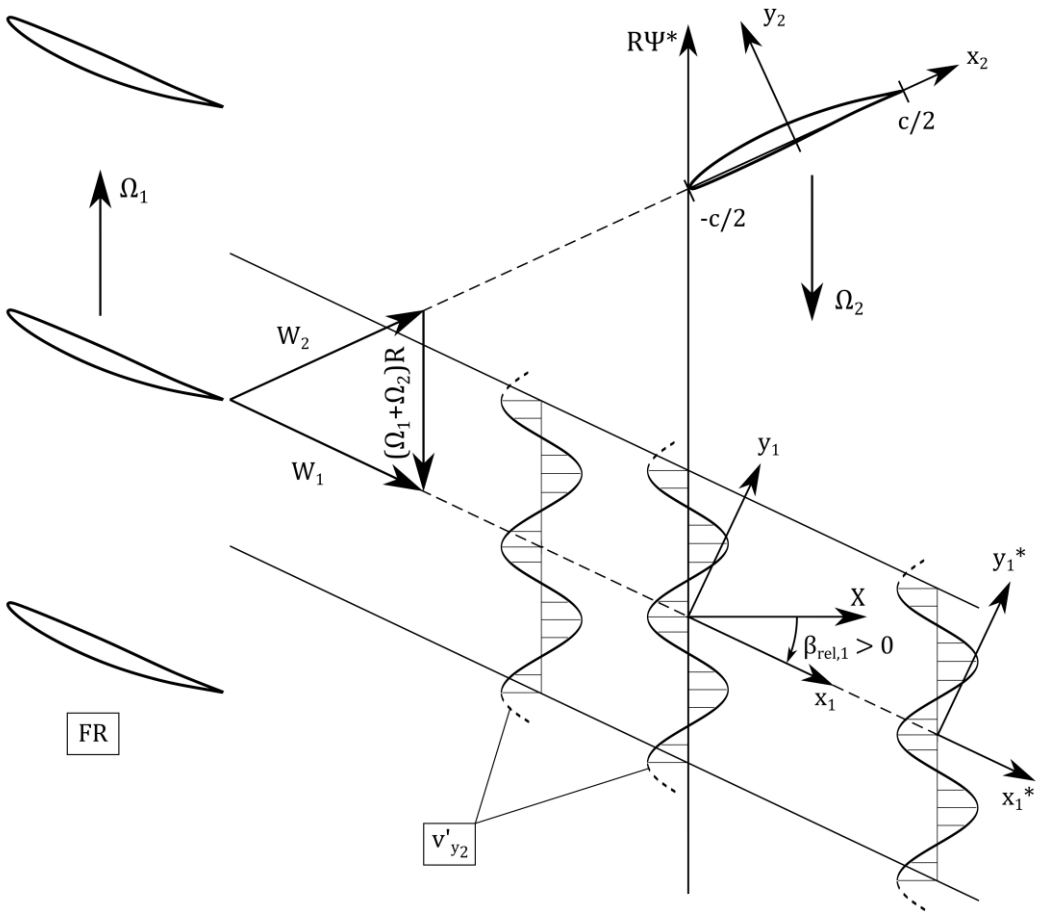

Figure B.3 – Blade sections of front and rear rotors, and pattern of the upwash harmonic gust, v'_{y_2}, generated by the front rotor.

where $\left|v_{y_2}(h)\right|$ represents the amplitude of the harmonic. One of the assumptions of the blade response model is that the convected gust is frozen, i.e., it is time independent in a reference frame moving with the mean flow. To clarify the consequences of this assumption, consider the coordinate systems (x_1, y_1) and (x_1^*, y_1^*) shown in Figure B.3. The former is attached to the front rotor while the latter moves with the relative mean flow $\boldsymbol{W}_1$. Both x_1 and x_1^* axes are aligned with the direction of $\boldsymbol{W}_1$, so that the coordinates (x_1, y_1) and (x_1^*, y_1^*) are related by:

$$\begin{cases} x_1^* = x_1 - W_1 t \\ y_1^* = y_1 \end{cases}, \tag{B.14}$$

where $W_1 = |\boldsymbol{W}_1|$.

Since the profile of v'_{y_2} given by Eq. (B.13) is generated by the FR, it is steady in the coordinate system (x_1, y_1). Nevertheless, the profile must be steady also in the coordinate system

(x_1^*, y_1^*). Consequently, in order to satisfy the assumption of frozen gust, v'_{y_2} must be independent of both x_1 and x_1^* coordinates, that is, the profile is convected rigidly with the mean flow velocity $\boldsymbol{W}_1$, as depicted in Figure B.3. Thus, the harmonic gust can be expressed in y_1^* coordinate as:

$$v'_{y_2}(y_1^*) = \left|v_{y_2}(h)\right| e^{i\left(\frac{hB_1}{R}\frac{y_1}{\cos\beta_{rel,1}}\right)} = \left|v_{y_2}(h)\right| e^{i\left(\frac{hB_1}{R}\frac{y_1^*}{\cos\beta_{rel,1}}\right)}, \tag{B.15}$$

where $\beta_{rel,1}$ is the angle between the axial direction and the direction of $\boldsymbol{W}_1$, (see Figure B.3).

Knowing the gust pattern $v'_{y_2}(y_1^*)$, the formulation for $v'_{y_2}(x_2, t)$ can be easily obtained. To do so, a coordinate system (x_2^*, y_2^*), which moves with the mean flow velocity $\boldsymbol{W}_2$ relative to the rear blade section, is introduced (see Figure B.4). The relationship between coordinates (x_2^*, y_2^*) and (x_2, y_2) is given by:

$$\begin{cases} x_2^* = x_2 - W_2 t \\ y_2^* = y_2 \end{cases}, \tag{B.16}$$

where $W_2 = |\boldsymbol{W}_2|$. Without loss of generality, it is assumed that at time $t = 0$ the origins of the coordinate systems (x_1^*, y_1^*), (x_2, y_2) and (x_2^*, y_2^*) are coincident, as shown in Figure B.4 a), and the phase of v'_{y_2} is zero at $y_1^* = 0$, so that $v'_{y_2}(y_1^*)$ is given by Eq. (B.15). Note that this initial condition corresponds to the one illustrated in Figure B.2 a). At any time $t > 0$, the origins of (x_1^*, y_1^*) and (x_2^*, y_2^*) are still coincident since both coordinate systems moves with the mean flow (see Figure B.4 b)), and the relationship between these coordinates is as follows:

$$\begin{cases} x_1^* = x_2^* \cos\mu - y_2^* \sin\mu \\ y_1^* = x_2^* \sin\mu + y_2^* \cos\mu \end{cases}, \tag{B.17}$$

where μ is the angle between axes x_1^* and x_2^*, as indicated in the figure. Considering Eq. (B.17), the harmonic upwash in terms of (x_2^*, y_2^*) is given by:

$$v'_{y_2}(x_2^*, y_2^*) = \left|v_{y_2}(h)\right| e^{\left[i\left(\frac{hB_1}{R}\frac{(x_2^*\sin\mu + y_2^*\cos\mu)}{\cos\beta_{rel,1}}\right)\right]}. \tag{B.18}$$

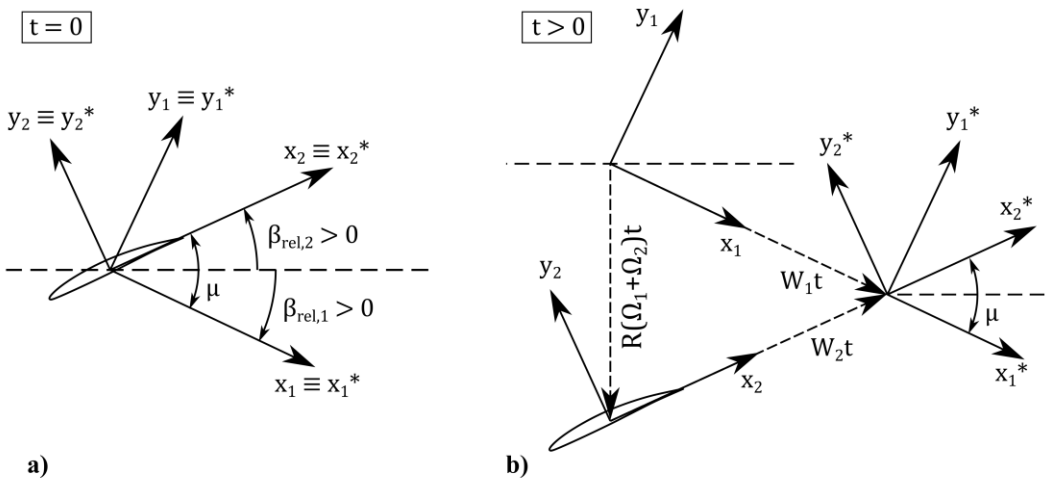

Figure B.4 – Coordinate systems useful for the computation of the upwash gust $v'_{y_2}(x_2,t)$ perceived by the rear blade section. **a)** position of the coordinate systems at time $t = 0$ (origin at the midchord point), **b)** position of the coordinate systems at time $t > 0$.

Finally, since the airfoil is assumed to lie on $y_2^* = y_2 = 0$, and substituting Eq. (B.16) into Eq. (B.18), the equation describing the upwash gust perceived by the rear blade section is obtained:

$$v'_{y_2}(x_2,t) = \left|v_{y_2}(h)\right| e^{\left[i\frac{hB_1}{R}\frac{\sin\mu}{\cos\beta_{rel,1}}(x_2 - W_2 t)\right]} = \left|v_{y_2}(h)\right| e^{\left[i(k_{x_2}x_2 - k_{x_2}W_2 t)\right]}. \quad \text{(B.19)}$$

Equation (B.19) allows identifying the chordwise wavenumber

$$k_{x_2} = \frac{hB_1}{R}\frac{\sin\mu}{\cos\beta_{rel,1}} \quad \text{(B.20)}$$

and the reduced frequency, $\sigma_{x_2} = k_{x_2}c_2/2$.

For the application of the blade response model to the CROR configuration, the circumferential profile of v'_{y_2} is computed at the axial coordinate of the LE of the blade section, $X_{LE,2}$, and is given by (see also Eq. (4.6)):

$$v'_{y_2}\left(X_{LE,2}, R\Psi^*\right) = \left|v_{y_2}(h)\right| e^{i\left(h\frac{B_1}{R}R\Psi^* + \Psi^*(h)\right)} = \left|v_{y_2}(h)\right| e^{i(hB_1\Psi^* + \Psi^*(h))}, \quad \text{(B.21)}$$

where $\Psi^*(h)$ is the phase of the harmonic at $\Psi^* = 0$, which depends on the actual distribution of $\boldsymbol{v}'\left(X_{LE,2}, \Psi^*\right)$. At time $t = 0$, the phase of the harmonic gust at the LE of the blade section, that

is, $x_2 = -c_2/2$, corresponds to $\phi = hB_1\Psi^*_{LE,2} + \Psi^*(h)$. Therefore, the phase shift $\Delta\phi = k_{x_2}c_2/2 + \phi$ is introduced to account for the initial phase of the gust with respect to the midchord point, which leads to:

$$v'_{y_2}(x_2,t) = \left|v_{y_2}(h)\right| e^{i(k_{x_2}x_2 - k_{x_2}W_2 t)} e^{i(k_{x_2}c_2/2+\phi)} . \tag{B.22}$$

Equation (B.22) is analogous to Eq. (B.11). Thus, the fluctuating lift force per unit span acting on the blade section, calculated by the blade response, is as follows:

$$L'_2(t) = \pi\rho_0 c_2 \left|v_{y_2}(h)\right| W_2 S_c\left(\sigma_{x_2}, M_{rel,2}\right) e^{i\left(k_{x_2}\frac{c_2}{2}+\phi\right)} e^{-i\,k_{x_2}W_2 t} , \tag{B.23}$$

where $M_{rel,2} = W_2/a_0$ is the Mach number of the mean flow relative to the blade section.

Eq. (B.23) demonstrates that the Fourier coefficients, $L_2(h)$, of the unsteady lift described in Chapter 4 are given by Eq. (4.7).

Finally, a useful expression for the chordwise wavenumber, k_{x_2}, in terms of the angular speeds of the two rotors and the mean flow velocity can be obtained. Consider angles $\beta_{rel,1}$, $\beta_{rel,2}$ and μ, defined in Figure B.4, and the following relations for the axial and tangential components of the relative mean flow velocity:

$$W_{X,1} = W_{X,2} = W_1 \cos\beta_{rel,1} = W_2 \cos\beta_{rel,2} , \tag{B.24}$$

$$W_{\Psi,1} = W_1 \sin\beta_{rel,1} , \tag{B.25}$$

and

$$W_{\Psi,2} = W_2 \sin\beta_{rel,2} . \tag{B.26}$$

Then, the following relationships hold:

$$\frac{\sin\mu}{R\cos\beta_{rel,1}} = \frac{\sin\left(\beta_{rel,1}+\beta_{rel,2}\right)}{R\cos\beta_{rel,1}} = \frac{1}{R}\left(\frac{\cos\beta_{rel,2}}{\cos\beta_{rel,1}}\sin\beta_{rel,1} + \sin\beta_{rel,2}\right). \tag{B.27}$$

Since $\cos\beta_{rel,2}/\cos\beta_{rel,1} = W_1/W_2$ (Eq. (B.24)), and noting that $W_{\Psi,1} + W_{\Psi,2} = R(|\Omega_1| + |\Omega_2|)$, we can write:

$$\frac{\sin\mu}{R\cos\beta_{rel,1}} = \frac{W_1\sin\beta_{rel,1} + W_2\sin\beta_{rel,2}}{RW_2} = \frac{W_{\Psi,1} + W_{\Psi,2}}{RW_2} = \frac{|\Omega_1| + |\Omega_2|}{W_2}. \quad \text{(B.28)}$$

By substituting Eq. (B.28) into Eq. (B.20), the following formula for the chordwise wavenumber is obtained:

$$k_{x_2} = \frac{hB_1(|\Omega_1| + |\Omega_2|)}{W_2}, \quad \text{(B.29)}$$

and the reduced frequency can be computed as:

$$\sigma_{x_2} = k_{x_2}\frac{c_2}{2} = \frac{hB_1(|\Omega_1| + |\Omega_2|)c_2}{2W_2}. \quad \text{(B.30)}$$

Eq. (B.29) shows that the frequency of the unsteady lift, $k_{x_2}W_2$, depends on the harmonic order h of the upwash gust, the number of blades B_1 of the rotor that generates the velocity perturbation, and the relative angular speed of the two rotors. Expressions (B.29) and (B.30) for k_{x_2} and σ_{x_2} are the same given in Chapter 4.

Appendix C DERIVATION OF THE NOISE PROPAGATION MODEL

The model proposed by Hanson [39] is adopted in the present work for the computation of the interaction noise tones emitted by the rear rotor. In this Appendix, the derivation of the equations provided in Chapter 4 for the calculation of the acoustic pressure amplitude (Eqs. (4.11) and (4.12)) is presented.

The starting point for the derivation of the model is the Goldstein's version of the acoustic analogy which gives the density disturbance, $\rho' = \rho - \rho_0$, caused by surfaces in arbitrary motion [37]:

$$\rho'(\boldsymbol{x},t) = -\frac{1}{a_0^2}\int_{-T}^{T}\int_{S(\tau)}\left(\rho_0 \boldsymbol{v}_n \frac{\partial G}{\partial \tau} + l_i \frac{\partial G}{\partial y_i}\right) dS(\tau) d\tau$$

$$+ \frac{1}{a_0^2}\int_{-T}^{T}\int_{v(\tau)} T_{ij}\frac{\partial^2 G}{\partial y_i \partial y_j} d\boldsymbol{y} d\tau \ . \tag{C.1}$$

Eq. (C.1) applies to any volume region $v(\tau)$ bounded by impermeable surfaces $S(\tau)$. $\boldsymbol{x} = (x_1, x_2, x_3)$ and $\boldsymbol{y} = (y_1, y_2, y_3)$ are the observer and source coordinates, respectively, measured from a reference point in the quiescent fluid. t is the observer time, while τ is the source (emission) time. The monopole source, $\boldsymbol{v}_n$, is the normal surface velocity, which is responsible for the thickness noise contribution generated by the volume displacement caused by the surface motion. The dipole sources, l_i, are the components of the force per unit area exerted by the fluid on surface $S(\tau)$, which give the loading noise contribution. T_{ij} is the Lighthill's stress tensor, which contains the viscous and nonlinear effects and describes the quadrupole noise contribution [33]. G is the free-space Green's function, given by:

$$G = \frac{\delta(t - \tau - d/a_0)}{4\pi d}, \tag{C.2}$$

where δ is the Dirac delta function and $d = |\boldsymbol{x} - \boldsymbol{y}|$. When distance d between observer and noise sources is large enough, $a_0^2\rho'$ can be identified as the acoustic pressure disturbance, p'.

For rigid surfaces $S(\tau)$, which is the case of a rotating blade, Eq. (C.1) reduces to the well-known Ffowcs Williams-Hawkings equation [24,37].

Consider the application of Eq. (C.1) to a propeller blade in forward motion with speed v_0 and rotating with angular speed Ω. The geometrical simplification of considering the noise sources as distributed on the helicoidal surface swept out by the blade PCA during its motion is adopted [38] (see Figure 4.4). The source strengths $\boldsymbol{v}_n$ and l_i are determined from the actual blade geometry, but their point of action is assumed to lie on the helicoidal surface. Then, it is convenient to introduce the helicoidal source coordinates $\gamma_i = (\gamma, \xi, R)$, where R is the radial coordinate while γ and ξ are arc lengths measured on a cylindrical surface of radius R. γ is the distance along the helix, measured backward from the location of the PCA at time $t = 0$ (see Figure 4.5 b)). ξ is measured normal to R and γ directions, so that $\xi = 0$ corresponds to the helicoidal surface.

The helicoidal surface is fixed in space and the sources are convected in direction $-\gamma$ at the advancing speed $V_{adv}(R) = (v_0^2 + \Omega^2 R^2)^{1/2}$. For analytical convenience, the convected source system is replaced by an equivalent system, $\boldsymbol{v}_n$, l_i, T_{ij}, that is fixed in space but timed to be activated by the passing of the blade. Thus, the sources are defined along the whole helix, i.e., $-\infty < \gamma < \infty$, but they are nonzero only at the blade locations. Considering these approximations, the equation for the acoustic pressure becomes:

$$p'(\boldsymbol{x},t) = a_0^2\rho'(\boldsymbol{x},t) = -\int_{-\infty}^{\infty}\int_{0}^{R_T}\int_{-\infty}^{\infty}\left(\rho_0 \boldsymbol{v}_n \frac{\partial G}{\partial \tau} + l_i \frac{\partial G}{\partial \gamma_i}\right) d\gamma dR d\tau$$

$$+ \int_{-\infty}^{\infty}\int_{0}^{R_T}\int_{-\infty}^{\infty}\int T_{ij}\frac{\partial^2 G}{\partial \gamma_i \partial \gamma_j} d\xi d\gamma dR d\tau \ , \qquad \text{(C.3)}$$

where T_{ij} is assumed to be sufficiently localized so that the ξ integration does not extend to the helicoidal surface of the adjacent blades.

To the purpose of computing the interaction noise emission, only the dipole sources l_i are taken into account, since the thickness noise due to $\boldsymbol{v}_n$ is independent of the aerodynamic interaction between rotors and the quadrupole sources T_{ij} are considered negligible. l_i is interpreted as the sum of the values on the upper and lower (in ξ direction) blade surfaces. It is convenient to express the surface sources l_i as volume sources by using the delta function [38]:

$$l_i(\gamma, R) = \int L_i(\gamma, \xi, R) d\xi \,, \tag{C.4}$$

where

$$L_i(\gamma, \xi, R) = l_i(\gamma, R)\delta(\mathrm{FA} + \xi) \,. \tag{C.5}$$

In Eq. (C.5), FA is the local face alignment of the blade section of radius R, as defined in Figure 4.5 b), and function $\delta(\mathrm{FA} + \xi)$ places the sources on surface $\xi = -\mathrm{FA}$, thus accounting for the local lean of the blade. Components l_γ and l_ξ of the forces per unit area, that is, the components in γ and ξ directions, are taken into account [39]. Thus, considering Eqs. (C.4) and (C.5), the acoustic pressure is given by:

$$p'(\boldsymbol{x}, t) = -\int_{-\infty}^{\infty} \int_{0}^{R_T} \int_{-\infty}^{\infty} \int \left[\left(l_\gamma \frac{\partial G}{\partial \gamma} + l_\xi \frac{\partial G}{\partial \xi} \right) \delta(\mathrm{FA} + \xi) \right] d\xi d\gamma dR d\tau \,. \tag{C.6}$$

Integration by parts allows shifting the derivatives from the Green's function to the source functions and the following form of the equation is obtained:

$$p'(\boldsymbol{x}, t) = \int \int \int \int g(\gamma, \xi, R) \frac{\delta(t - \tau - d/a_0)}{4\pi d} d\xi d\gamma dR d\tau \,, \tag{C.7}$$

where g is the generalized source function defined as:

$$g(\gamma, \xi, R) = \frac{\partial}{\partial \gamma} l_\gamma(\gamma, R)\delta(\mathrm{FA} + \xi) + l_\xi(\gamma, R)\delta'(\mathrm{FA} + \xi) \,. \tag{C.8}$$

The frequency domain representation of the source distributions can be obtained by considering a Fourier series for the time evolution and a wavenumber representation in space [38,39,68]. Consider the impingement of periodic velocity disturbances on the blade. This causes periodic fluctuations of the strength of the dipole sources and their time dependence can be expressed by means of a Fourier series:

$$l_\gamma(\gamma, R, \tau) = \sum_{h=-\infty}^{\infty} l_{\gamma h}(\gamma, R) e^{-i\omega_h \tau} \tag{C.9}$$

and

$$l_\xi(\gamma, R, \tau) = \sum_{h=-\infty}^{\infty} l_{\xi h}(\gamma, R) e^{-i\omega_h \tau}\,, \tag{C.10}$$

where the Fourier coefficients $l_{\gamma h}$ and $l_{\xi h}$ are the forces per unit area for harmonic order h, and ω_h is the angular frequency of the harmonic. Then, the generalized source function can be written as:

$$g(\gamma, \xi, R, \tau) = \sum_{h=-\infty}^{\infty} g_h(\gamma, \xi, R) e^{-i\omega_h \tau}\,, \tag{C.11}$$

where $g_h(\gamma, \xi, R)$ is given by:

$$g_h(\gamma, \xi, R) = \frac{\partial}{\partial \gamma} l_{\gamma h}(\gamma, R)\delta(\mathrm{FA} + \xi) + l_{\xi h}(\gamma, R)\delta'(\mathrm{FA} + \xi)\,. \tag{C.12}$$

A wavenumber representation of the source distribution in space is defined through the Fourier transform pair given by the equations:

$$\hat{g}_h\left(\frac{\omega}{V_{adv}}, \xi, R\right) = \int_{-\infty}^{\infty} g_h(\gamma, \xi, R) e^{i\frac{\omega}{V_{adv}}\gamma} d\gamma\,, \tag{C.13}$$

$$g_h(\gamma, \xi, R) = \frac{1}{2\pi V_{adv}} \int_{-\infty}^{\infty} \hat{g}_h(\gamma, \xi, R) e^{-i\frac{\omega}{V_{adv}}\gamma} d\omega\,, \tag{C.14}$$

where $\omega/V_{adv}(R)$ represents the spatial wavenumber of the sources in direction γ (i.e., chordwise). Therefore, accounting for Eqs. (C.11) and (C.14) and substituting into Eq. (C.7), the acoustic pressure depending on the source distribution in the time-space frequency domain is obtained:

$$p'(\boldsymbol{x},t) = \int\int\int\int \frac{1}{8\pi^2 V_{adv} d} \int \sum_{h=-\infty}^{\infty} \left\{\hat{g}_h e^{-i\omega_h \tau}\right\} e^{-i\frac{\omega}{V_{adv}}\gamma}$$

$$\times\ \delta(t-\tau-d/a_0) d\omega d\xi d\gamma dR d\tau\,. \tag{C.15}$$

Eq. (C.15) can be specialized to compute the acoustic pressure disturbance generated by a rear rotor with B_2 blades, rotating with angular speed Ω_2, which impinges the velocity perturbations generated by a front rotor with B_1 blades counter-rotating with angular speed Ω_1. In this case, the time frequency of the dipole sources on the rear blades for harmonic order h corresponds to $\omega_h = hB_1(|\Omega_1| + |\Omega_2|)$, as shown in Appendix B (see Eq. (B.29)). In the following, the index h is called h_1 to highlight that it actually corresponds to the harmonic order of the periodic velocity perturbations in space generated by the FR. It is further assumed that the observer location is in the far field, that is, $d \gg R_{T,2}$. The observer position is defined in a spherical coordinate system, (ϱ, φ, ψ), that moves forward with the propeller at speed v_0, and defined as shown in Figure C.1. The polar angle, φ, is equal to 90° in the plane of rotation of the RR, while the azimuthal angle, ψ, is measured in the rotational direction of the RR, from the (arbitrary) position of one of the rear blades at time $t = 0$. Hanson [39] shows that, under these assumptions, the acoustic pressure detected by an observer moving forward with the rotor becomes (the full demonstration is omitted for brevity):

$$p'(\varrho,\varphi,\psi,t) = \frac{-i\rho_0 a_0^2 B_2 D_2}{8\pi\varrho(1-M_0\cos\varphi)}$$

$$\times \sum_{h_2=-\infty}^{\infty} \sum_{h_1=-\infty}^{\infty} e^{i(h_2B_2 - h_1B_1)\left(\psi - \frac{\pi}{2}\right)} e^{i(h_2B_2|\Omega_2| + h_1B_1|\Omega_1|)\left(\frac{\varrho}{a_0} - t\right)}$$

$$\times \int_{hub}^{tip} M_{adv,2}^2 e^{i(\phi_l + \phi_s)} \mathcal{J}_{h_2B_2 - h_1B_1}(q) \left[k_\gamma \frac{C_{Dh_1}}{2}\Psi_{Dh_1} + k_\xi \frac{C_{Lh_1}}{2}\Psi_{Lh_1}\right] d\left(\frac{R}{R_{T,2}}\right), \tag{C.16}$$

where the wavenumbers k_γ and k_ξ are given by:

$$k_\gamma = \frac{2M_{T,2}}{M_{adv,2}}\left[\frac{h_2B_2 + h_1B_1\Omega_{12}}{1 - M_0\cos\varphi} - h_1B_1(1+\Omega_{12})\right]\frac{c_2}{D_2}, \tag{C.17}$$

$$k_\xi = -\frac{2}{M_{adv,2}}\left[\frac{(h_2B_2 + h_1B_1\Omega_{12})M_{T,2}^2 R\cos\varphi}{R_{T,2}(1 - M_0\cos\varphi)} - \frac{R_{T,2}(h_2B_2 - h_1B_1)M_0}{R}\right]\frac{c_2}{D_2}, \quad \text{(C.18)}$$

while

$$\phi_s = \frac{2M_{T,2}}{M_{adv,2}}\left[\frac{h_2B_2 - h_1B_1\Omega_{12}}{1 - M_0\cos\varphi} - h_1B_1(1 + \Omega_{12})\right]\frac{\mathrm{MCA}}{D_2} = k_\gamma\frac{\mathrm{MCA}}{c_2}, \quad \text{(C.19)}$$

$$\phi_l = \frac{2}{M_{adv,2}}\left[\frac{(h_2B_2 + h_1B_1\Omega_{12})M_{T,2}^2 R\cos\varphi}{R_{T,2}(1 - M_0\cos\varphi)} - \frac{R_{T,2}(h_2B_2 - h_1B_1)M_0}{R}\right]\frac{\mathrm{FA}}{D_2} =$$

$$= -k_\xi\frac{\mathrm{FA}}{c_2}. \quad \text{(C.20)}$$

In Eqs. (C.17) to (C.20), $M_{T,2} = |\Omega_2|R_{T,2}/a_0$ represents the blade tip rotational Mach number, and $\Omega_{12} = |\Omega_1|/|\Omega_2|$ is the ratio of the angular speeds of the two rotors. MCA is the local midchord alignment, or sweep, of the blade section of radius R, as defined in Figure 4.5 b).

Complex terms $C_{Lh_1}(R)$ and $C_{Dh_1}(R)$ result from the integration along γ, that is, the integration in chordwise direction, of the harmonic dipole sources $l_{\xi h}(\gamma, R)$ and $l_{\gamma h}(\gamma, R)$, respectively. Therefore, Hanson [39] refers to these terms as the lift and drag harmonics, and they are related to the distributed dipole sources by means of the following equations:

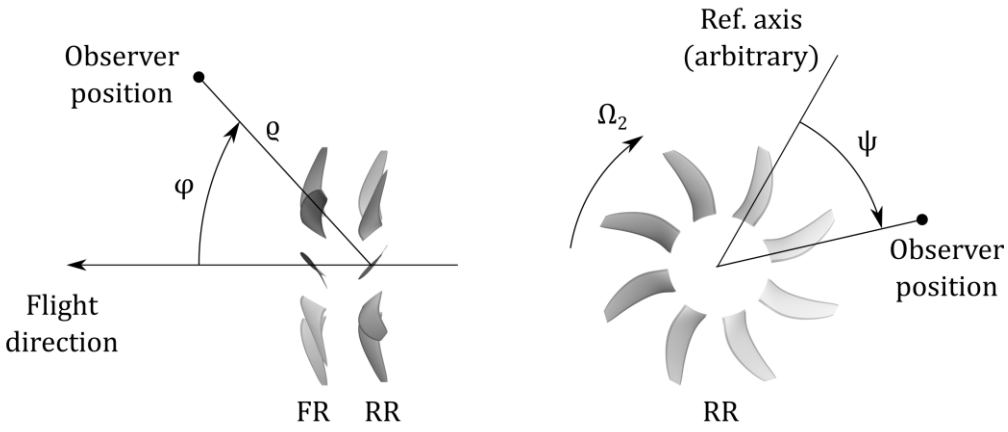

Figure C.1 – Spherical coordinate system, (ϱ, φ, ψ), moving forward with the rotor.

$$l_{\xi h}(\gamma, R) = \frac{\rho_0 V_{adv,2}^2}{2} C_{Lh_1}(R) f_{Lh_1}(\chi)\,, \tag{C.21}$$

$$l_{\gamma h}(\gamma, R) = \frac{\rho_0 V_{adv,2}^2}{2} C_{Dh_1}(R) f_{Dh_1}(\chi)\,, \tag{C.22}$$

where $\chi = (\gamma - \mathrm{MCA})/c_2$ is the normalized chordwise distance that ranges from -0.5 at the LE to 0.5 at the TE, while f_{Lh_1} and f_{Dh_1} are factors with unit area that give the shape of the load distribution. Note that Eqs. (C.21) and (C.22) imply that $f_{Lh_1}(\chi)$ and $f_{Dh_1}(\chi)$ are real functions.

In Eq. (C.16), complex coefficients $\Psi_{Lh_1}(k_\gamma)$ and $\Psi_{Dh_1}(k_\gamma)$ are dimensionless non-compactness factors. They account for the effect of the actual distribution of the sources along the chord of the blade sections [38,39], and they are computed according to the equations:

$$\Psi_{Lh_1}(k_\gamma) = \int_{-1/2}^{1/2} f_{Lh_1}(\chi) e^{ik_\gamma \chi} d\chi\,, \tag{C.23}$$

$$\Psi_{Dh_1}(k_\gamma) = \int_{-1/2}^{1/2} f_{Dh_1}(\chi) e^{ik_\gamma \chi} d\chi\,. \tag{C.24}$$

$\Psi_{Lh_1}(k_\gamma)$ and $\Psi_{Dh_1}(k_\gamma)$ modify the acoustic pressure amplitude by introducing a phase shift and an amplitude variation, which depend on the chordwise distribution of the dipoles $f_{Lh_1}(\chi)$ and $f_{Dh_1}(\chi)$.

The exponential term $exp[i(\phi_l + \phi_s)]$ introduces a phase shift that accounts for the local misalignment of the blade surface with respect to the ideal helicoidal surface, where the noise sources are assumed to lie. In fact, Eqs. (C.19) and (C.20) show that parameters ϕ_l and ϕ_s depends on the local geometrical quantities FA and MCA of a blade section, which correspond to the local lean and sweep of the blade, respectively.

Term $exp[-i(h_2 B_2 |\Omega_2| + h_1 B_1 |\Omega_1|)t]$ within the double summation in Eq. (C.16) shows that the acoustic pressure detected by the observer consists of the superposition of all the harmonic signals with frequencies

$$f = \frac{\left|h_1 B_1 |\Omega_1| + h_2 B_2 |\Omega_2|\right|}{2\pi} = |h_1 BPF_1 + h_2 BPF_2|\,, \tag{C.25}$$

which are linear combination of the blade passing frequencies of the two rotors. Note that for $h_1 = 0$ the sources are steady for an observer rotating with the blade ($\omega_{h_1} = 0$). In this case, $C_{L0}(R)$ and $C_{D0}(R)$ represent the ordinary steady lift and drag coefficients, and Eq. (C.16) gives the loading noise emitted by the rotor at frequencies $f = |h_2 BPF_2|$. Instead, the contribution of the harmonics characterized by both $h_1 \neq 0$ and $h_2 \neq 0$ corresponds to the interaction noise.

The exponential term $exp[i(h_2 B_2 - h_1 B_1)(\psi - \pi/2\,)]$ describes the pattern of the acoustic pressure in azimuthal direction ψ at constant time t. This pressure distribution in space spins around the rotor axis at frequency $f = |h_1 BPF_1 + h_2 BPF_2|$.

It should be noted that, although Eq. (C.16) allows computing the time history of the acoustic pressure disturbance at a desired observer position, it depends on the harmonic content of the blade loading. Therefore, provided that C_{Lh_1}, C_{Dh_1}, Ψ_{Lh_1} and Ψ_{Dh_1} are known from a separate analysis, the discrete tones that contribute to the noise emission can be directly calculated. For the purpose of computing the pressure amplitude for a specific IN frequency, the exponential terms describing the azimuthal pattern and the time advance of the pressure disturbances can be repealed by Eq. (C.16), since they do not influence the signal amplitude. Thus, the Fourier coefficient, $P_{h_1,h_2}(\varrho, \varphi)$, of the harmonic with frequency $f = |h_1 BPF_1 + h_2 BPF_2|$, for $h_1, h_2 \in \{\dots, -2, -1, 1, 2, \dots\}$, is computed by means of Eq. (4.11) presented in Chapter 4. Then, the pressure amplitude is given by $A_p(\varrho, \varphi, f) = 2\left|P_{h_1,h_2}(\varrho, \varphi)\right|$ (Eq. (4.12)). Notice that the pressure amplitude for a specific frequency does not depend on the azimuthal angle ψ, which influences only the phase of the harmonic.

REFERENCES

[1] D.E. Van Zante, Progress in Open Rotor Research: A U.S. Perspective, in: ASME Turbo Expo 2015, Montreal, Canada, 2015. doi:10.1115/GT2015-42203.

[2] T. Kirker, Procurement and testing of a 1/5 scale advanced counter rotating propfan model, in: 13th Aeroacoustics Conf., American Institute of Aeronautics and Astronautics, Reston, Virigina, 1990. doi:10.2514/6.1990-3975.

[3] GE Aviation, Open Rotor Engine Aeroacoustic Technology. Final Report, 2013.

[4] C.A. Negulescu, Airbus AI-PX7 CROR Design Features and Aerodynamics, SAE Int. J. Aerosp. 6 (2013) 626–642. doi:10.4271/2013-01-2245.

[5] H. Nichols, UDF engine/MD80 flight test program, in: 24th Jt. Propuls. Conf., American Institute of Aeronautics and Astronautics, Reston, Virigina, 1988. doi:10.2514/6.1988-2805.

[6] W.C. Strack, G. Knip, A.L. Weisbrich, J. Godston, E. Bradley, Technology and Benefits of Aircraft Counter Rotation Propellers, NASA TM-82983. (1982).

[7] R.D. Hager, D. Vrabel, Advanced turboprop project, NASA Tech. Rep. No. SP-495. (1988).

[8] A. Abbas, J. De Vicente, E. Valero, Aerodynamic technologies to improve aircraft performance, Aerosp. Sci. Technol. 28 (2013) 100–132. doi:10.1016/j.ast.2012.10.008.

[9] D.E. Van Zante, E. Envia, Prediction of the Aero-Acoustic Performance of Open Rotors, in: ASME Turbo Expo 2014, 2014. doi:10.1115/GT2014-26413.

[10] D. Sree, Far-Field Acoustic Power Level and Performance Analyses of F31/A31 Open Rotor Model at Simulated Scaled Takeoff, Nominal Takeoff, and Approach Conditions, NASA CR-218716. (2015).

[11] D. Sree, Near-Field Acoustic Power Level Analysis of F31/A31 Open Rotor Model at Simulated Cruise Conditions, NASA CR-218845. (2015).

[12] D.E. Van Zante, F. Collier, A. Orton, S.A. Khalid, J.P. Wojno, T.H. Wood, Progress in open rotor propulsors: The FAA/GE/NASA open rotor test campaign, Aeronaut. J. 118 (2014) 1181–1213. doi:10.1017/S0001924000009842.

[13] J. Ricouard, E. Julliard, M. Omais, V. Regnier, A. Parry, S. Baralon, Installation Effects on Contra-Rotating Open Rotor Noise, 16th AIAA/CEAS Aeroacoustics Conf. (2010) 1–8. doi:10.2514/6.2010-3795.

[14] C. Paquet, E. Julliard, J. Ricouard, P. Spiegel, Z08: low-speed aero-acoustic

experimental characterization of open rotor installation on aircraft, in: 20th AIAA/CEAS Aeroacoustics Conf., Atlanta, GA, 2014. doi:10.2514/6.2014-2747.

[15] A. Zachariadis, C.A. Hall, Application of a Navier–Stokes Solver to the Study of Open Rotor Aerodynamics, J. Turbomach. 133 (2011). doi:10.1115/1.4001246.

[16] A. Zachariadis, C. Hall, A.B. Parry, Contrarotating Open Rotor Operation for Improved Aerodynamics and Noise at Takeoff, J. Turbomach. 135 (2013). doi:10.1115/1.4006778.

[17] T. Brandvik, C. Hall, A.B. Parry, Angle-of-Attack Effects on Counter-Rotating Propellers at Take-Off, in: ASME Turbo Expo 2012, Copenhagen, Denmark, 2012. doi:10.1115/GT2012-69901.

[18] G. Delattre, F. Falissard, Influence of Torque Ratio on Counter-Rotating Open-Rotor Interaction Noise, AIAA J. 53 (2015) 2726–2738. doi:10.2514/1.J053797.

[19] S. Stapelfeldt, T. Parry, M. Vahdati, Validation of time-domain single-passage methods for the unsteady simulation of a contra-rotating open rotor, Proc. Inst. Mech. Eng. Part A J. Power Energy. 229 (2015) 443–453. doi:10.1177/0957650915596279.

[20] T. Deconinck, A. Capron, C. Hirsch, G. Ghorbaniasl, Prediction of Near-And Far-Field Noise Generated by Contra-Rotating Open Rotors, Int. J. Aeroacoustics. 11 (2012) 177–196. doi:10.1260/1475-472X.11.2.177.

[21] International Civil Aviation Organization, Novel Aircraft-Noise Technology Review and Medium- and Long-Term Noise Reduction Goals, ICAO Rep. (2014).

[22] R.J. Astley, Can technology deliver acceptable levels of aircraft noise ?, Inter-Noise 2014. (2014) 1–12.

[23] B. Magliozzi, D.B. Hanson, R.K. Amiet, Propeller and Propfan Noise, NASA Langley Res. Center, Aeroacoustics Flight Veh. Theory Pract. Vol. 1 Noise Sources. NASA TR-90-3052. (1991) 1–64.

[24] J.E. Ffowcs Williams, D.L. Hawkings, Sound Generation by Turbulence and Surfaces in Arbitrary Motion, Philos. Trans. R. Soc. A Math. Phys. Eng. Sci. 264 (1969) 321–342. doi:10.1098/rsta.1969.0031.

[25] F. Farassat, Linear Acoustic Formulas for Calculation of Rotating Blade Noise, AIAA J. 19 (1981) 1122–1130. doi:10.2514/3.60051.

[26] D.B. Hanson, M.R. Fink, The importance of quadrupole sources in prediction of transonic tip speed propeller noise, J. Sound Vib. 62 (1979) 19–38. doi:10.1016/0022-460X(79)90554-6.

[27] M.J. Kingan, Open rotor broadband interaction noise, J. Sound Vib. 332 (2013) 3956–3970. doi:10.1016/j.jsv.2013.03.014.

[28] T. Node-Langlois, F. Wlassow, V. Languille, Y. Colin, B. Caruelle, J.R. Gill, X. Chen,

X. Zhang, A.B. Parry, Prediction of Contra-Rotating Open Rotor broadband noise in isolated and installed configurations, in: 20th AIAA/CEAS Aeroacoustics Conf., Atlanta, GA, 2014. doi:10.2514/6.2014-2610.

[29] A. Peters, Z.S. Spakovszky, Rotor Interaction Noise in Counter-Rotating Propfan Propulsion Systems, Vol. 7 Turbomachinery, Parts A, B, C. 134 (2010) 2821–2834. doi:10.1115/GT2010-22554.

[30] R.P. Woodward, E.B. Gordon, Noise of a model counterrotation propeller with reduced aft rotor diameter at simulated takeoff/approach conditions (F7/A3), NASA TM-100254, 26th Aerosp. Sci. Meet. (1988).

[31] C. Rohrbach, F.B. Metzger, D.M. Black, R.M. Ladden, Evaluation of wind tunnel performance testings of an advanced 45° swept eight-bladed propeller at Mach numbers from 0.45 to 0.85, NASA CR-3505. (1982).

[32] R. Schnell, J. Yin, C. Voss, E. Nicke, Assessment and Optimization of the Aerodynamic and Acoustic Characteristics of a Counter Rotating Open Rotor, J. Turbomach. 134 (2012). doi:10.1115/1.4006285.

[33] M.J. Lighthill, On Sound Generated Aerodynamically. I. General Theory, Proc. R. Soc. A Math. Phys. Eng. Sci. 211 (1952) 564–587. doi:10.1098/rspa.1952.0060.

[34] M.J. Lighthill, On Sound Generated Aerodynamically. II. Turbulence as a Source of Sound, Proc. R. Soc. A Math. Phys. Eng. Sci. 222 (1954) 1–32. doi:10.1098/rspa.1954.0049.

[35] J.D. Denton, The Calculation of Three-Dimensional Viscous Flow Through Multistage Turbomachines, J. Turbomach. 114 (1992) 18–26. doi:10.1115/1.2927983.

[36] Y. Colin, A. Carazo, B. Caruelle, T. Node-Langlois, A. Parry, Computational strategy for predicting CROR noise at low-speed Part I: review of the numerical methods, in: 18th AIAA/CEAS Aeroacoustics Conf. (33rd AIAA Aeroacoustics Conf., Colorado Springs, CO, 2012. doi:10.2514/6.2012-2221.

[37] M.E. Goldstein, Aeroacoustics, McGraw-Hill. (1976).

[38] D.B. Hanson, Helicoidal Surface Theory for Harmonic Noise of Propellers in the Far Field, AIAA J. 18 (1980) 1213–1220. doi:10.2514/3.50873.

[39] D.B. Hanson, Noise of counter-rotation propellers, J. Aircr. 22 (1985) 609–617. doi:10.2514/3.45173.

[40] C.M. Ekoule, A. McAlpine, A.B. Parry, M. Kingan, N. Sohoni, Development of a Hybrid Method for the Prediction of Advanced Open Rotor Tone Noise, in: 23rd AIAA/CEAS Aeroacoustics Conf., Denver, CO, 2017. doi:10.2514/6.2017-3870.

[41] A. Carazo, M. Roger, M. Omais, Analytical Prediction of Wake-Interaction Noise in

Counter-Rotation Open Rotors, in: 17th AIAA/CEAS Aeroacoustics Conf. Portl., Portland, Oregon, 2011. doi:10.2514/6.2011-2758.

[42] R. Jaron, A. Moreau, S. Guerin, RANS-informed fan noise prediction: separation and extrapolation of rotor wake and potential field, in: 20th AIAA/CEAS Aeroacoustics Conf., Atlanta, GA, 2014. doi:10.2514/6.2014-2946.

[43] R. Jaron, A. Moreau, S. Guerin, Extrapolation of RANS flow data for improved analytical fan tone prediction, in: 21st AIAA/CEAS Aeroacoustics Conf., Dallas, TX, 2015. doi:10.2514/6.2015-2515.

[44] G. Grasso, S. Moreau, J. Christophe, C. Schram, Multi-disciplinary optimization of a contra-rotating fan, Int. J. Aeroacoustics. (2018) 1–32. doi:10.1177/1475472X18789000.

[45] M. Kingan, R. Self, Counter-Rotation Propeller Tip Vortex Interaction Noise, in: 15th AIAA/CEAS Aeroacoustics Conf. (30th AIAA Aeroacoustics Conf., Miami, Florida, 2009. doi:10.2514/6.2009-3135.

[46] M.E. Quaglia, T. Léonard, S. Moreau, M. Roger, A 3D analytical model for orthogonal blade-vortex interaction noise, J. Sound Vib. 399 (2017) 104–123. doi:10.1016/j.jsv.2017.03.023.

[47] J. Leishman, Principles of helicopter aerodynamics, (2006).

[48] GE Aircraft Engines, Full Scale Technology Demonstration of a Modern Counterrotating Unducted Fan Engine Concept. Design Report, NASA CR-180867. (1987).

[49] GE Aircraft Engines, Experimental Performance and Acoustic Investigation of Modern, Counterrotating Blade Concepts. Final Report, NASA CR-185158. (1990).

[50] R.P. Woodward, C.E. Hughes, Aeroacoustic effects of reduced aft tip speed at constant thrust for a model counterrotation turboprop at takeoff conditions, NASA TM-103608. (1990).

[51] ANSYS-FLUENT 17, ANSYS Inc. (2016).

[52] R. Raj, B. Lakshminarayana, Characteristics of the wake behind a cascade of airfoils, J. Fluid Mech. 61 (1973) 707–730. doi:10.1017/S002211207300090X.

[53] J.L. Kerrebrock, Small disturbances in turbomachine annuli with swirl, AIAA J. 15 (1977) 794–803. doi:10.2514/3.7370.

[54] J.J. Adamczyk, Passage of a Swept Airfoil through an Oblique Gust, J. Aircr. 11 (1974) 281–287. doi:10.2514/3.59240.

[55] D. Tormen, P. Giannattasio, A. Zanon, H. Kühnelt, M. De Gennaro, Application of a RANS-Informed Analytical Model for Fast Noise Prediction of Contra Rotating Open Rotors, in: ASME Turbo Expo 2017, Charlotte, NC, 2017. doi:10.1115/GT2017-64162.

[56] G.K. Batchelor, Axial flow in trailing line vortices, J. Fluid Mech. 20 (1964) 645–658. doi:10.1017/S0022112064001446.

[57] Q.R. Wald, The aerodynamics of propellers, Prog. Aerosp. Sci. 42 (2006) 85–128. doi:10.1016/j.paerosci.2006.04.001.

[58] A.J. Landgrebe, An analytical and experimental investigation of helicopter rotor hover performance and wake geometry characteristics, 1971.

[59] D. Van Zante, M. Wernet, Tip Vortex and Wake Characteristics of a Counterrotating Open Rotor, in: 48th AIAA/ASME/SAE/ASEE Jt. Propuls. Conf. Exhib., American Institute of Aeronautics and Astronautics, Atlanta, GA, 2012. doi:10.2514/6.2012-4039.

[60] J. Leishman, Challenges in modeling the unsteady aerodynamics of wind turbines, in: 2002 ASME Wind Energy Symp., Reno, NV, 2002. doi:10.2514/6.2002-37.

[61] H. Abedi, L. Davidson, S. Voutsinas, Enhancement of Free Vortex Filament Method for Aerodynamic Loads on Rotor Blades, in: ASME 2014 Int. Mech. Eng. Congr. Expo., 2014. doi:10.1115/IMECE2014-36082.

[62] Y. Levy, A. Seginer, D. Degani, Graphical visualization of vortical flows by means of helicity, AIAA J. 28 (1990) 1347–1352. doi:10.2514/3.25224.

[63] D.C. Mikkelson, B.J. Blaha, G.A. Mitchell, J.E. Wikete, Design and Performance of Energy Efficient Propellers for Mach 0.8 Cruise, NASA TM X-73612. (1977).

[64] A. Moreau, S. Guérin, Development and Application of a New Procedure for Fan Noise Prediction, in: 16th AIAA/CEAS Aeroacoustics Conf., American Institute of Aeronautics and Astronautics, Reston, Virigina, 2010. doi:10.2514/6.2010-4034.

[65] A. Holewa, C. Weckmüller, S. Guérin, Impact of Bypass Duct Bifurcations on Fan Noise, J. Propuls. Power. 30 (2014) 143–152. doi:10.2514/1.B34957.

[66] T. Von Karman, W.R. Sears, Airfoil Theory for Non-Uniform Motion, J. Aeronaut. Sci. 5 (1938) 379–390. doi:10.2514/8.674.

[67] W.R. Sears, Some Aspects of Non-Stationary Airfoil Theory and Its Practical Application, J. Aeronaut. Sci. 8 (1941) 104–108. doi:10.2514/8.10655.

[68] D.B. Hanson, Compressible Helicoidal Surface Theory for Propeller Aerodynamics and Noise, AIAA J. 21 (1983) 881–889. doi:10.2514/3.60132.